CellPress

Matter

Review

Single-crystal halide perovskites: Opportunities and challenges

Yusheng Lei,[1,2] Yimu Chen,[2] and Sheng Xu[2,3,4,5,*]

SUMMARY

Single-crystal halide perovskites have demonstrated excellent optoelectronic properties and promising device application potentials, thanks to their remarkable carrier dynamics, solution processing procedures, and outstanding stabilities. The latest progress and future perspectives of single-crystal halide perovskites are reviewed herein. The basic properties and fundamental studies of single-crystal halide perovskites are first discussed. We then introduce the growth methods for these materials and summarize their recent developments. We further present the single-crystal halide perovskite devices among their major application fields. Finally, we discuss current challenges and provide some suggestions for their further development. We hope this paper can help readers understand the status and future challenges for single-crystal halide perovskites.

INTRODUCTION

As a class of emerging semiconductors, halide perovskites hold significant potentials for multiple fields. However, current halide perovskite electronic devices are heavily focused on polycrystalline thin films, primarily due to the simplicity of depositing polycrystals.[1,2] Despite their successful use cases in various devices, polycrystalline halide perovskite thin films face many challenges that greatly impede their further research, development, and commercialization of those devices. A high density of structural defects is typically present in the polycrystalline thin films, including point defects (e.g., vacancies, interstitials, and substitutional antisites), impurities, dislocations, grain boundaries, and residual precipitates (e.g., PbI_2 cluster and metallic Pb from the fast antisolvent deposition process).[3] Those defects result in non-radiative carrier loss,[4] material degradation,[5] device hysteresis,[6] and many other detrimental effects.[7,8] Single-crystal halide perovskites, on the contrary, exhibit a largely suppressed density of those structural defects due to the ordered lattice arrangement. This structural superiority bestows the single-crystal halide perovskites with several attractive benefits, which has garnered growing attention in the field.[8–12] In this review, we summarize the advances that have been made to date in developing single-crystal halide perovskites, with a focus on their property merits, growth methods, and use cases. Finally, we share our thoughts on several outstanding challenges, inviting more researchers to contribute to this exciting field.

BASIC PROPERTIES OF HALIDE PEROVSKITES

Compared with conventional semiconductors, halide perovskites show structural as well as compositional versatility, which confers fascinating semiconductive properties for a wide range of applications.

The structure and composition of halide perovskites

Perovskite was first discovered by German mineralogist Gustav Rose in Russian's Ural Mountains in 1839.[13] Perovskites share the same ABX_3 crystal structure. In

Progress and potential

Single-crystal halide perovskites have received growing attention due to their high carrier-transport efficiency and excellent stability in comparison with their polycrystalline counterparts. This review is timely, since it gives a comprehensive overview of the advances in single-crystal halide perovskite, including their unique physical properties, controllable crystal growth, and, most importantly, device applications. In the end, we share our perspectives on the remaining challenges and potential solutions for driving this emerging field forward. This review will provide food for thought to researchers in the field and a jump-start to beginners who want to join this exciting field.

© 2021 Elsevier Inc.

halide perovskites, A is a general cation that can be organic or inorganic, B is a metallic cation, and X is a halide anion.[14] Specifically, common A-site cations include Cs^+,[15] Rb^+,[16] K^+,[17] methylammonium (MA^+),[18] formamidinium (FA^+),[19] dimethylammonium (DMA^+),[20] ethylammonium (EA^+),[21] guanidinium (GUA^+),[22] tetramethylammonium (TMA^+),[23] tetrabutylammonium (TBA^+),[24] and phenylethylammonium (PEA^+);[25,26] Common B-site metallic cations include Pb^{2+},[27] Mg^{2+},[28] Ca^{2+},[29] Ba^{2+},[29] Mn^{2+},[30] Fe^{2+},[31] Ni^{2+},[32] Cu^{2+},[33] Zn^{2+},[34] Cd^{2+},[35] Ge^{2+},[36] Sn^{2+},[37] Eu^{2+},[38] Tm^{2+},[39] and Yb^{2+};[40] Common X-site anions are Cl^-,[41] Br^-,[42] I^-,[43] formate ($HCOO^-$),[44] and BH_4^-.[45] Depending on the effective radii of the A-site cations, B-site cations, and X-site anions, the crystal lattice of halide perovskites ranges from a highly symmetric cubic structure to a less-symmetric tetragonal or orthorhombic structure (Figure 1A).[46] In general, the backbone of these pseudocubic structures consists of the corner-sharing $[BX_6]$ octahedra, with A-site cations occupying the 12-fold coordination sites formed in the middle of eight $[BX_6]$ octahedra.[47]

A tolerance factor is usually used to evaluate whether a pseudocubic perovskite structure can be maintained:[51]

$$t = \frac{r_A + r_X}{\sqrt{2(r_B + r_X)}},$$

where t is the tolerance factor, r_A is the effective radius of the A-site general cation, r_B is the effective radius of the B-site metallic cation, and r_X is the effective radius of the X-site halide anion. Empirically, a halide perovskite structure with a calculated t ranging from 0.8 to 1 is considered to be stable with cubic symmetry (Figure 1B).[15,46,48] If the size of A is relatively small (e.g., for MA^+ cations with a radius of 217 pm[15]), then t would be small, and a tetragonal or orthorhombic structure will be formed. On the other side, if the size of A is too large (e.g., for TBA^+ cations with a radius of 494 pm[24]), the perovskite will adopt a layered two-dimensional (2D) or a linear one-dimensional (1D) structure such as the Ruddlesden-Popper phase, the Dion-Jacobson phase, and the alternating-cation phase (Figure 1C).[52] The size of B cations (e.g., Pb^{2+} with a radius of 119 pm[15] and Sn^{2+} with a radius of 110 pm[15]) usually will not have a big impact on t since they do not change much compared with the size of A. The size of X anions can effectively affect the crystal structure of halide perovskites. For example, $MAPbI_3$ (I^- with a radius of 220 pm[15]) adopts a tetragonal structure under room temperature while $MAPbBr_3$ and $MAPbCl_3$ (Br^- with a radius of 196 pm[15] and Cl^- with a radius of 181 pm[15]) adopt a cubic structure. Also, F^--based halide perovskites are rarely studied due to the small size of the F^- anion (129 pm in radius[15]), which results in a too-small tolerance factor to hold the crystal lattice.[53] Because of the high tunability in structures and compositions, the halide perovskites show very versatile functionalities.[54]

General merits of halide perovskites

Halide perovskites are intriguing semiconductors. It has been reported that the valence band maximum of halide perovskites mainly consists of s orbitals of heavy metal ions (e.g., Pb^{2+}) and p orbitals of halide ions (e.g., I^-).[55] Therefore, substituting the chemical composition can effectively alter the coupling of the orbitals and, consequently, the electronic band structures of the perovskites, which enables a broad range of applications.[56–59] With different compositions, halide perovskites show a tunable direct band gap between 1.2 eV and 3.1 eV (Figures 1D and 1E),[60] which covers the entire visible spectrum.

Besides, halide perovskites demonstrate tunable exciton (bound electron-hole pairs) binding energies (E_b) based on their compositions and dimensions. For the

[1]Department of Chemical Engineering, Stanford University, Stanford, CA 94305, USA
[2]Department of Nanoengineering, University of California San Diego, La Jolla, CA 92093, USA
[3]Materials Science and Engineering Program, University of California San Diego, La Jolla, CA 92093, USA
[4]Department of Bioengineering, University of California San Diego, La Jolla, CA 92093, USA
[5]Department of Electrical and Computer Engineering, University of California San Diego, La Jolla, CA 92093, USA
*Correspondence: shengxu@ucsd.edu

https://doi.org/10.1016/j.matt.2021.05.002

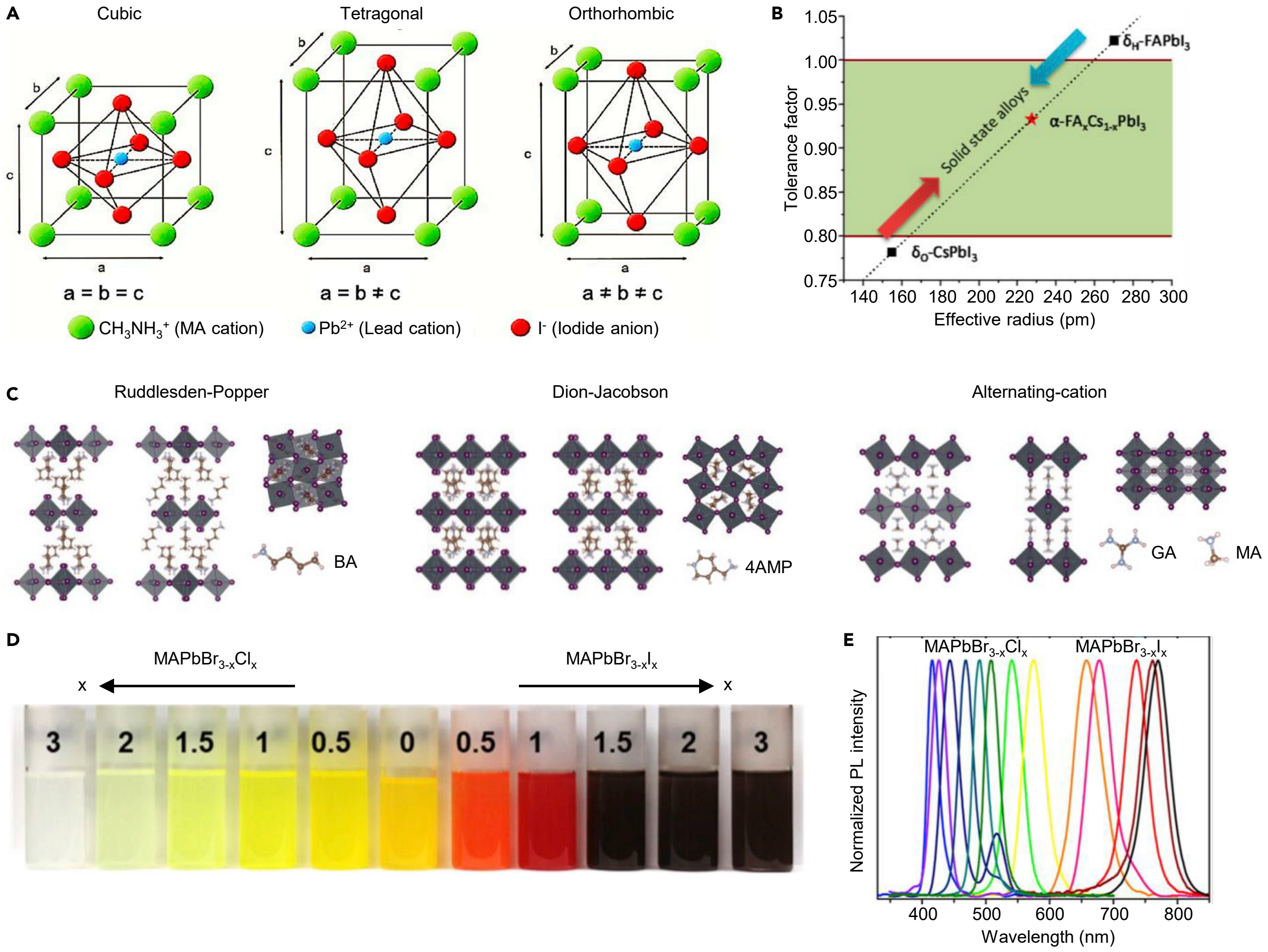

Figure 1. The tunable structure, composition, and band gap of halide perovskites

(A) Schematic lattices of 3D halide perovskites with different crystal structures.[46] Different pseudocubic structures can be formed with different compositions and external conditions. Copyright 2020, American Chemical Society.

(B) Relationship between the composition and the tolerance factor.[48] In this plot, the tolerance factors of $FAPbI_3$ (>1.0) and $CsPbI_3$ (<0.8) fall outside of the range of stability due to the cation size. Alloying FA^+ and Cs^+ cations can neutralize the tolerance factor into the range of stability. Copyright 2015, American Chemical Society.

(C) Schematic lattices of 2D halide perovskites with different crystal structures.[49] The most representative crystal structures are Ruddlesden-Popper, Dion-Jacobson, and alternating-cation. Copyright 2020, Springer Nature.

(D) Optical images of $MAPbX_3$ colloidal solutions with different halide compositions,[50] demonstrating the tunable band gap by compositional engineering. Copyright 2015, American Chemical Society.

(E) Photoluminescent spectra of the corresponding band-gap-tunable $MAPbX_3$ colloidal solutions.[50] Copyright 2015, American Chemical Society.

widely studied $MAPbI_3$, E_b is reported to be ~10 meV,[61] which is much smaller than the thermal energy at room temperature (~26 meV), indicating that the excitons can easily overcome the Coulombic interaction by thermal fluctuation and become free charge carriers.[62] The free charge carriers can be readily separated and collected upon excitation, which is suitable for photovoltaic and photodetection applications. On the other side, reducing the dimensions of halide perovskites[63] and changing the composition by substituting the halide ions with others[64] can effectively increase the E_b to several hundreds of millielectron volts. A large E_b enables enhanced radiative recombination of the charge carriers, which is advantageous for light-emitting applications.

Additionally, halide perovskites have shown superior carrier-transport properties. High mobility (up to several hundreds of $cm^2 \cdot V^{-1} \cdot s^{-1}$, due to the relatively low electron/hole effective masses[65]) and long lifetime (up to several microseconds, due to the relatively benign defect chemistry[65,66]) of charge carriers have been reported in halide perovskites,[65] contributing to the long charge carrier diffusion length (up to tens of micrometers).[47] It is worth mentioning that the carrier mobility of halide perovskites is found to be comparable with those of typical inorganic semiconductors (e.g., GaAs).[67] Fröhlich interaction, which is the intrinsic coupling between carriers and phonons in polar semiconductors,[68] relaxes the carriers' initial kinetic energy to the lattice and therefore limits the further increase of carrier mobility in halide perovskites.[63] Nevertheless, these outstanding carrier-transport properties render halide perovskites extremely suitable for applications like highly efficient photovoltaic, low-limit photodetection, and many others.

Meanwhile, halide perovskites typically show a high absorption coefficient up to 10^5 cm^{-1} over the entire visible spectrum,[69] due to the strong interband transition.[70,71] This absorption coefficient is more than one order of magnitude higher than that of Si.[72] The high absorption coefficient enables a required absorber thickness of <400 nm in photovoltaic devices, which is much thinner than those made of Si.[73] Consequently, a reduced device thickness can not only reduce devices' cost significantly, but also potentially suppress the charge carrier recombination and, according to the Shockley-Queisser model,[74] lead to a high open-circuit voltage (V_{OC}) in photovoltaics.

Last but not least, halide perovskites can be processed by low-temperature solution methods.[75] Unlike conventional semiconductors that typically required vacuum-based deposition under high temperatures, the solution processability of halide perovskites can be readily scaled up at a low cost. There is no need for any fancy equipment, which allows quick and wide adoption of perovskite research worldwide. Different from other solution-processable semiconductors (e.g., quantum dots[76] and organic materials[77]), high-quality halide perovskite single crystals can be easily grown by several crystallization methods.

CURRENT STUDIES OF SINGLE-CRYSTAL HALIDE PEROVSKITES

Most of the devices reported to date are based on polycrystalline halide perovskite thin films with compromised electronic and optoelectronic performance. Single-crystal halide perovskites possess merits that warrant effective solutions to mitigate these problems, such as carrier recombination, current-voltage hysteresis, and instability.[9–12]

Carrier recombination

The recombination of free carriers directly determines the mean free time of the carriers in semiconductors. Structural defects lead to the formation of electronic traps within the band gap, which can serve as centers for trapping free carriers.[78] Trapped carriers are likely to be detrapped from shallow trap states with sufficiently low activation energies or annihilated in deep trap states with large activation energies.[3] The latter process is mainly attributed to the non-radiative recombination and is detrimental to device performance.

Trap densities can be characterized by *I-V* characteristic curves (Figures 2A and 2B)[4,79] and *C-f* measurements (Figures 2C and 2D).[79–81] The results show that the trap density is between 10^{15} and 10^{17} cm^{-3} for polycrystalline halide perovskite

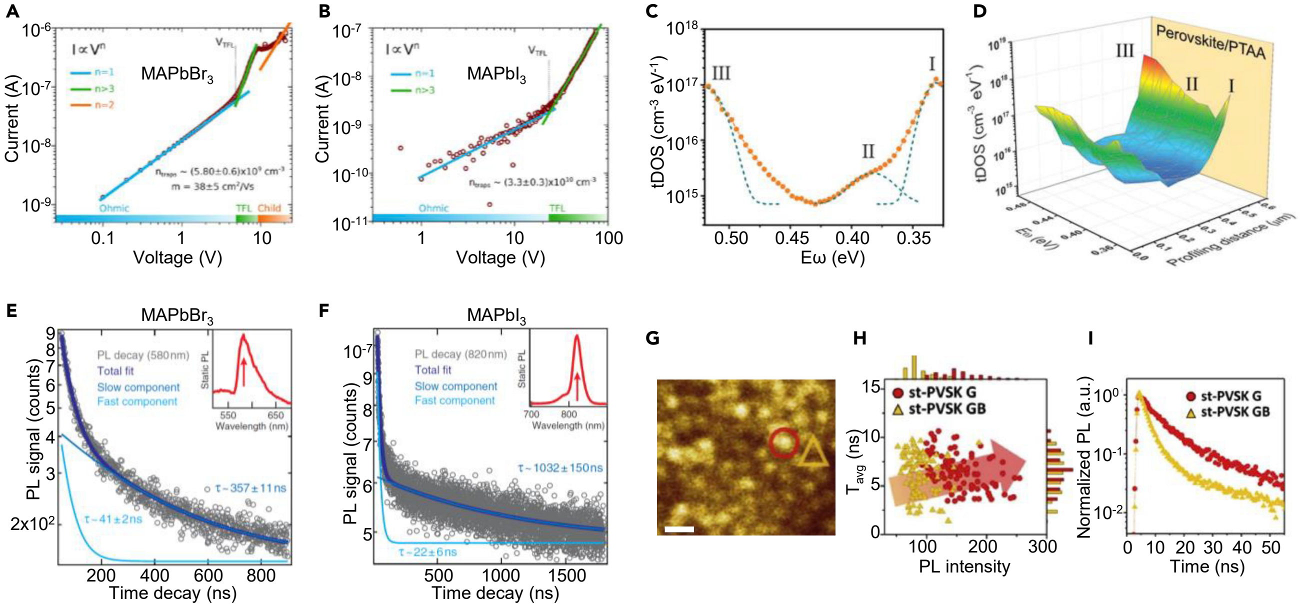

Figure 2. Carrier recombination in halide perovskites

(A and B) Identifying the carrier trap densities in (A) MAPbBr$_3$ and (B) MAPbI$_3$ single crystals by the space-charge-limit-current method.[4] Results show that the trap densities in these single crystals are on the order of 10^9–10^{10} cm^{-3}. Copyright 2015, The American Association for the Advancement of Science.

(C) Trap density energy landscape in a polycrystalline halide perovskite thin film characterized by capacitance-frequency measurements.[8] Results show that the trap density in the polycrystalline thin film is on the order of 10^{17} cm^{-3}. Note that symbols I, II, and III represent three kinds of trap centers with different energies in the electronic band. Copyright 2020, The American Association for the Advancement of Science.

(D–F) (D) Spatial and energy mapping of the trap density in a polycrystalline halide perovskite solar cell characterized by the drive-level capacitance profiling method.[8] Results show that the interfacial traps play a major role. Copyright 2020, The American Association for the Advancement of Science. Identifying the carrier lifetime in (E) MAPbBr$_3$ and (F) MAPbI$_3$ single crystals by time-resolved photoluminescent measurements.[4] Results show that the carrier lifetime can reach on the order of microseconds. Insets: the photoluminescence peaks used in the time-resolved photoluminescent measurements. Copyright 2015, The American Association for the Advancement of Science.

(G) A confocal photoluminescence image of a polycrystalline MAPbI$_3$ thin film.[87] The red circle denotes the mapping at the grain center, while the yellow triangle denotes the mapping at the grain boundary. Scale bar, 500 nm. Copyright 2017, American Chemical Society.

(H) A 2D scatterplot of photoluminescence intensity and average carrier lifetime at the grain center and the grain boundary.[87] Results show that the photoluminescent peak intensity in the grain centers with reduced non-radiative recombination is much stronger than that in the grain boundaries. Copyright 2017, American Chemical Society.

(I) Representative time-resolved photoluminescent decay curves at the grain center and the grain boundary.[87] Results show that the carrier lifetime in the grain center is longer than that in the grain boundary. Copyright 2017, American Chemical Society.

thin films[72] and is around five to seven orders of magnitude lower for single crystals.[4,82] For electronic and optoelectronic devices whose performance is highly related to the carrier diffusion length, such a greatly reduced trap density in single crystals can lead to a suppressed non-radiative recombination of charge carriers and thus augmented device performance. For example, trap-assisted non-radiative carrier recombination based on polycrystalline halide perovskites is the main reason for the reduced fill factor (FF) and voltage loss in solar cells.[83] Lower densities of structural defects and electronic traps in single crystals minimize the non-radiative recombination of charge carriers, as proven by the much-elongated carrier lifetime (Figures 2E and 2F)[84,85] and higher photoluminescence quantum yield.[86]

Note that although increasing the grain size and passivating the grain boundaries in polycrystalline halide perovskite thin films are commonly shown to reduce the non-radiative recombination,[88–90] the role of grain boundaries on the recombination of free carriers is still under debate.[91] Conventionally, grain boundaries are viewed as non-radiative recombination centers due to the generated local heterogeneity (Figure 2G–2I).[92] Recent studies showed that the grain boundaries in polycrystalline copper indium gallium sulfide and copper zinc tin sulfide thin films were benign because the defects in grain boundaries could induce electrostatic barriers and reduce the carrier recombination.[93,94] Similarly, several studies reported benign properties of the grain boundaries in halide perovskites.[91,95] Due to their intrinsic complexity, more studies are needed to reveal the role of grain boundaries in the carrier recombination in halide perovskites.

Carrier transport

Besides trapping the free carriers by forming deep electronic states in the band gap, the point defects can also affect the carrier transport through the Coulomb-interaction-induced defect scattering. The point defects can alter the acceleration vector of the carriers.[96] Due to the reduced point defect densities and the weakened carrier-phonon coupling, single-crystal halide perovskites usually exhibit much-enhanced carrier mobility.[80,97,98] Meanwhile, the absence of grain boundaries eradicates the possible scattering of the charge carriers, contributing to the excellent carrier dynamics in single-crystal halide perovskites.[97,99,100]

Carrier mobility can be experimentally characterized by multiple methods, including the Hecht-equation electrical measurement (Figure 3A),[101] the space-charge-limit-current measurement,[4,102] the time-of-flight measurement (Figures 3B and 3C),[103,104] and the Hall effect measurement.[82] Although electrical characterization methods offer measurement simplicity (e.g., *I-V* curves), they can sometimes involve a high interfacial contact resistance, leading to measurement errors.[65] To solve this problem, contactless optical characterization techniques have been reported, including the terahertz frequency conductivity measurement (Figure 3D),[105] the transient microwave conductivity measurement (Figure 3E),[106] and a customized three-dimensional (3D) optical diffusion-quenching method (Figure 3F).[107] Such measurements could significantly reduce the contact resistance-induced errors and reveal accurate carrier mobility. Despite the type of characterization methods used, single-crystal halide perovskites, in general, show much higher carrier mobility than the polycrystalline counterparts,[60,65,108] holding potentials in ultrafast electroluminescence,[109] lasers,[110] and photodetection.[111]

Ion migration

Due to the relatively low activation energy, ion migration is inevitable in halide perovskites. In particular, under biased operational conditions, ion migration takes place mainly through point defects (e.g., vacancies and interstitials).[112] The activation energies of mobile vacancies and interstitials for organic cations, metal cations, and halide anions have been studied through first-principle calculations.[3] Calculation results show that point defects in halide perovskites have relatively low activation energies, which can lead to a severe ion migration under electric field during device operation.[78,113] Besides, grain boundaries can serve as a channel for the mobile ionic defects, leading to more severe ion migration under biased operational conditions.[46] Also, the accumulation of ions at perovskite/electrode interfaces results in the electric-field screening effect, which can lead to current-voltage hysteresis during electrical measurements.[114] The hysteresis issue poses great difficulties to the accurate measurement of the device performance.[115] Moreover, the migration and accumulation of mobile ions will rupture the halide perovskite lattices as well as the adjacent hole/electron transporting layers.[116] The ion migration will lead to material compositional segregation and decomposition, which can damage the long-term stability of halide perovskite devices.[117] Therefore, it is crucial to suppress the ion migration in halide perovskites.

In single-crystal halide perovskites, there are largely reduced densities of point defects and impurities and an absence of grain boundaries.[60,118] The ion-migration

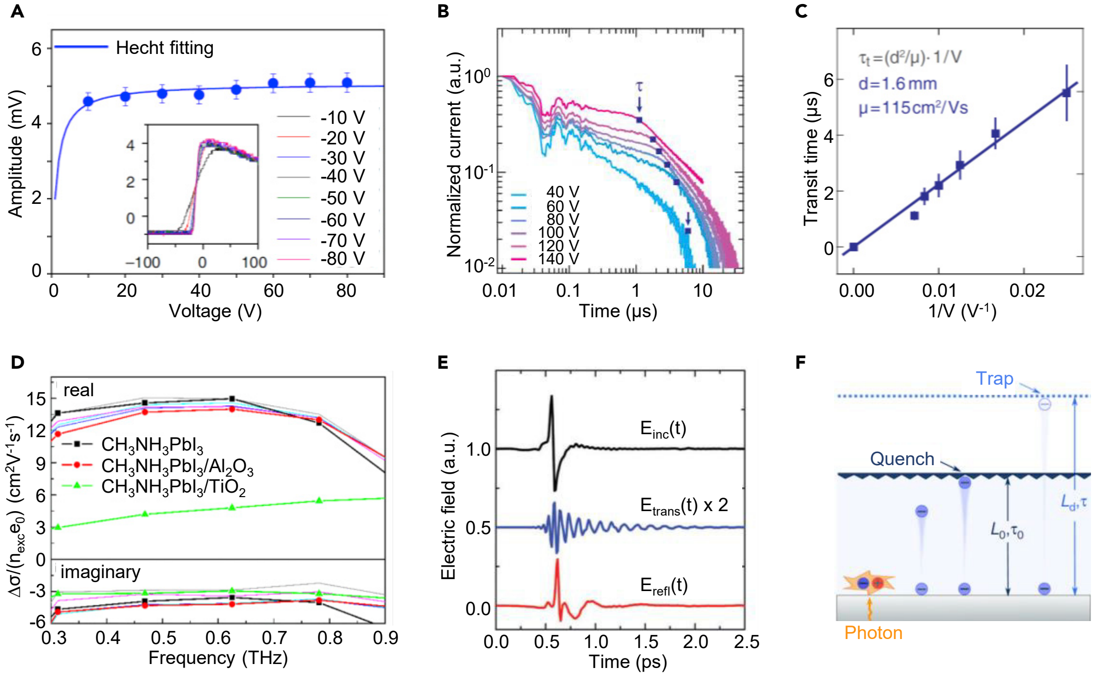

Figure 3. Carrier transport in halide perovskites

(A) Carrier mobility-lifetime product characterized by Hecht measurements.[101] The hole mobility and the hole lifetime are calculated to be 52 $cm^2 V^{-1} s^{-1}$ and 296 μs, respectively. Inset: the relationship between the pulse amplitude and the applied voltage. Copyright 2020, Springer Nature.

(B) Transient photocurrent decay by time-of-flight measurements.[4] The carrier transient time is extracted from the kink where the majority of carriers are extracted, as marked by the black squares. Copyright 2015, The American Association for the Advancement of Science.

(C) Fitting of the calculated carrier transient time to determine the carrier mobility of single-crystal halide perovskites.[4] The carrier mobility of this device is calculated to be 115 $cm^2 V^{-1} s^{-1}$. Copyright 2015, The American Association for the Advancement of Science.

(D) Terahertz photoconductivity spectra of different polycrystalline halide perovskite devices.[106] Copyright 2017, American Chemical Society.

(E) The spectra of the incident (black), transmitted (blue), and reflected (red) microwave pulses after interaction with the single-crystal halide perovskite using transient microwave conductivity measurements.[105] Copyright 2015, The Royal Society of Chemistry.

(F) The schematic concept of the diffusion-quenching model.[107] Carriers are generated at the perovskite/substrate interface, diffuse, and then are quenched before recombination. Copyright 2018, Springer Nature.

activation energy in single-crystal halide perovskites (1.05 eV) is also significantly higher than that in polycrystalline halide perovskites (0.27–0.50 eV) under dark conditions (Figures 4A–4D).[119] Although it is unlikely to fully eliminate ion migration, the density of mobile ions can be significantly suppressed due to the enhanced material crystallinity. A use case to manifest the suppressed ion migration is field-effect transistors (FETs). Halide perovskites are considered as an optimal material for FETs due to their outstanding carrier-transport properties.[120] However, very few groups have achieved room-temperature halide perovskite FETs because the severe gate electric-field screening effect induced by ion migration can degrade the transconductance and compromise the FET performance.[120,121] Single-crystal halide perovskites with significantly suppressed ion migration are seen as a perfect candidate to achieve room-temperature halide perovskite FETs.[122,123] The suppressed ion migration can considerably reduce the operational hysteresis. The realization of reliable single-crystal FET at room temperature would be a milestone in the developmental roadmap of halide perovskite electronics.

Instability

Another merit of single-crystal halide perovskites is their much-enhanced stability. Currently, moisture and oxygen in the air are believed to be the major cause of degrading the halide perovskites.[46] By interacting with the hygroscopic organic

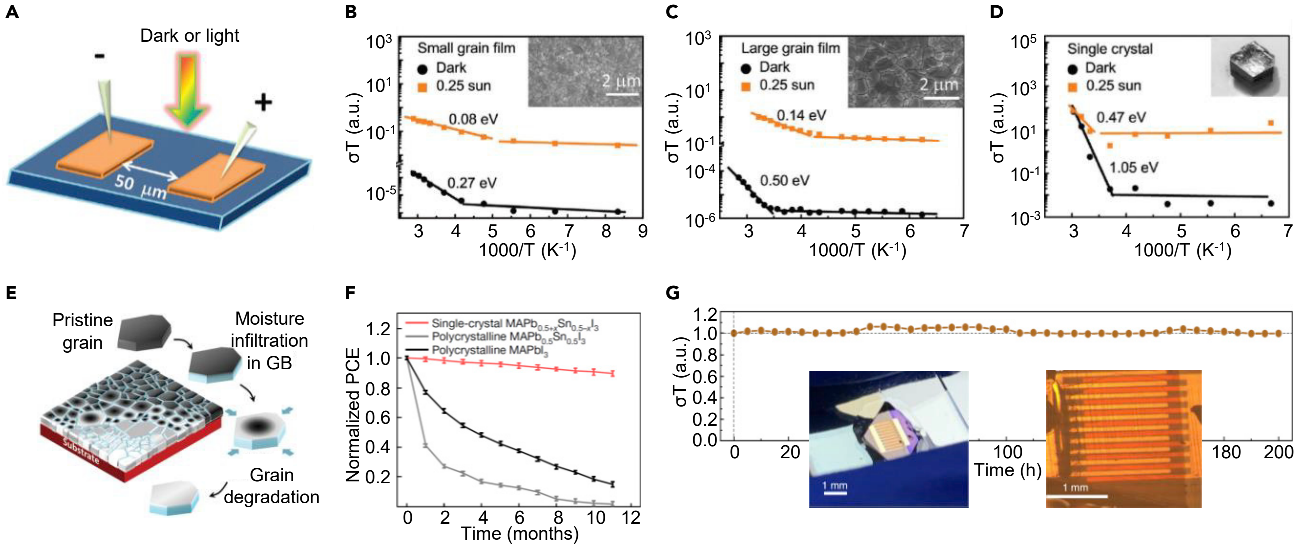

Figure 4. Ion migration and instability in halide perovskites

(A–D) (A) Schematics for measuring ion migration in halide perovskites.[119] Conductivity of the device is measured under different temperatures. Copyright 2016, The Royal Society of Chemistry. The temperature-dependent conductivity of (B) a polycrystalline thin film with small grains, (C) a polycrystalline thin film with large grains, and (D) a single-crystal.[119] Results show that the activation energy for ion migration decreases with increasing the density of grain boundaries. Insets in (B) and (C) are scanning electron microscopy images of the polycrystalline thin films. The inset in (D) is an optical image of a single crystal. Copyright 2016, The Royal Society of Chemistry.

(E) Schematic degradation mechanism of polycrystalline halide perovskite thin films.[124] Moisture penetrates through the grain boundary and decomposes the entire grain. Copyright 2017, The Royal Society of Chemistry.

(F) Operational stability of a vertical-type solar cell based on single-crystal and polycrystalline halide perovskite thin films.[11] Results show that the single-crystal device has a much-enhanced operational stability compared with the polycrystalline. Copyright 2020, Springer Nature.

(G) Enhanced device operational stability in a planar-type solar cell based on single-crystal halide perovskite wafers.[125] Power conversion efficiency degradation can hardly be observed in the 200-h stability test. Insets: optical images of the entire solar cell (left) and a magnified view of the device structure (right). Copyright 2020, Springer Nature.

cations, water molecules can dissociate the interaction between the organic cation and the inorganic lead halide framework and decompose the perovskites. Oxygen molecules can also react with the organic cations in a similar way. Grain boundaries can serve as the channel (i.e., a fast transport highway) for moisture and oxygen penetration and gradually decompose the entire material (Figure 4E).[124] Without proper encapsulation, polycrystalline halide perovskites can decompose in several days under ambient conditions. By eliminating the grain boundaries,[126] and therefore the channel for moisture and oxygen penetration, single-crystal halide perovskites exhibit long-term stability under ambient conditions.[124]

Halide perovskites will also self-decompose. When heated, grain boundaries serve as the channel for the volatilization of organic cations, resulting in the decomposition of halide perovskites. According to thermogravimetric analysis, the single-crystal halide perovskite exhibits enhanced thermal stability compared with the polycrystalline counterpart due to the absence of grain boundaries in the single crystal.[41,127] Single-crystal halide perovskites with the same chemical composition as the polycrystalline usually show a higher decomposition temperature.[11] The enhanced thermal stability is critical for photovoltaics, especially those with focused light sources whereby the intense illumination will give rise to localized heating of the photoactive layers.

Single-crystal halide perovskites also show superiority in operational stability (Figures 4F and 4G).[11,125] Non-radiative carrier recombination induced by defects usually releases heat. Therefore, extensive non-radiative carrier recombination can potentially cause a severe rise in the device temperature and accelerate the material decomposition. This problem is critical in light-emitting diodes (LEDs), resulting in a notoriously short lifetime of the devices.[128] For example, it is reported that the lifetime of perovskite LEDs could be extended by reducing the Joule heat by passivating the traps with additives in $FAPbI_3$ precursors.[129] Single-crystal halide perovskites with low defect density can suppress the non-radiative recombination, leading to long-term operational stability, especially for LEDs with a shorter emitting wavelength that operate under a higher bias voltage and tend to generate a larger amount of heat. This enhanced thermal stability of single-crystal halide perovskites can potentially help realize long-term stable blue LEDs.

Facet, strain, and superlattice engineering

Epitaxial growth has been widely used in the semiconductor industry.[130,131] Through the epitaxial technique, high-quality single-crystal halide perovskite nano-/micro-structures with different crystallographic facets and orientations,[132–134] lattice strain,[135,136] and superlattice structures[137,138] have been grown, enabling many new avenues of fundamental studies and device applications.

By adopting halide perovskite bulk crystals with different chemical compositions and crystallographic orientations as the substrate, an epitaxial layer can be grown with various crystallographic orientations.[9,82,139,140] Besides, adding capping agents to the growth solution can change the surface energy of individual lattice planes during the nucleation and thus tailor the exposed facets of the final single crystals (Figure 5A).[141,142] Enclosed by different facets, halide perovskite single crystals tend to exhibit varying properties. For example, different facets grown by using different capping agents can be either p or n type because of the dissimilar dominant point defects on these facets:[143] the (100) facet with I^- vacancies of the $MAPbI_3$ single-crystal is found to be n type while the (112) facet with MA^+ and Pb^{2+} vacancies turns out to be p type. For another example, the optoelectronic performance of halide perovskites shows facet dependence.[142] Photocurrent measurements from different facets of single-crystal $MAPbI_3$ show that the (100) facet has a better photoresponse because of the reduced defect density on the (100) facet.[142] Facet engineering can have a profound impact on the performance of single-crystal halide perovskite devices.

Lattice strain can modify the electronic band structure of the epitaxial layer to enhance the existing functionality or even create new functionalities.[12,144,150] In polycrystalline perovskites, it is challenging to generate controllable and long-lasting strain due to the weak physical attachment of the polycrystalline to the substrate. Additionally, those grain boundaries in polycrystalline thin films can also facilitate the phase change because of the unbalanced strain between grains.[151,152] By epitaxial growth, the controllable and stable strain has been achieved in single-crystal halide perovskites by inducing lattice mismatch with the substrate.[12,144,153] Interfacial van der Waals forces have been exploited to tune the optical properties of halide perovskites due to the low moduli of halide perovskites.[144] Due to the relatively weak interfacial interactions, however, van der Waals epitaxy cannot achieve substantial strain in the halide perovskites.[144] Recently, large magnitudes of strain (2.4%) have been realized with strong interfacial chemical bonds. The lattice mismatch between the epitaxial layer and the substrate can be used as a continuously tunable knob to deform and create strain in the epitaxial lattice, which can consequently change the properties and functionalities of the materials.[154] Compressive strain is found to narrow the band gap and enhance the hole mobility in halide perovskites (Figures 5B and 5C).[12,153] In addition, compressive strain can

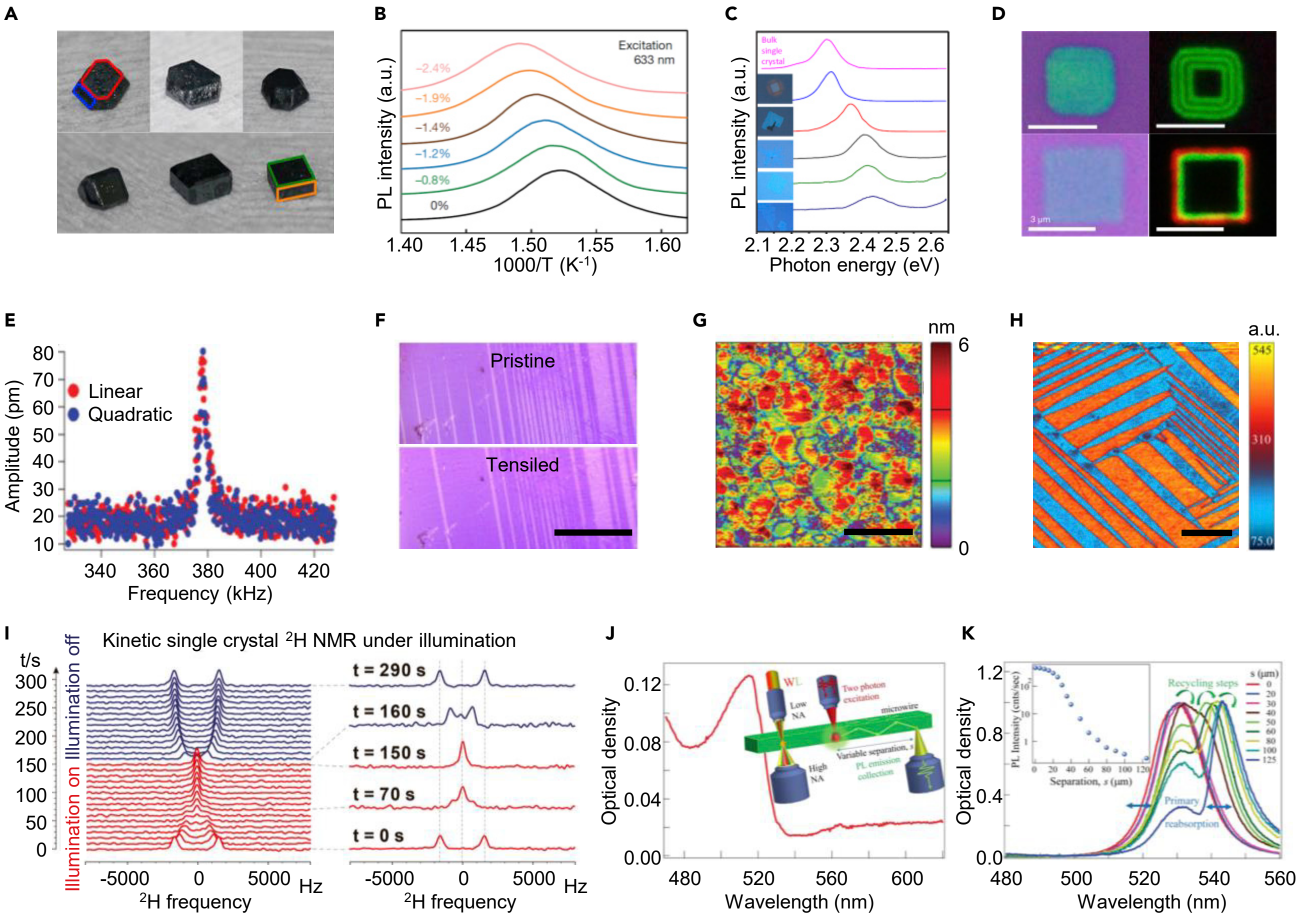

Figure 5. Facet, strain, superlattice, and ferroelectricity engineering in halide perovskites

(A) Facet engineering of halide perovskite single crystals by controlling the capping agent concentration.[142] Red, the (100) facet; blue, the (112) facet; orange, the (110) facet; and green, the (002) facet. Copyright 2017, American Chemical Society.

(B) Strain-dependent photoluminescent spectra of the epitaxial $FAPbI_3$, demonstrating that the strain can effectively tune the band gap and thus optical properties of halide perovskites.[12] Copyright 2020, Springer Nature.

(C) Thickness-dependent photoluminescent spectra of a $CsPbBr_3$ crystal grown by the van der Waals epitaxy.[144] The change in the thickness-dependent band gap is smaller compared with that of the freestanding one, demonstrating the weak interfacial interaction of the van der Waals epitaxy. The color contrast of the optical images of the $CsPbBr_3$ crystals on the left indicates their relative thicknesses. Copyright 2019, American Physical Society.

(D) Optical (left panels) and photoluminescent (right panels) images of periodically heterostructured halide perovskites.[10] Different colors on the right panels reveal the planar heterostructure with different band gaps. Scale bars, 3 μm. Copyright 2020, Springer Nature.

(E) Comparison of the linear (first harmonic) and quadratic (second harmonic) piezoelectric force microscopy response of $MAPbI_3$.[145] Results show that $MAPbI_3$ exhibits both linear and quadratic responses, indicating that $MAPbI_3$ might be ferroelectric. Copyright 2016, The Royal Society of Chemistry.

(F–H) (F) Polarized optical images of a $MAPbI_3$ under freestanding and tensile strain.[146] The stripe pattern changes under the tensile strain, which is the signature of ferroelasticity. Scale bar, 100 μm. Copyright 2020, Springer Nature. Amplitude mapping of (G) a polycrystalline[145] and (H) a single-crystal[147] $MAPbI_3$ thin film by piezoelectric force microscopy. The comparison shows the pattern in the single crystal is more regularly aligned than that of the polycrystalline, due to the absence of grain boundaries, point defects, and impurities in the single crystal. Scale bars, 500 nm (G) and 2 μm (H). Copyright 2018, Springer Nature.

(I) Dynamic ^2H-NMR spectra of a single-crystal halide perovskite.[148] Results reveal the dynamic reorientation of the organic cation MA^+ under illumination by probing the local chemistry of H atoms. Copyright 2020, Elsevier.

(J) A linear absorption spectrum of a single-crystal halide perovskite microwire. Inset: the schematic measurement setup.[149] Different photoluminescent spectra can be obtained by changing the distance between the laser and detector. Copyright 2018, American Chemical Society.

(K) Photoluminescent spectra of a single-crystal halide perovskite microwire with different excitation distances from the detector (from 0 μm to 125 μm), demonstrating the reabsorption process in halide perovskites.[149] Inset: photoluminescent intensity with different excitation distances from 0 μm to 125 μm. Copyright 2018, American Chemical Society.

structurally stabilize the phase of those metastable halide perovskites by anchoring the lattices of the epitaxial layer to those of the substrate,[12,155–157] which thus effectively broadens the library of halide perovskites for building stable devices.

Periodic alternation of the growth of two or more semiconductors with a controllable thickness (typically a few atomic layers) forms a superlattice or a multiple quantum well. Due to the quantum confinement and the coupling of adjacent electron wave functions, such structures can exhibit much-enhanced electronic properties, such as high quantum yield in lasers,[158] and even show new functionalities, such as superconductivity,[159] which are absent in their individual forms. Therefore, it is of great interest to achieve superlattice in halide perovskites, which can be potentially valuable for various applications. Recently, the periodically heterostructured growth of two halide perovskites with sub-100-nm thickness for each layer has been reported (Figure 5D).[10] The periodic heterostructure obviously enhanced the fluorescence intensity and shifted the emission wavelength because of the energy transfer between different layers of halide perovskites. Further developments in reducing the thickness of each layer to several atomic layers may help enhance the quantum confinement effect.[160]

Studies of intrinsic properties: Ferroelectricity and others

Defects in polycrystals would confound the measurements of physical properties of the material per se. Due to the much-reduced structural heterogeneities and disorders, single-crystal halide perovskites are considered to be better for studying the intrinsic properties of halide perovskites.

The existence of ferroelectricity in halide perovskites is still under hot debate (Figures 5E and 5F).[146,161–166] In general, ferroelectricity is identified by the existence of ferroelectric domain structures and the switching of polarization in the domains with electrical polling.[167] One of the debates in ferroelectricity measurements of halide perovskite states that the electrical polling triggers ion migration, leading to artificial switching rather than ferroelectric switching of polarization.[72,168] Other debating aspects suggest that the polling process may inject extra carriers into the halide perovskites, leading to an artificial dipole switching,[72] and the contribution of polar organic cations to the ferroelectricity of halide perovskites remains unclear.[169,170] While the high crystallinity does not create ferroelectricity in single-crystal halide perovskites, it can play an important role in determining the existence of ferroelectricity. The single crystal is free from grain boundaries and has a much-reduced impurity density, which leads to a more homogeneous and more accurately identified ferroelectric domain structure than the polycrystalline (Figures 5G and 5H).[171] Additionally, single-crystal halide perovskites can significantly suppress ion migration due to the lower point defect density and thus reduce the artifacts during electrical polling, which helps examine the existence of ferroelectricity.

Besides ferroelectricity, single crystals are conducive to studying the carrier-phonon coupling in halide perovskites, which helps understand the intrinsic limit of carrier dynamics and their photophysical properties.[172,173] The reduced point defects and absence of grain boundaries in the single-crystal halide perovskites minimize the scattering of free carriers and lead to more accurate measurements of these intrinsic properties.[173] Similarly, solid-state nuclear magnetic resonance probes the local chemical environment of atoms, which carries vast structural information of the material (Figure 5I).[174] In polycrystalline halide perovskites, atoms around the structural defects will suffer from severe local heterogeneous strain, which confounds the signals measured by the nuclear magnetic resonance. In single-crystal halide perovskites, the lack of such local heterogeneities leads to much-reduced measurement complexity.[148] Additionally, photon recycling/reabsorption plays an important role in the V_{OC} of perovskite solar cells and the efficiency of general optoelectronic devices.[42] Single crystals are free from scattering by grain boundaries and may directly facilitate the photon recycling process (Figures 5J and 5K).[175]

CURRENT GROWTH METHODS FOR SINGLE-CRYSTAL HALIDE PEROVSKITES

Researchers have established various kinds of procedures to grow single crystals of hybrid and even all-inorganic halide perovskites. While those procedures are different from each other, the key concept is the same, namely, crystallization from a well-controlled precursor environment. Because of the especially strong temperature-dependent solubility of perovskites in various solvents, solution-based crystallization is the most widely adopted method.

Bulk crystals

Bulk crystals of halide perovskites usually are not suitable for building devices, mainly because their large sizes strongly influence the internal carrier extractions and result in strong carrier recombination. Nonetheless, high-quality bulk crystals are great for fundamental studies of structural,[12] mechanical,[176,177] semiconductive,[85,122] and ferroelectric[178,179] properties of halide perovskites. Many methods have been reported to grow bulk crystal halide perovskites of high quality, large size, and high throughput.

The Bridgman method

By this method, large single-crystal halide perovskites are grown inside sealed ampoules.[180,181] Powdered materials and seeds are filled inside a quartz ampoule under an inert or vacuum environment (Figure 6A). The crucible filled with the precursor powder is then moved to the hot zone of the furnace and kept as such. After the powder melts, the quartz ampoule is moved with a certain velocity toward the cold zone of the furnace. Crystals start to nucleate at the crucible tip at specific temperatures. The crystallization facade then starts to propagate through the melted powder. Usually organic compounds have high vapor pressure and are chemically unstable at their melting point, so the Bridgman method is not suitable for hybrid halide perovskite and can only grow all-inorganic halide perovskite single crystals, such as the solid-state reaction processed $CsPbBr_3$[182,183] and lead-free $CsSnI_3$ by mixing CsI and SnI_2.[184]

Slow evaporation

Slow evaporation is well known as the simplest method to obtain single crystals. In a mixed precursor solution, the solvent naturally evaporates, typically under controlled heating, until crystallization takes place (Figure 6B). A saturated solution is required to grow the crystals; otherwise, the crystallization process will not happen or be delayed until the solution is saturated upon solvent evaporation. Despite its simplicity, this method is less attempted because of the long-time required. Single crystals of BA_2PbX_4 (BA is benzyl ammonium) have been grown by this method.[185] The use of mixed solvents (dimethylformamide and dimethylsulfoxide) can not only increase the solubility of the precursors but also accelerate the evaporation rate of low-vapor pressure dimethylformamide and reduce the time required.

Inverse temperature crystallization

The inverse temperature crystallization (ITC) method is based on an unusual retrograde solubility regime whereby the solubility decreases in a specific organic solvent or solvents when the temperature increases (Figure 6C).[85] As the temperature rises, the solution gradually reaches supersaturation. The nucleation appears at some point, followed by crystal growth. Choosing the appropriate solvent is the key to

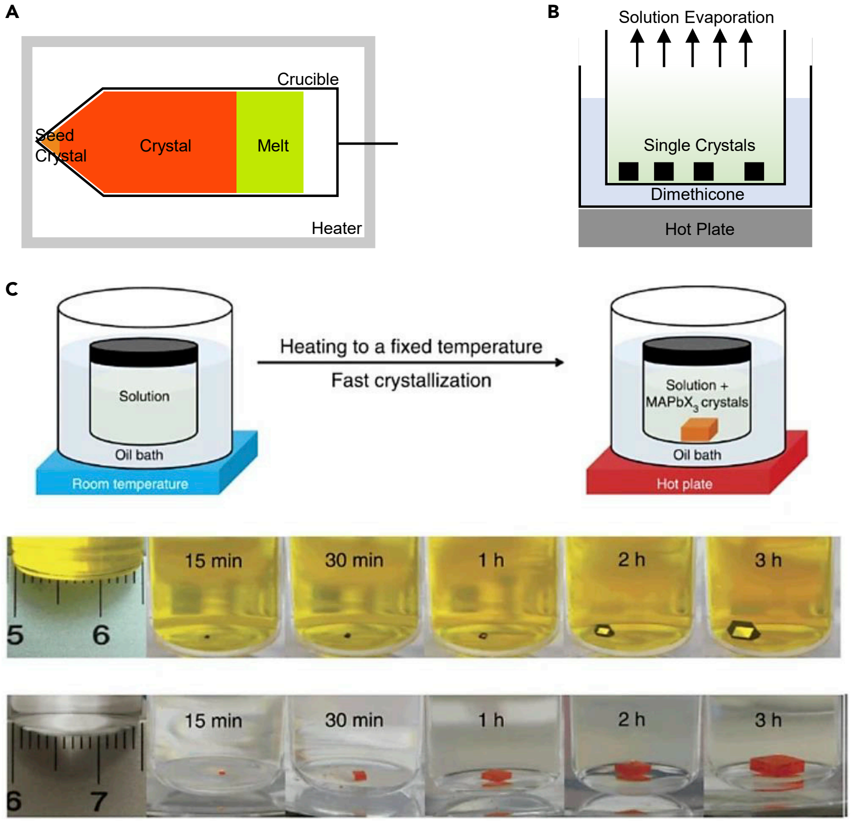

Figure 6. Growth methods for halide perovskite bulk crystals

(A) A schematic setup for growing crystals by the Bridgeman method. Powders and seeds are filled in a quartz ampoule and moved to a hot furnace until melting, after which the quartz ampoule is moved with a certain velocity toward the cold zone of the furnace until crystallization.

(B) A schematic setup for growing crystals using the slow evaporation method. In a saturated precursor solution, the solvent naturally evaporates under heating to drive crystallization and growth.

(C) A schematic setup for growing crystals using the ITC method and optical images of the as-grown crystals at different stages. As the temperature increases, the solution gradually reaches supersaturation, followed by nucleation and crystal growth.[85] Copyright 2015, Springer Nature.

growing high-quality halide perovskite single-crystals. In 3D perovskites, crystallization can easily happen because of the strong relation between temperatures and perovskite solubility in several specific solvents[41] (e.g., dimethylformamide for $MAPbBr_3$,[186] dimethylsulfoxide for $MAPbCl_3$,[187] and γ-butyrolactone for $MAPbI_3$[85]), which allows them to grow into a large single crystal rather than many small crystals. In addition to the hybrid halide perovskites, it is also possible to grow all-inorganic single-crystal halide perovskites with this method, such as $CsPbBr_3$ using dimethylsulfoxide as the solvent under ambient conditions.[188] However, the ITC method is not very suitable for 2D perovskites, whose solubility in common solvents is too high to form crystals rather than amorphous colloids.

Modifying steps of the ITC method, very-large-sized single-crystal halide perovskites can be grown. First, the growth precursor is dissolved in a suitable solution and subjected to high temperatures overnight. The precursors' solubility gradually decreases, which leads to a homogeneous nucleation process, forming multiple small crystals (1–2 mm in size). Second, a seed crystal with good morphology and high integrity is chosen and positioned inside a freshly prepared saturated precursor solution. This solution is then subsequently subjected to heating. The seed crystal will promote heterogeneous nucleation, yielding a larger crystal (~7 mm in size),[41] which can be used as a seed crystal for another round of growth. An iterative process can yield crystals as large as 1,000 cm^3.[189]

Micro-/nanocrystals

Nanostructured halide perovskites have been deemed desirable candidates for some electronic and optoelectronic applications,[190,191] especially in light-emitting devices,[192–194] due to their unique quantum confinement effect, which can result in superb electrical and photophysical properties beyond those of their bulk counterparts.

Micro-/nanoplates

To date, both vapor-phase and solution-phase methods have been used to synthesize halide perovskite micro-/nanoplates, with the former being more widely adopted.[195–197] $MAPbX_3$ (X = Br^-, Cl^-, and I^-) micro-/nanoplatelets were firstly fabricated by a vapor-phase conversion from halide platelets to corresponding perovskite platelets.[194] However, impurities and defects were easily formed using this method because of the insufficient conversion process. To solve this problem, a more efficient vapor-phase method was reported by using dual precursor sources simultaneously in the reaction system (Figure 7A).[197] The as-prepared platelets approached sub-10 nm in thickness and several micrometers in lateral dimensions, with excellent crystal qualities, suggesting that the vapor-phase method is very efficient for the preparation of perovskite micro-/nanostructures.

Micro-/nanoplates of $MAPbBr_3$[201] and $CsPbBr_3$[198] could be synthesized in solution by using a colloidal approach (Figure 7B). From the reported solution-phase methods, low reaction temperature and extra introduced solvents (e.g., acetone) play key roles in the shape control. It was empirically found that only acetone could efficiently trigger the nucleation of platelets of many Br-based halide perovskites,[198,201] while other solvents facilitated nanocrystal nucleation and growth. It is likely that acetone can slowly destabilize the complexes of Cs^+ and Pb^{2+} with various molecules in solution and therefore set the trigger for the nucleation of the platelets, which is not observed in other polar solvents such as isopropanol or ethanol.[198] The addition of ethanol, for example, led to the quick formation of large nanoparticles (20–40 nm in size), most likely due to the excessive destabilization of the initial metal complexes.[198]

Micro-/nanowires

Micro-/nanowires feature a higher degree of anisotropy, which provides a high-speed channel for the directional transport and propagation of photons and charge carriers. By taking advantage of such unique characteristics, micro-/nanowires with intriguing electrical and photophysical properties have been demonstrated, attracting interests for fundamental studies and various applications.

Similarly, halide perovskite micro-/nanowires can be synthesized by both vapor-phase and solution-phase methods. The first solution-growth strategy to prepare $MAPbI_3$ micro-/nanowires was reported in 2015 (Figure 7C).[199] Lead acetate thin film was firstly deposited on a glass substrate and then exposed to an organic MAI precursor solution. Unlike the widely used inorganic PbI_2 precursor, the lead acetate precursor prefers to form micro-/nanowires rather than the typical cubes. The same method can be applied to other halide perovskites such as $MAPbBr_3$ and $MAPbCl_3$ by replacing the corresponding organic precursors. By using the lead

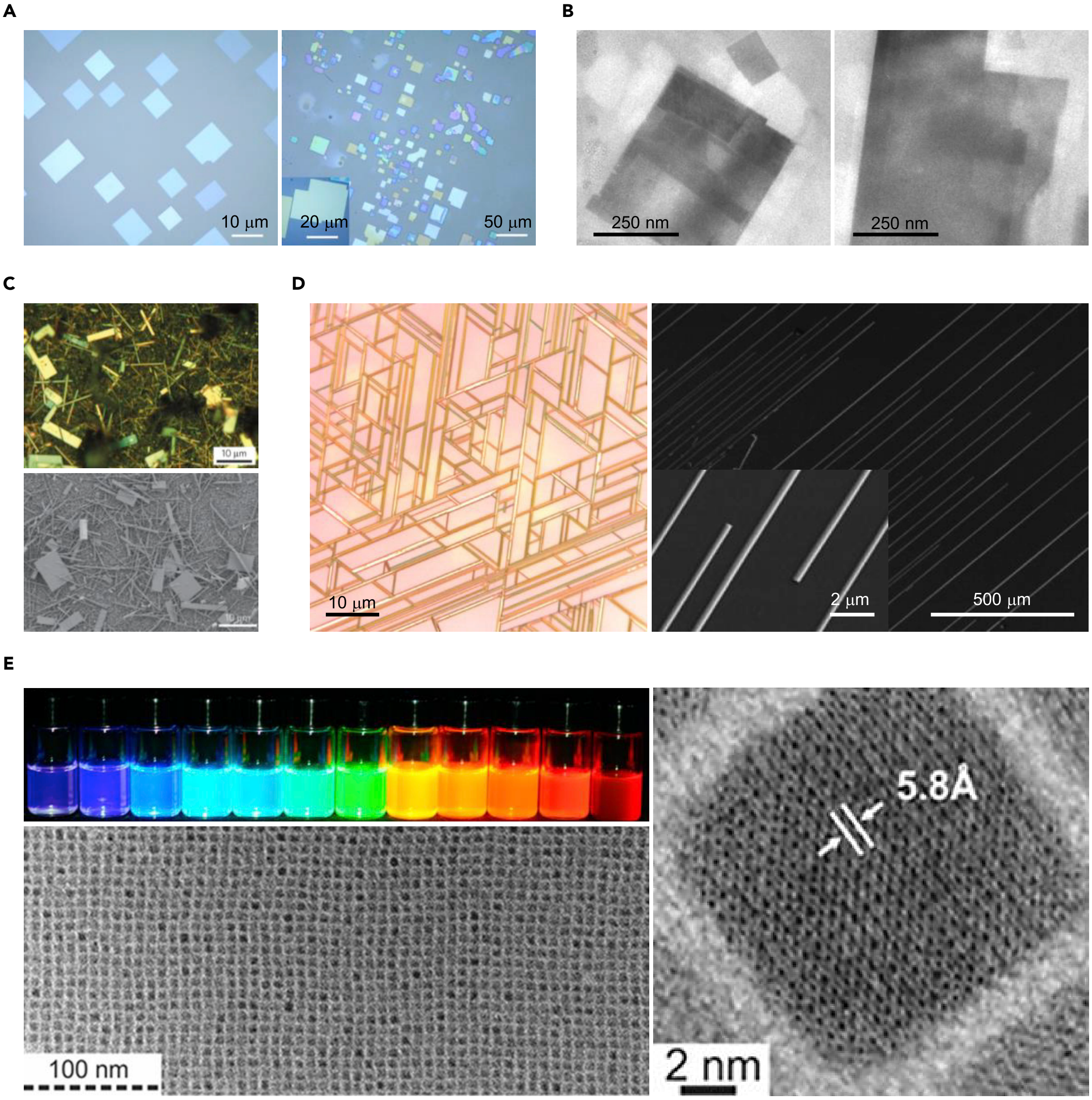

Figure 7. Growth methods for halide perovskite micro-/nanocrystal

(A) Optical images of the single-crystal $MAPbBr_3$ micro-/nanoplates grown by a vapor-phase method.[197] Copyright 2015, American Chemical Society.

(B) Transmission electron microscopy images of the single-crystal $CsPbBr_3$ micro-/nanoplates grown by a solution-phase method.[198] Copyright 2016, American Chemical Society.

(C) Optical and scanning electron microscopy images of the single-crystal $MAPbI_3$ micro-/nanowires grown by a solution-phase method. Lead acetate precursor is found to be the key factor for forming micro-/nanowires. A high aspect ratio (length up to 20 μm and width of several hundred nanometers) can be realized.[199] Copyright 2015, Springer Nature.

(D) Optical images of the $CsPbBr_3$ micro-/nanowires grown by a vapor-phase method on mica (left) and sapphire (right) substrates. The growth is considered to be governed by the van der Waals force.[139] Copyright 2017, American Chemical Society.

(E) Optical and transmission electron microscopy images of the perovskite quantum dots grown by the hot injection method. By tuning the precursor component, quantum dots of a series of band gaps can be obtained.[200] Copyright 2015, American Chemical Society.

acetate as the inorganic precursor, the as-grown micro-/nanowires can exhibit superior crystal qualities with a high aspect ratio (length up to 20 μm and width of several hundreds of nanometers).[199] Later, by using the $PbCl_2$ precursor with a different anti-solvent diffusion-induced crystallization strategy, the as-crystallized $MAPbCl_3$ perovskites, which should be cubes in principle, were found to be micro-/nanowires.[202] Even though the mechanism of morphology change is still not clear, the kinds of antisolvents were found to be related to the micro-/nanowire morphologies, with toluene resulting in the highest aspect ratio (length ~45 μm and width ~500 nm).[202]

The vapor-phase methods are more often reported for synthesizing all-inorganic halide perovskite micro-/nanowires. The growth mechanism is generally considered to be the van der Waals force.[153,203] On mica and sapphire substrates, $CsPbBr_3$ micro-/nanowires were easily grown via a vapor-phase process (Figure 7D).[134,139,204,205] Regardless of the substrate and the precursor source, a long reaction time and a high reaction pressure were found to be critical for forming the micro-/nanowire structures.

Quantum dots

With a controllable size and uniform size distribution, halide perovskite quantum dots exhibit tunable quantum confinement effects, which allow for efficient color emissions. There have been numerous reports on the synthesis of halide perovskite quantum dots,[200,206–208] with a key common concept, namely, hot injection.

Typical hot injection synthesis involves heating the required precursors to a certain temperature under gas protection and quickly injecting the hot precursors into another solution. Via a quick ionic metathesis reaction, quantum dots can be obtained (Figure 7E).[200] In this method, the nucleation stage happens directly after the injection, and the growth stage starts afterward. The separation between the two stages allows the achievement of narrow size distribution of the quantum dots.[209] The operating temperature and the injection time play important roles in controlling the size of the obtained quantum dots.[210] The high reaction temperature also enables better control over the shape and phase purity of the quantum dots, which may be due to the instant crystallization process without a growth window.[211] Both hybrid and all-inorganic perovskite quantum dots can be obtained with this method.[200]

However, a low emission quantum yield of those as-obtained quantum dots is commonly observed, which is considered to be due to the unstable, uncoordinated surface atoms.[212] By choosing different organic ligands and solvents in the precursor solutions,[207,208,213–215] which can passivate the defect and prohibit the non-radiative carrier recombination of the quantum dots, the emission quantum yield of halide perovskite has been improved from the original ~20%[206] to now ~95%.[216,217]

Thin films

Bulk crystals (typically >1 mm in thickness) suffer from inefficient extraction of charge carriers in electronics, whose carrier diffusion length (typically 5–10 μm[218,219]) is far below their crystal dimensions. Neither are nanostructures ideal for fabricating devices. The interface between the nanostructures can impede the transport of free carriers over a long range, in a way similar to the grain boundaries in the polycrystalline materials. Therefore, single-crystal thin films with proper thicknesses are ideal for extracting charge carriers. Additionally, thin films are compatible with processes for device integration, which typically requires multilayered stacking of different functional materials.

Slicing

After the halide perovskite bulky crystals are grown, they can be sliced into thin wafers (Figure 8A).[220] With this method, single-crystal wafers of $FAPbI_3$ and $MAPbI_3$ with sizes of more than 20 mm and thicknesses as low as 100 μm have been achieved using a diamond wire. An additional wet etching step by dissolving the $FAPbI_3$ and

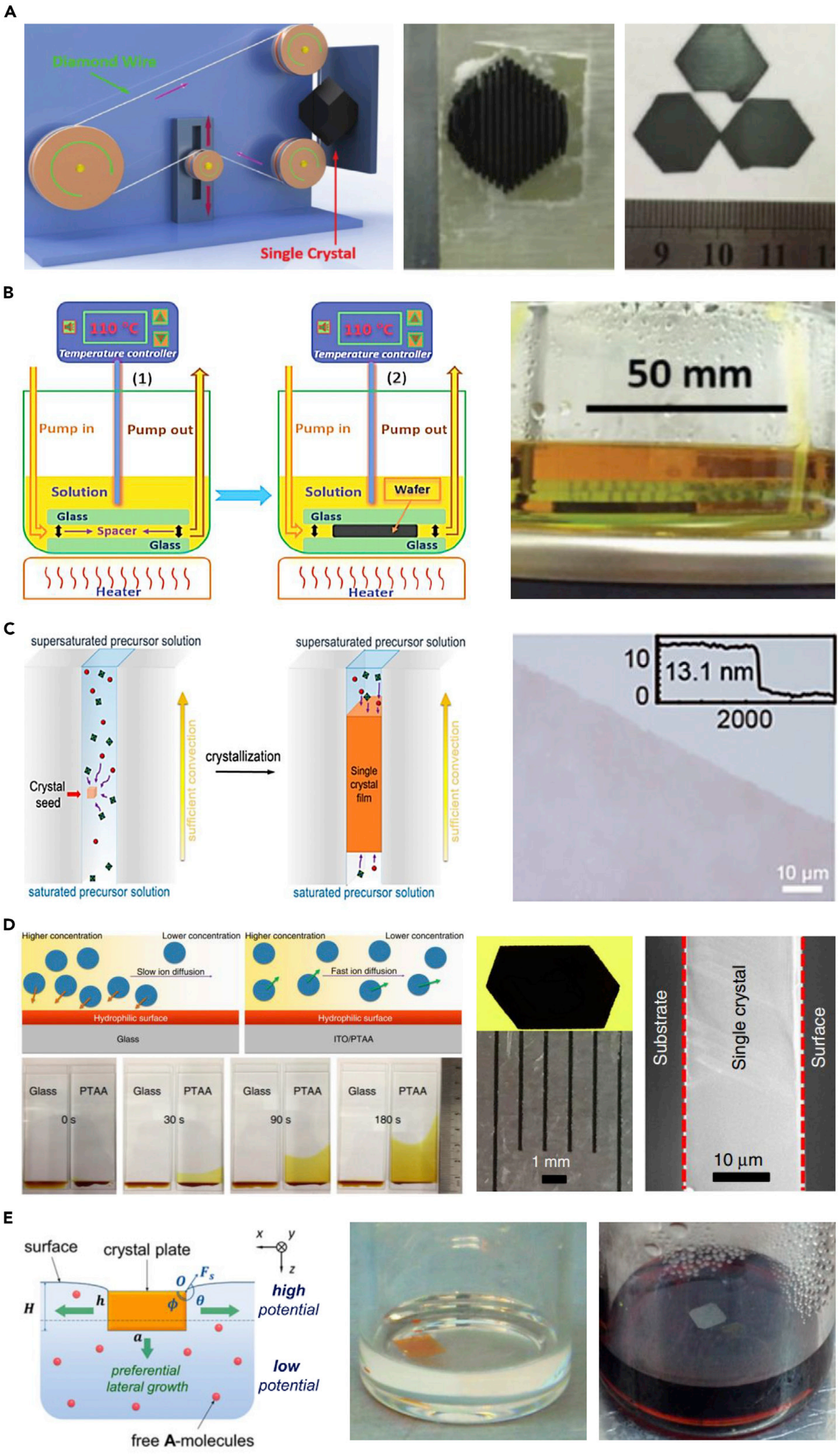
A
Diamond Wire
Single Crystal
9 10 11 1
B
110 °C
Temperature controller
(1)
Pump in
Pump out
Solution
Glass
Spacer
Glass
Heater
110 °C
Temperature controller
(2)
Pump in
Pump out
Solution
Wafer
Glass
Glass
Heater
50 mm
C
supersaturated precursor solution
Crystal seed
sufficient convection
saturated precursor solution
crystallization
supersaturated precursor solution
Single crystal film
sufficient convection
saturated precursor solution
10
0
13.1 nm
2000
10 μm
D
Higher concentration
Lower concentration
Slow ion diffusion
Hydrophilic surface
Glass
Higher concentration
Lower concentration
Fast ion diffusion
Hydrophilic surface
ITO/PTAA
Glass
PTAA
0 s
Glass
PTAA
30 s
Glass
PTAA
90 s
Glass
PTAA
180 s
1 mm
Substrate
Single crystal
Surface
10 μm
E
surface
crystal plate
x
y
z
O
F_s
h
ϕ
θ
H
a
high potential
low potential
preferential lateral growth
free A-molecules

Figure 8. Fabrication methods for single-crystal halide perovskite thin films

(A) A schematic setup and optical images of the single-crystal wafers made by the slicing method. Bulk single crystals are sliced by diamond wires into pieces of thin single-crystal wafers.[220] Copyright 2016, John Wiley and Sons.

(B) A schematic setup and an optical image of the space-confinement method. A geometrically defined dynamic flow reaction system is used to grow single-crystal thin films. A peristaltic pump provides constant transport of fresh solutions for continuous crystal growth.[222] Copyright 2016, John Wiley and Sons.

(C) Schematics and an optical image of the modified space-confinement method. Two flat substrates vertically clip together are immersed in the precursor solution. Changing the clipping force can effectively tune the film thickness. $MAPbBr_3$ single crystals of a thickness of 13 nm can be obtained.[223] Copyright 2016, American Chemical Society.

(D) Schematics of the modified space-confinement method, and optical and scanning electron microscopy images of the as-grown single crystals. A hydrophobic interface of the clapping substrate can effectively reduce the wettability of the substrates and lead to favored precursor transportation. A millimeter-sized thin single crystal with ~20 μm thickness can be obtained.[224] Copyright 2017, Springer Nature.

(E) A schematic setup and optical images of the surface-tension-controlled ITC method. The large intermolecular distances in the surface layer due to surface-tension effects decrease the molecular interaction energies, which can be translated into a faster lateral growth rate along the solution surface than that along the thickness direction into the solution bulk.[225] Copyright 2017, American Chemical Society.

$MAPbI_3$ crystals in γ-butyrolactone can further reduce the thickness to ~15 μm.[221] However, mechanical slicing of those thin, brittle crystals normally causes fractures inside, which also can serve as trap states to impede charge transport and thus irreversibly degrade both mechanical and electrical properties of the as-fabricated thin films. Additionally, because of the unbalanced solubility in the solvents, the etching rates for the organic and inorganic components are different. Consequently, wet etching may also largely increase the surface trap density by forming various reactive defects in the partially etched perovskite structures.

Space confinement

Combining the ITC method and a geometrically defined dynamic flow reaction system can grow single-crystal thin films.[222] A peristaltic pump provides mass transport of fresh solution for continuous crystal growth. The resultant single-crystal $MAPbI_3$ thin films can possess a relatively large size of up to 1 cm, and the thickness can be controlled to be as thin as 150 μm (Figure 8B). The film thickness can be further controlled by two flat substrates clipped together that are vertically immersed into the perovskite-precursor solution (Figure 8C).[223] The gap size of the two substrates can be tuned by changing the clipping force, and hence the film thickness of the resulting $MAPbBr_3$ can be adjusted to be as thin as 13 nm. Using this method, different types of single-crystal halide perovskite thin films have been grown successfully on various substrates, including quartz, indium tin oxide (ITO), Si, and polyethylene terephthalate.

Unfortunately, the sizes of the single-crystal thin films grown with the clipped templates are too small (typically only hundreds of micrometers in footprint) to be effectively applied in devices. A further improvement of the clipped template method has been demonstrated with a hydrophobic interface facilitated diffusion strategy.[224] The growth substrates were coated with a hydrophobic hole-transport material poly[bis(4-phenyl) (2,4,6-trimethylphenyl)amine] (PTAA), which can effectively reduce the wettability of the substrates and lead to favored precursor transportation (Figure 8D).[224] As a consequence, millimeter-sized single-crystal halide perovskite ($MAPbI_3$ and $MAPbBr_3$) thin films with thicknesses of tens of micrometers have been achieved.

A surface tension-controlled ITC strategy was also developed to achieve preferential growth in the lateral direction at the solution surface.[225] The intermolecular distances in the surface layer are larger due to surface-tension effects, which decreases the corresponding molecular interaction energies. The resultant growth barrier at the surface layer is lower than that in the bulk solution, which can lead to a faster

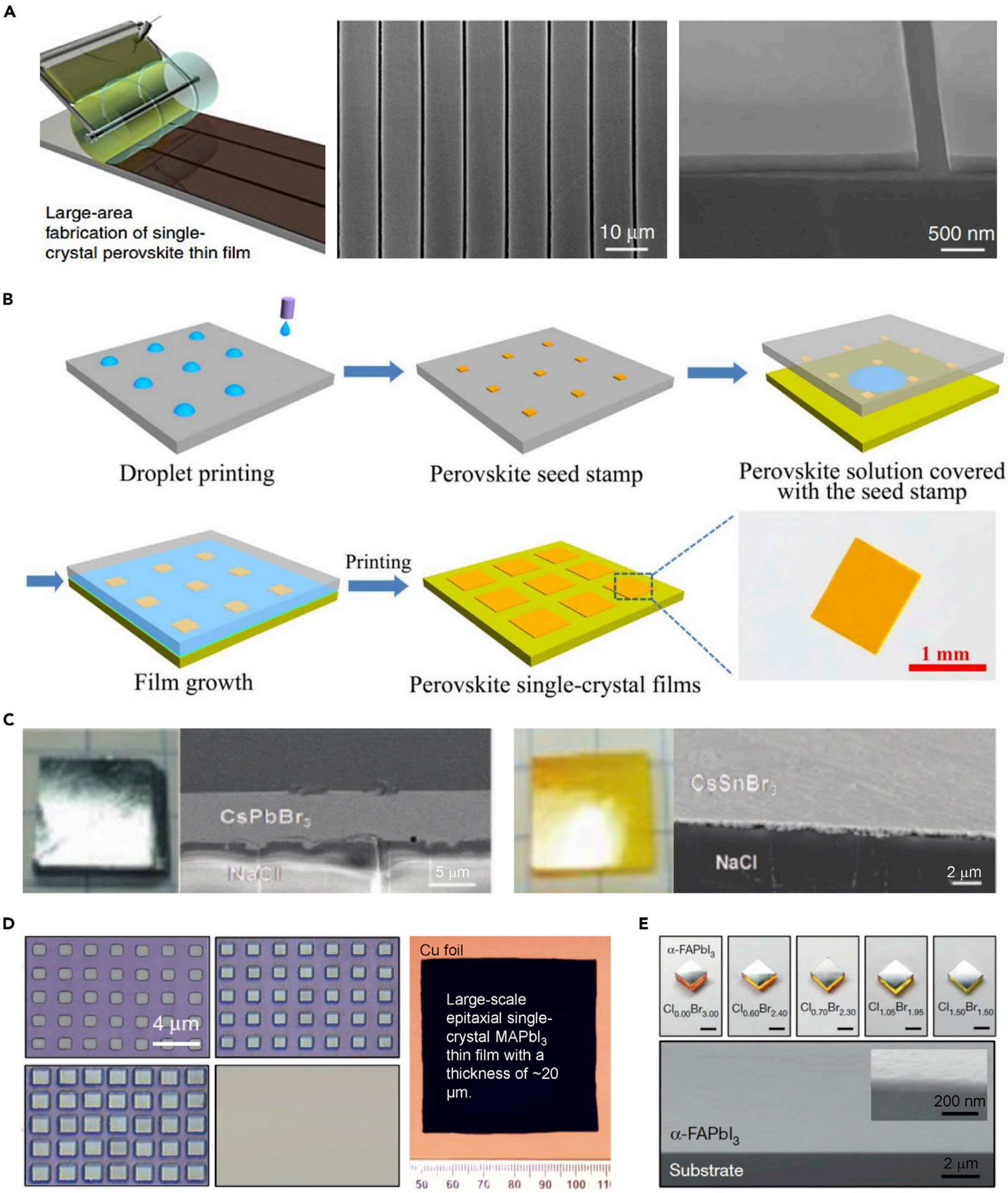

Figure 9. More fabrication methods for single-crystal halide perovskite thin films

(A) A schematic setup of the roll-printing method and scanning electron microscopy images of the as-grown thin films. Inch-scale single-crystal $MAPbI_3$ thin-film stripes can be obtained.[226] Copyright 2017, Springer Nature.

(B) Schematics of the stamping method and an optical image of the as-grown thin film. An array of perovskite seeds is grown and stamped to a substrate, which undergoes the space-confined solvent evaporation-induced crystallization process. Arrayed single-crystal thin films with sizes of millimeters and thicknesses of nanometers to micrometers can be obtained.[227] Copyright 2018, American Association for the Advancement of Science.

(C) Optical and scanning electron microscopy images of the single-crystal $CsPbBr_3$ and $CsSnBr_3$ thin films grown on single-crystal alkali halides substrates by a vapor-phase epitaxial method. The obtained single-crystal halide perovskite thin films exhibit adjustable thicknesses from 200 nm to 7 mm and sizes up to 1 cm × 1 cm.[228] Copyright 2017, John Wiley and Sons.

(D) Optical images of the single-crystal thin films grown by the solution-based lithography-assisted epitaxial method. Individual epitaxial crystals can merge together to form a single-crystal thin film due to their identical crystal orientation.[229] Copyright 2020, Springer Nature.

Figure 9. *Continued*

(E) Optical and scanning electron microscopy images of strained single-crystal thin films grown by the solution-based epitaxial method. Single-crystal α-$FAPbI_3$ thin films can be grown on a series of lattice-mismatched halide perovskite substrates (top). Scale bars, 4 mm. A suitable embedded strain level will enhance the hole mobility without causing high densities of defects in the epitaxial layers.[12] Copyright 2020, Springer Nature.

lateral growth rate along the solution surface than that along the thickness direction into the solution bulk (Figure 8E). Using this strategy, various single-crystal halide perovskite thin films (including $MAPbBr_3$, $MAPbI_3$, and $MASnBr_3$) with areas up to 1 cm^2 and thicknesses of 5–20 μm have been grown at the solvent surface.

Roll-printing

Compared with the discrete single crystals with limited areas that are commonly grown via spatially confined solution methods, producing continuous uniform wafer-scale single-crystal halide perovskite thin films is highly desired but challenging. A facile roll-printing technique was developed to fabricate inch-scale single-crystal $MAPbI_3$ thin films (Figure 9A).[226] In this solvent evaporation-induced crystallization process, a customized channel-patterned rolling mold was used to transfer the perovskite ink solution onto a preheated substrate, leading to immediate evaporation of the solvent and, thus, instant crystallization of halide perovskites. The geometrical confinement of the mold can restrict the crystal growth in the thickness direction to the submicrometer scale. The instant crystallization under a controlled temperature plays an important role in controlling the growth behavior so that the precursor would contribute to the growth of already formed seed crystals, rather than forming new seed crystals and yielding random polycrystalline structures.

Stamping

Seeded growth by solvent evaporation is slow, but an array of seeded growth in parallel can increase the growth throughput. The stamping method is based on combining the seeded growth with space confinement. An array of perovskite seeds was stamped onto a substrate, which underwent the space-confined solvent evaporation-induced crystallization process (Figure 9B).[227] To prepare the stamped seed array, perovskite inks are printed onto a temporary substrate, and ordered perovskite seeds are then formed as the ink droplets evaporate. The seed stamp is then transferred to a target substrate with a saturated precursor solution inside. The stamped seed array promotes heterogeneous nucleation and significantly inhibits random homogeneous nucleation. As the solvent gradually evaporates at room temperature, single-crystal thin films with patterned geometries can grow on the seeds that are uniformly distributed across the entire substrate. The result is the scalable growth of single-crystal halide perovskite thin-film arrays, with each piece being millimeters in size and controllable thicknesses of from hundreds of nanometers to >10 μm. This method has been demonstrated to be suitable for $MAPbBr_3$, $MAPbCl_3$, $MAPbI_3$, $CsPbBr_3$, and BA_2PbBr_4.

Vapor-phase epitaxy

Vapor-phase epitaxy has been demonstrated as a powerful technique to grow high-quality single-crystal halide perovskite thin films. However, because of the high growth temperature, the lattice constant and thermal expansion coefficient of the halide perovskite should be matched with those of the substrate, which limits the choice of substrates and halide perovskites to be grown. Monocrystalline alkali halides have been used as the substrate for the growth of all-inorganic single-crystal halide perovskite thin films (e.g., $CsPbBr_3$ and $CsSnBr_3$) due to their similar material chemistries and lattice constants (Figure 9C).[228] The obtained single-crystal halide perovskite thin films exhibited smooth surfaces with a uniform and adjustable thickness from 200 nm to 7 mm and a size up to 1 cm × 1 cm. Similarly, single-crystal $CsPbBr_3$ thin films with a controllable micrometer-scale thickness and an area of

0.5 cm × 1 cm have been grown on the (100) facet of $SrTiO_3$ substrates through the vapor-phase epitaxial method.[230] Despite the distinct differences in the lattice constants between the $SrTiO_3$ substrate and $CsPbBr_3$, two unit cells of $CsPbBr_3$ can be aligned with three unit cells of $SrTiO_3$ with a very low lattice mismatch.[230] During the growth, the high reaction temperature accelerates atomic diffusion, which efficiently increases the nucleation density and further facilitates the growth of thin films.

Even under optimized conditions, vapor-phase epitaxial growth still does not have good growth coverage on the substrate, leading to a low growth throughput. Also, the structural phase is prone to change during the process of cooling from the high growth temperature, resulting in uncontrollable lattice relaxation or breakdown of the epitaxial relationship, which increases the dislocation concentration in the as-grown crystals. To control the dislocation concentration and also study the related carrier dynamics in perovskites, a remote epitaxy approach using polar substrates coated with a layer of graphene has been demonstrated.[203] With graphene as a buffer layer, $CsPbBr_3$ can be grown on the graphene/CaF_2 substrate. The weak film-substrate coupling in remote epitaxy largely suppresses the nucleation of new crystals and promotes growth on existing crystals, yielding large-sized crystal domains. The as-grown thin film has low-density dislocations because of the low interfacial energy mediated by the graphene buffer layer. However, considering the totally different lattice structure between $CsPbBr_3$ and graphene, it is also possible that the $CsPbBr_3$ crystals might have nucleated on the CaF_2 substrate through the pinholes of the graphene. Nevertheless, compared with conventional ionic epitaxy, the remote epitaxy suppresses the generation of dislocations and related carrier recombination, which largely enhances the carrier lifetime.

Solution-based epitaxy

Solution-based epitaxy allows the formation of stable interfacial chemical bonds for controllable and uniform epitaxial growth.[231] Compared with vapor-phase epitaxy, solution-based epitaxy can have a much higher growth coverage because of the uniform contact between the substrate and the growth precursor. Halide perovskite bulk crystals can be used as the substrate. By tailoring the composition of the bulk crystals, the growth can be either homoepitaxy[11,82] or heteroepitaxy.[12]

A solution-based lithography-assisted epitaxial growth method has been reported to fabricate single-crystal thin films of general halide perovskites (Figure 9D).[11,82] A general halide perovskite bulk crystal was used as the substrate. To prevent the halide perovskites from decomposing in solution (e.g., developers and etchants), a hermetic layer of parylene-C polymer was used to seal the bulk crystal substrate. After a patterned mask was formed on the parylene-C the substrate surface was exposed by dry-etching the parylene-C. Using the combined epitaxial growth and microfabrication, the crystal's growth behavior, including thickness (as thin as 600 nm), area (as large as 5.5 cm × 5.5 cm), morphology (thin films, rods, and cubes), orientation (along <001>, <110>, and <111>), and composition (e.g., by alloying different cations and anions) could be controlled. In particular, by continuously changing the growth precursor's composition, the composition of the single-crystal thin film could be continuously changed, forming a gradient composition and thus a graded band gap along the thickness direction of the thin film. The graded band gap is valuable for charge carrier separation and collection, similar to the function of a built-in potential at the interface of p-n junctions.

By adopting a similar growth process, strain was embedded inside the epitaxial thin film when the compositions of the thin film and the bulk crystal substrate were different (Figure 9E).[12] By carefully designing the level of lattice mismatch, a series

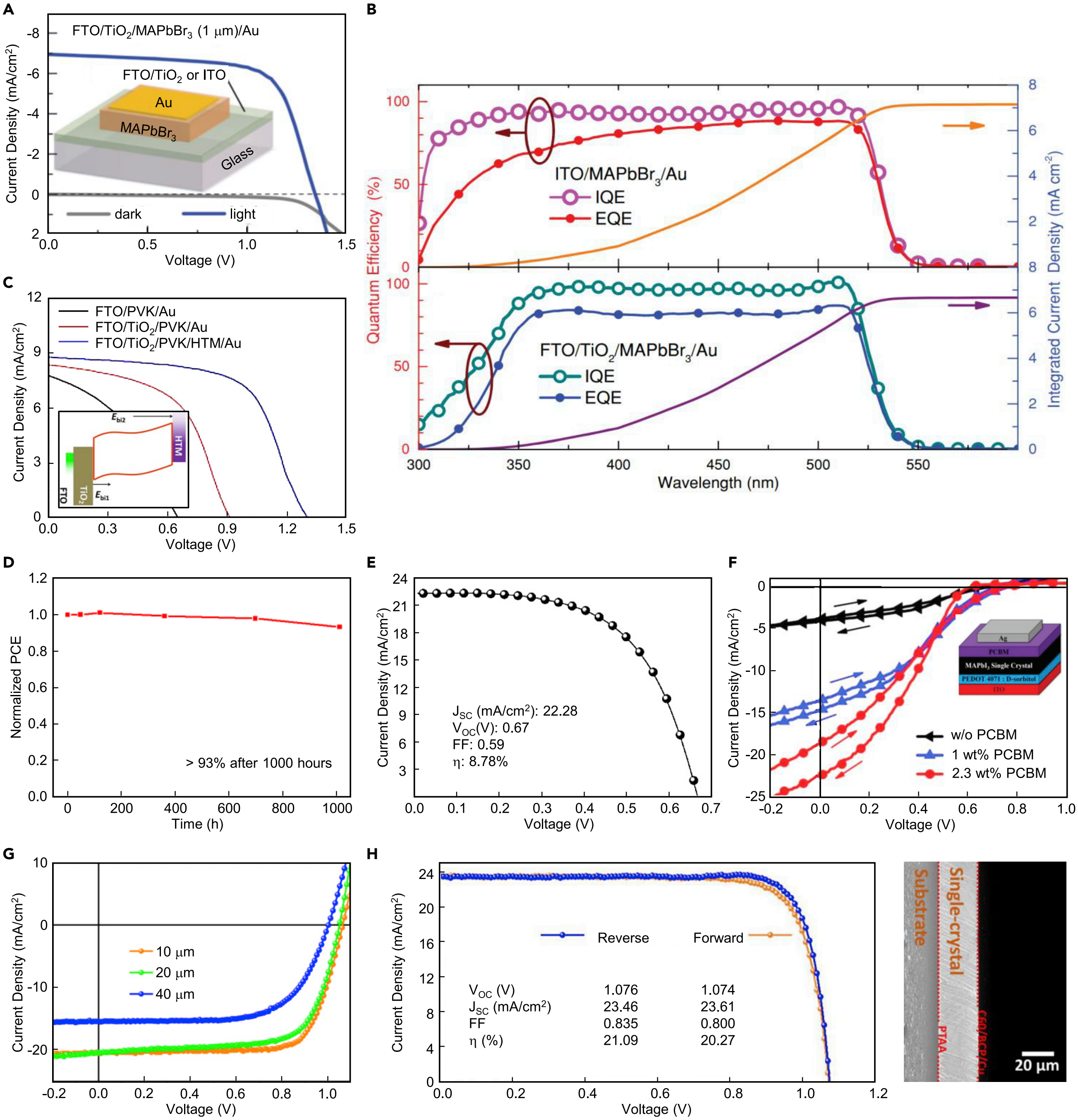

Figure 10. Single-crystal halide perovskite solar cells

(A) *J-V* curves of a 1-μm-thick single-crystal MAPbBr$_3$ solar cell. The low efficiency is considered to be from the wide band gap of the absorber and the absence of the hole-transport layer.[261] Copyright 2016, John Wiley and Sons.

(B) Quantum efficiency measurements of a 1-μm-thick single-crystal MAPbBr$_3$ solar cell. The high internal quantum efficiency suggests very efficient intrinsic carrier transport in the single-crystal absorber, but the low external quantum efficiency indicates that a more optimized structural design is needed.[261] Copyright 2016, John Wiley and Sons.

(C) *J-V* curves of a 16-μm-thick single-crystal MAPbBr$_3$ solar cell. The efficiency is obviously improved by forming a better-aligned energy band structure with an electron transport layer and a hole-transport layer.[262] Copyright 2017, The Royal Society of Chemistry.

(D) Superb stability of a single-crystal MAPbBr$_3$ solar cell.[262] Copyright 2017, The Royal Society of Chemistry.

(E) *J-V* curve of a 15-μm-thick single-crystal MAPbI$_3$ solar cell. Replacing MAPbBr$_3$ with MAPbI$_3$ provides a more suitable absorption range to improve the solar cell efficiency.[263] Copyright 2017, Elsevier.

Figure 10. *Continued*

(F) *J-V* curves of 15-μm-thick single-crystal $MAPbI_3$ solar cells with different structures. Changing the device structure cannot further improve the efficiency, indicating that the absorber thickness may be the bottleneck.[264] Copyright 2018, John Wiley and Sons.

(G) *J-V* curves of single-crystal $MAPbI_3$ solar cells. Decreasing the absorber thickness results in better device efficiencies. A remarkable 17.8% efficiency is achieved with a 10-μm-thick absorber. The decreased absorber thickness is critical for efficient charge extraction and minimal carrier recombination.[224] Copyright 2017, Springer Nature.

(H) *J-V* curves (left) of an optimized 10-μm-thick single-crystal $MAPbI_3$ solar cell (right). Record efficiency of 21.1% for single-crystal halide perovskite solar cells is achieved.[265] Copyright 2019, American Chemical Society.

of lattice strain, as large as 2.4%, can be effectively coded into the halide perovskite thin films. The embedded compressive strain was shown to not only change the crystal structure but also reduce the effective mass and thus increase the hole mobility in $FAPbI_3$. Additionally, the compressive strain was unexpectedly able to stabilize certain metastable halide perovskites (e.g., the photoactive α-$FAPbI_3$ that would otherwise phase change to the photoinactive δ-$FAPbI_3$) and extend its lifetime from 24 h to almost a year. This controllable strain engineering in perovskites may open up new directions for high-performance semiconducting electronics.

SINGLE-CRYSTAL HALIDE PEROVSKITE DEVICES

Halide perovskites have demonstrated exciting potential in multiple fields, including solar cells,[18,19,27,232–234] photodetectors,[101,109,229,235–238] LEDs,[129,239–241] lasers,[58,242–246] and many others.[246–252] Besides the excellent electrical properties, single crystals show much-enhanced device stability compared with their polycrystalline counterparts. Because of their well-aligned lattice structures,[11,12] the single-crystals are not as vulnerable as the polycrystalline thin films to the common stability risk factors, such as phase change,[253–255] annealing-induced lattice expansion,[256] and rapid cation decomposition.[257]

Solar cells

Halide perovskites have been intensively applied for developing photovoltaics during the past few years. However, the current record efficiency for perovskite solar cells is still far from their theoretical Shockley-Queisser limit (e.g., ~30.5% for a single-junction cell based on $MAPbI_3$). Additionally, the poor stability becomes the realistic limitation for future improvements as well as commercializing perovskite solar cells. Polycrystalline thin-film halide perovskite solar cells, with currently the most efficient structure,[232] have been proved to suffer from high defect levels, massive grain boundaries, and rapid ion migrations,[119,258] which are the major problems for the short device lifetime. In contrast, single-crystal halide perovskites are free from grain boundaries, showing not only low defect levels[79] and suppressed ion migrations[11,119] but also dramatically enhanced optoelectronic properties, which are promising for improving device performance and stability.

Compared with the widely studied polycrystalline halide perovskite solar cells, reports on their single-crystal counterparts are very few. One of the major challenges is the typically large thickness of the single-crystal halide perovskite absorber, which is orders of magnitude thicker than the polycrystalline thin films (500–900 nm).[232,259] The large thickness of the single-crystal absorbers results in a weak built-in field, a high carrier recombination rate, and therefore a poor charge-extraction efficiency. It is critical to improve the fabrication protocols and reduce the single-crystal film thickness.[260]

Single-crystal $MAPbBr_3$ has been used as an absorber for solar cells, with a power conversion efficiency (PCE) of 6.53% (Figure 10A).[261] The measured high internal quantum efficiency suggests very efficient intrinsic carrier transport in the single-crystal absorber (Figure 10B). However, the external quantum efficiency drops

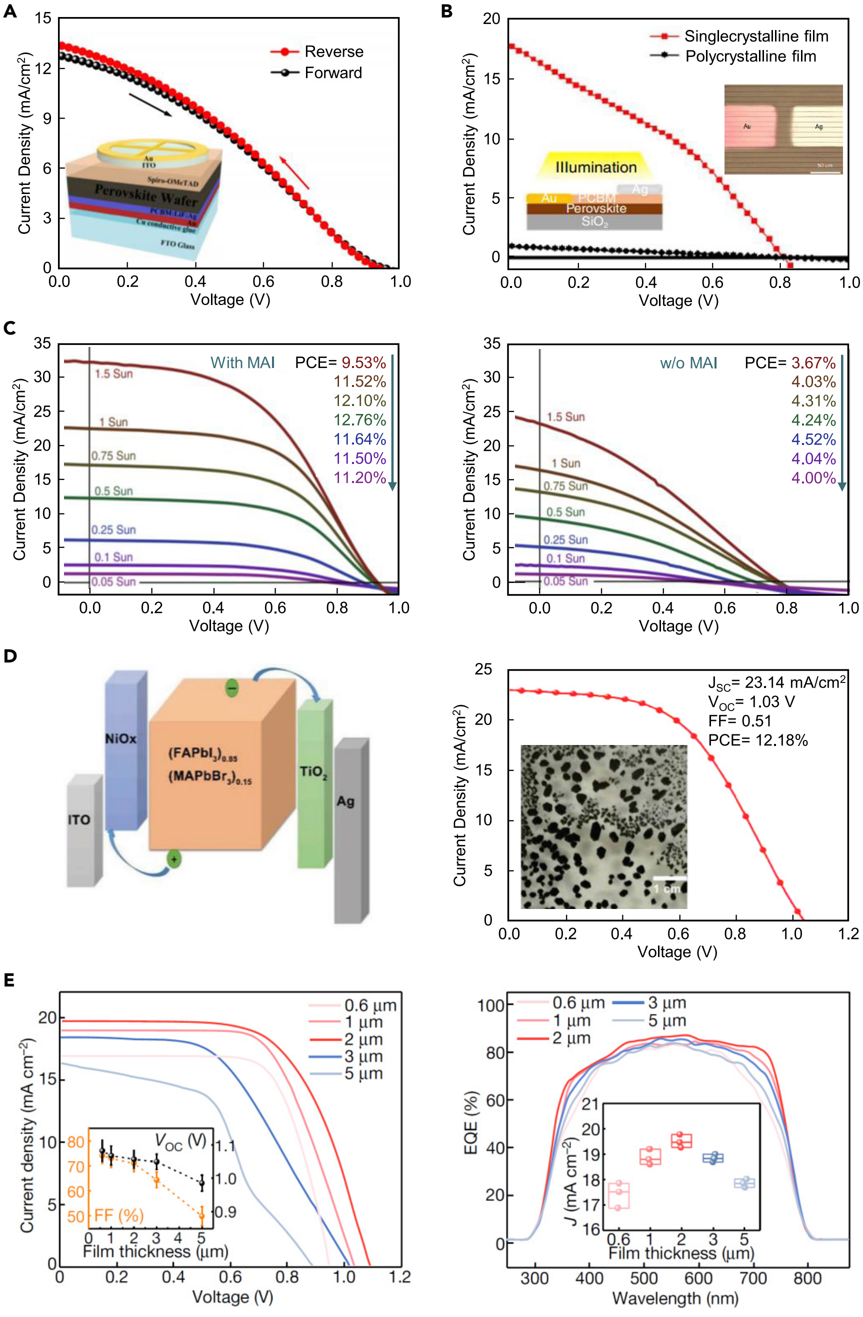

Figure 11. Scalable and band gap engineering in single-crystal halide perovskite solar cells

(A) *J-V* curves of a 50-μm-thick single-crystal $MAPbI_3$ solar cell. This solar cell is based on a ~120 mm × 120 mm wafer.[267] Copyright 2017, Springer Nature.

(B) *J-V* curves of a 200-nm-thick single-crystal $MAPbI_3$ solar cell. This wafer-scale solar cell is fabricated by the roll-printing method with a lateral device structure.[226] Copyright 2017, Springer Nature.

(C) *J-V* curves of laterally structured single-crystal $MAPbI_3$ solar cells with optimized surface conditions. The MAI (left) and the MAI-free (right) treatments are investigated. The MAI-treated devices exhibit better PCE over different light intensities, suggesting that the surface of the single-crystal $MAPbI_3$ can be passivated by the MAI.[125] Copyright 2020, Springer Nature.

(D) Band-gap engineering of the single-crystal absorber. A 24.5-μm-thick mixed single-crystal $(FAPbI_3)_{0.85}(MAPbBr_3)_{0.15}$ can achieve better energy alignments and device performance (left).

Figure 11. ***Continued***

The *J-V* curve from the best device (right), showing a PCE of 12.18%. The inset is an optical image of $(FAPbI_3)_{0.85}(MAPbBr_3)_{0.15}$ thin single crystals.[269] Copyright 2018, John Wiley and Sons.

(E) *J-V* curves of single-crystal $MAPbI_3$ solar cells (left) and related external quantum efficiencies (right) with different absorber thicknesses. The FF, V_{OC}, and J_{SC} are found to be highly related to the thin-film thickness, where an optimized thickness is ~2 μm.[11]. Copyright 2020, Springer Nature.

demonstrably compared with its internal quantum efficiency, suggesting that a more optimized structural design is needed for carrier extraction and collection. Later, the efficiency of single-crystal $MAPbBr_3$ solar cells was improved to 7.11% by optimizing both the electron and the hole-transport layers to form a better-aligned energy band structure (Figure 10C).[262] Additionally, the single-crystal $MAPbBr_3$ solar cells exhibited much better stability than the polycrystalline counterpart under one-sun illumination and could maintain 93% of their initial PCE after aging in dry air without encapsulation for 1,000 h (Figure 10D).[262] However, compared with the polycrystalline solar cell, the improvement in the efficiency of single-crystal solar cells was rather limited even with optimized electron and hole-transport layers, indicating that the device layout and structural design should not be the bottleneck for high efficiency. The overall mediocre efficiency of the single-crystal $MAPbBr_3$ solar cells was considered to arise from the narrow absorption range of $MAPbBr_3$.

Replacing $MAPbBr_3$ with a halide perovskite of a more suitable absorption range promised to improve the single-crystal solar cell efficiency. $MAPbI_3$ has a smaller band gap of ~1.7 eV and can serve as a better absorber than the $MAPbBr_3$ of ~2.3 eV. Single-crystal $MAPbI_3$ solar cells with an $FTO/TiO_2/MAPbI_3$/2,2′,7,7′-tetrakis(*N*,*N*-di-*p*-methoxyphenylamine)-9,9′spirobifluorene (Spiro-OMeTAD)/Ag structure achieved a PCE of 8.78% with an absorber thickness of ~15 μm (Figure 10E).[263] The low FF and V_{OC}) in the current density-voltage curve were the major problems in limiting the PCE,[263] even with different electron and hole-transport layers (Figure 10F).[264] The major reasons for these relatively low FF and V_{OC} in single-crystal $MAPbI_3$ solar cells were still considered to be the relatively thick absorber[224] and the resulting strong interfacial carrier accumulation.[266]

By further decreasing the absorber thickness to 10 μm, the single-crystal $MAPbI_3$ solar cells with an $ITO/PTAA/MAPbI_3/PCBM/C_{60}$/bathocuproine/Cu structure demonstrated a much-improved efficiency of 17.8% (Figure 10G).[224] Such a stepwise efficiency improvement was attributed to the decreased absorber thickness, whereby efficient charge extraction and minimal carrier recombination led to the relatively high FF and V_{OC}. Later, an optimized experimental procedure realized a high PCE of 21.1% with the same device structure.[265] The best device based on a 10-μm-thick single-crystal $MAPbI_3$ reached an ultrahigh FF of 83.5% (Figure 10H), indicating extremely efficient internal carrier-transport dynamics and a very strong built-in field. Compared with the efficient polycrystalline halide perovskite solar cells whose absorber thickness is around 500–800 nm, more detailed studies are needed to understand the thickness-dependent carrier dynamics in single-crystal solar cells to further improve the PCE.

For the aforementioned $MAPbI_3$ solar cells, all of the single crystals were grown using the space-confinement method and had relatively small areas. $MAPbI_3$ solar cells with large areas were fabricated using diced 50-μm-thick large wafers. The resulting PCE was ~4% with a device structure of Au/ITO/Spiro-OMeTAD/$MAPbI_3$/PCBM/LiF/Ag/Au (Figure 11A).[267] The thick absorber and, thus, low FF were still the major reasons for the relatively poor PCE. To control the thickness of large-area single-crystal halide perovskite thin films, a roll-to-roll printing method was demonstrated for making wafer-scale single-crystal $MAPbI_3$ with designed patterns, whose thickness could be down to ~200 nm (Figure 11B).[226] However, because this method had strict requirements regarding the substrate roughness and was operated under a high temperature, the as-fabricated single-crystal thin films could only be integrated into solar cells in a lateral structure without a hole-transport layer, which limited the PCE to only 4.83%. Recently, the PCE of laterally structured single-crystal $MAPbI_3$ solar cells was improved to ~11% by introducing a surface precursor treatment process (Figure 11C).[125] However, the lack of a hole-transport layer still remains unsolved, which was also a major challenge for other laterally structured solar cells.[268]

To achieve a high efficiency, the band gap of the halide perovskite needs to be engineered to be close to ~1.4 eV, which can absorb the most solar energy according to the Shockley-Queisser limit.[74] Therefore, the band gap of $MAPbI_3$ is still too large to be ideal. In polycrystalline perovskite solar cells, narrow-band-gap α-$FAPbI_3$ is used to replace the $MAPbI_3$ for a higher PCE. However, pure α-$FAPbI_3$ is not stable at room temperature. To achieve a single-crystal absorber with suitable band gap and structural stability, an effective way is to alloy different kinds of cations/atoms to form a mixed halide perovskite.[16,232] A mixed single-crystal $(FAPbI_3)_{0.85}(MAPbBr_3)_{0.15}$ solar cell with an ITO/NiO_x/$(FAPbI_3)_{0.85}(MAPbBr_3)_{0.15}$/$TiO_2$/Ag structure was reported with the highest PCE of 12.18% and an absorber thickness of 24.5 μm (Figure 11D).[269] Even though a more efficient band structure could be formed, the relatively low FF and V_{OC} still revealed that either the crystal was too thick or there was too much interlayer carrier recombination.

Using the solution-based lithography-assisted epitaxial growth method as mentioned above, thin (from 600 nm to tens of micrometers), large-area (~25 cm^2), and composition-tunable single-crystal halide perovskite films were demonstrated.[11] The as-fabricated flexible single-crystal $MAPb_xSn_{1-x}I_3$ solar cells, with an ITO/SnO_2/$MAPb_xSn_{1-x}I_3$/Spiro-OMeTAD/Au structure, exhibited an average of 17%–19% PCE and much-enhanced stabilities. The FF, V_{OC}, and short-circuit density (J_{SC}) were found to be highly related to the perovskite film thickness, suggesting that a comprehensive and detailed understanding of these aspects may further improve the device performance (Figure 11E).

Photodetectors

The valuable optical and charge-transport properties of halide perovskites have enabled their wide deployment as photodetectors, whose performance (e.g., responsivity,[270] response speed,[111,227,270] and detectivity[270,271]) have been largely improved over the years in polycrystalline halide perovskite thin films. Single-crystal halide perovskite thin films hold promise to further improve the photodetector performance.

Unlike solar cells, whose complicated design in structures and layout can significantly affect the device performance, photodetectors are relatively more straightforward. Existing single-crystal halide perovskite photodetectors can be classified into two structural types: the planar type, where the two electrodes are assembled on the same surface of the absorber, and the vertical type, where the perovskite layer needs to be sandwiched between two electrodes.

Planar-type photodetectors, because of their ease of fabrication, are most commonly reported. As shown in Figure 12A, a single-crystal $MAPbI_3$ photodetector array was fabricated in a planar structure, whose photocurrent response was ≈350-fold higher than that of the polycrystalline thin films.[222] Moreover, the fabrication of large photodetector arrays on single-crystal halide perovskite wafers is compatible

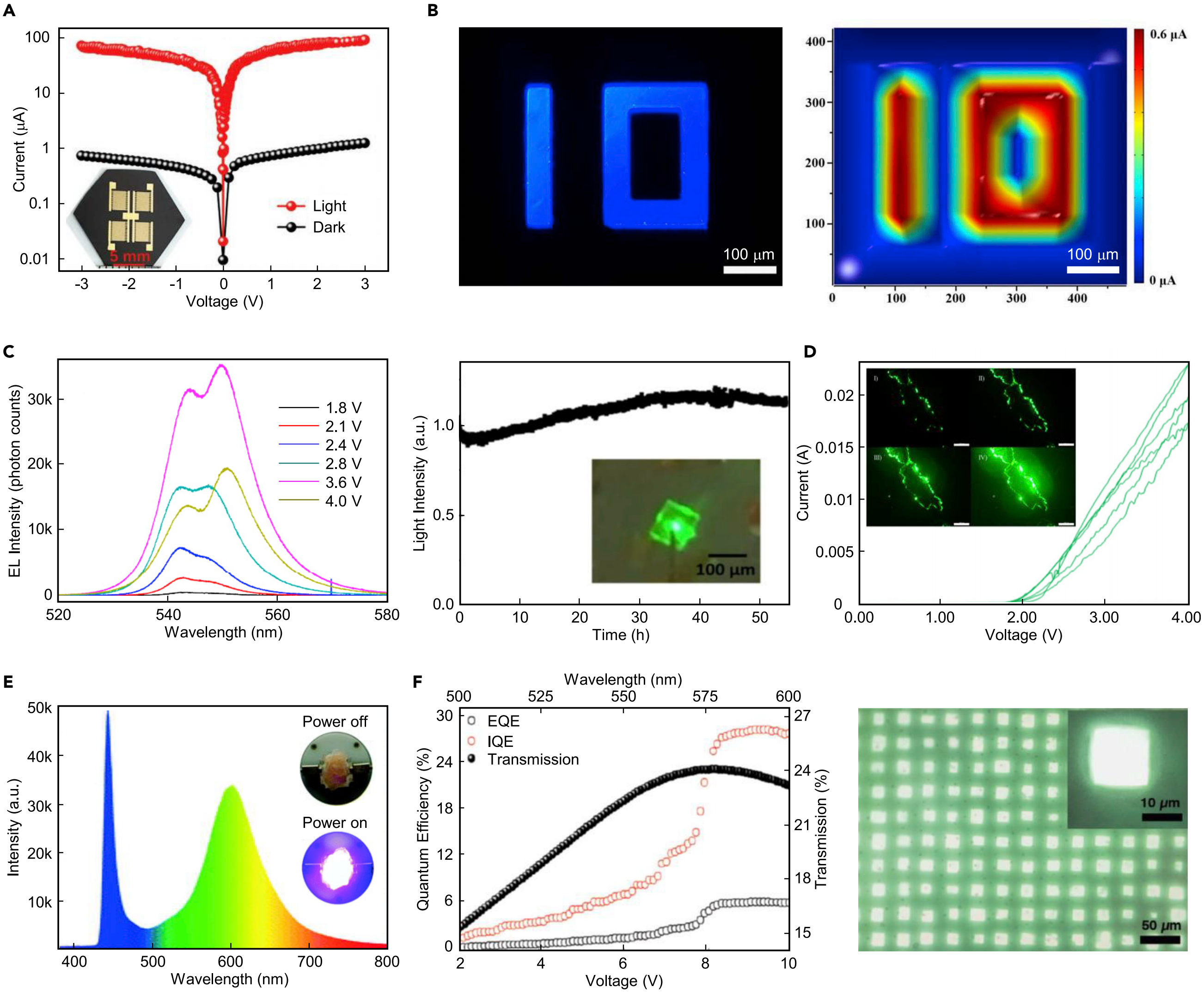

Figure 12. Single-crystal halide perovskite photodetectors and light-emitting diodes

(A) A planar structured single-crystal $MAPbI_3$ photodetector array. The photocurrent response is much higher (≈350 times) than that of the polycrystalline thin films.[222] Copyright 2016, John Wiley and Sons.

(B) A large photodetector array on a single-crystal $MAPbI_3$ wafer for imaging.[227] Copyright 2018, American Association for the Advancement of Science.

(C) A single-crystal $MAPbBr_3$ LED fabricated by depositing halide perovskite microplatelets onto an ITO-glass substrate without any transport layers. The device shows a driving voltage as low as 1.8 V (left). Illuminating at 5,000 $cd \cdot m^{-2}$ with high brightness and color purity can last continuously for 54 h under a liquid-nitrogen temperature, showing the single crystals' stability (right).[272] Copyright 2017, American Chemical Society.

(D) A single-crystal $MAPbBr_3$ LED without any transport layers operated from 2 to 4 V. Blinked emission at the crystal edges at a subsecond time interval is observed, possibly due to low electrical injection caused by the sub-band-gap states and the non-radiative carrier traps.[273] Scale bars, 200 μm. Copyright 2018, IOP publishing.

(E) A transport-layer-free 2D layered $(CH_3NH_3)_2MnCl_4$ single-crystal LED exhibits red luminescence with a quantum efficiency of 2.4%. The lack of transport layers prevents further improving the device performance.[274] Copyright 2019, The Royal Society of Chemistry.

(F) The first single-crystal halide perovskite LED array with an integrated hole transport layer, showing largely improved external quantum efficiency to ~7.1% (left). An optical image of the $MAPbBr_3$ array under operation is shown on the right.[82] Copyright 2018, John Wiley and Sons.

with the mass productions of integrated circuits. Similar results based on large-area single-crystal halide perovskite wafers have also been demonstrated for imaging (Figure 12B).[227] Additionally, flexible planar-type photodetectors based on low-dimensional single-crystal phenylethylamine lead iodide $(PEA)_2PbI_4$ have been demonstrated.[270] The single-crystal $(PEA)_2PbI_4$ exhibited low defect density, superior uniformity, and long-term stability, which resulted in a series of flexible photosensors with a very high external quantum efficiency of 26,530%, responsivity of 98.17 $A\cdot W^{-1}$, and detectivity of 1.62×10^{15} $cm\cdot Hz^{1/2}\cdot W^{-1}$ (Jones).

For the vertical-type photodetector, similar to the solar cells, the crystal thickness has a crucial influence on the device performance. A vertical-type photodetector with a small thickness should exhibit better performance than its planar-type counterpart because of the better structural design for charge collection and the larger active region. Note that for high-energy radiations (e.g., X-ray and γ-ray),[275] a vertical-type perovskite detector with a large thickness is more efficient than a small thickness because thick crystals are more prone to fully absorb those high-energy photons. The fabrication condition for vertical-type photodetectors is very similar to that of solar cells, whose key challenge is to form the single-crystal thin film and integrate it with the other functional layers in the device. The bulk crystal photodetectors with a thickness on the millimeter or submillimeter scale have always shown low responsivity due to substantial charge recombination.[271] Using ultrathin single-crystal $MAPbBr_3$ as the absorbers was proved to dramatically improve the photodetector performance.[73,271,276,277]

By integrating appropriate carrier-transport layers in the vertical device structure, photodiode-based photodetectors have been demonstrated.[12,278] Compared with the photoconductor-based photodetectors that only need two electrodes, the photodiode-based photodetectors with carrier-transport layers do not need an external power source. Without careful optimization of each layer and their interfaces, the photodiode-based photodetectors normally have very low external quantum efficiency (less than 1%[278–280]) if no current amplification or photomultiplication are applied.[281–283] The photodiode-based photodetectors can be operated at relatively low voltages and exhibit much faster response owing to their rather small thickness of the photoactive layers and, therefore, better carrier transport across these layers. Additionally, strain engineering has been found to further decrease the carrier effective mass and enhance the carrier mobility, which leads to an even faster response in the photodiode-type photodetectors.[12] Similarly to the solar cells, further improving the vertical-type photodetectors requires a more sophisticated structural and interfacial design of the devices.

Light-emitting diodes

Halide perovskites in the polycrystalline form have exhibited strong potential as an ideal emitting material with high external quantum efficiency, weak Auger recombination, and high color purity.[272] Therefore, their high-quality single-crystal counterparts with a long carrier lifetime and the absence of grain boundaries are highly expected to exhibit more stable and efficient electroluminescence.

The first single-crystal $MAPbBr_3$ microplatelet-based LED was reported with a simple structure of ITO/$MAPbBr_3$/Au without any electron or hole-transport layers.[272] The single-crystal LEDs were fabricated by depositing microplatelets onto an ITO-glass substrate, and emitted at 2.3 eV with a low onset bias of 1.8 V. Note that the optical emission energy in electron volts is even higher than the bias voltage, probably due to a barrier-free injection of the free charge carriers,[272] but the exact mechanism remains unclear. By quenching ionic migrations at a liquid-nitrogen temperature, the LED could sustain a continuous operation for 54 h at 5,000 $cd\cdot m^{-2}$ without degradation of brightness or shift of the emission wavelength (Figure 12C), showing that the single-crystal halide perovskites can be potentially applied in LEDs with high brightness and color purity. However, the device size (~100 μm × 100 μm) was too small for practical applications, and no electron or hole-transport layers could be integrated, largely limiting the

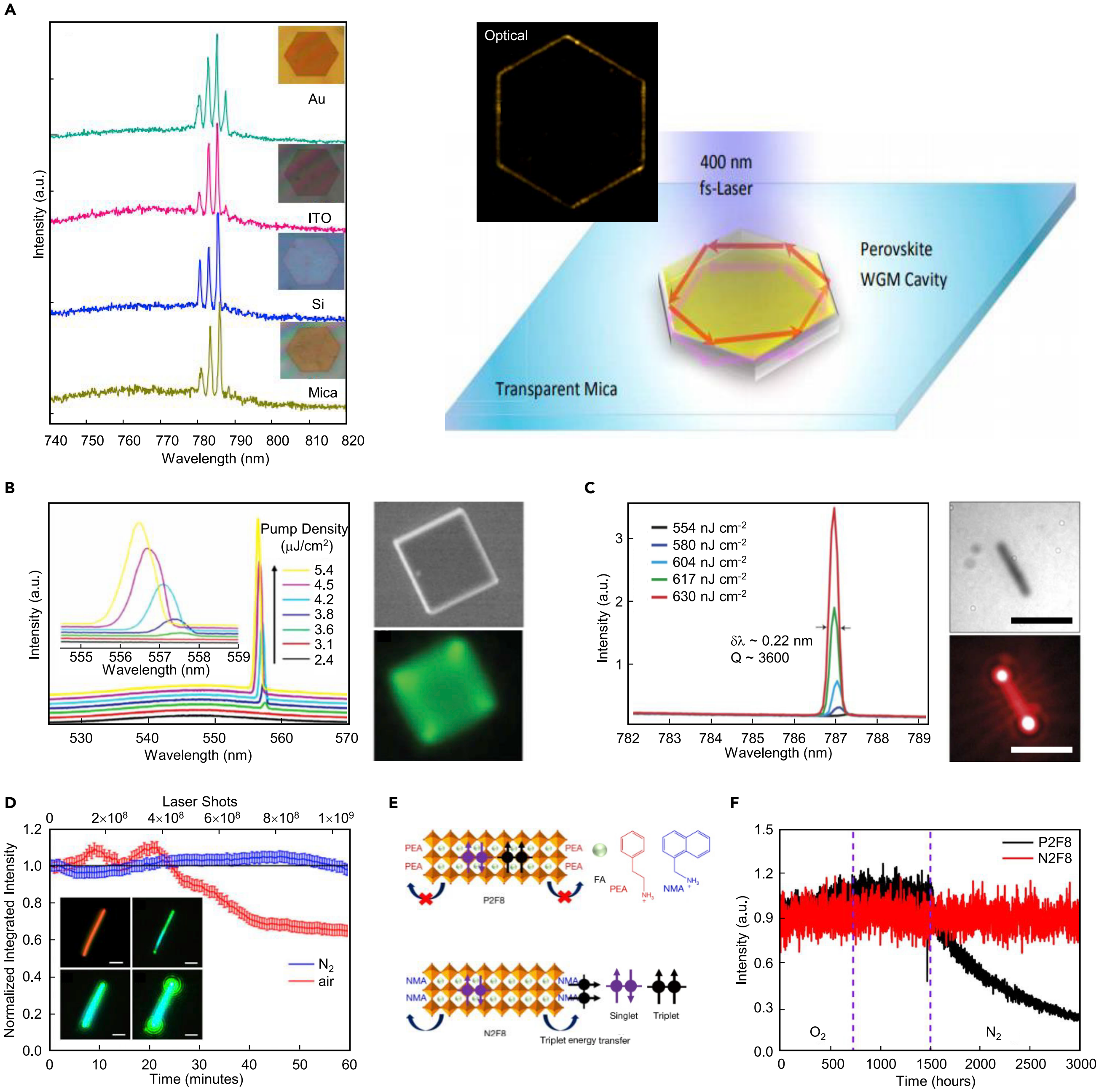

Figure 13. Single-crystal halide perovskite lasers

(A) The first demonstrated optically pumped laser based on single-crystal nanoplates of $MAPbI_3$ on various substrates (left). An optical image and schematics reveal the lasing mechanism (right). The thickness and edge lengths are 150 nm and 32 μm, respectively.[194] Copyright 2014, American Chemical Society.

(B) An optically pumped single-crystal $MAPbBr_3$ square microdisk laser, showing a low threshold ($3.6 \pm 0.5\ \mu J \cdot cm^{-2}$) and a high Q factor (≈430).[288] Copyright 2015, John Wiley and Sons.

(C) An optically pumped single-crystal $MAPbI_3$ nanowire-based laser, showing a super-low threshold ($220\ nJ \cdot cm^{-2}$) and super-high Q factor (≈3600).[199] Scale bars, 10 μm. Copyright 2015, Springer Nature.

(D) An optically pumped single-crystal $CsPbBr_3$ nanowire-based laser, with continuous excitation and emission demonstrated for the first time, which is considered to be due to the excellent thermal stability of all-inorganic perovskites.[289] Scale bars, 2 μm. Copyright 2016, National Academy of Sciences.

(E) Triplet management by modifying the components of 2D halide perovskites. The triplet energy cannot be transferred from P2F8 (PEABr-based perovskite, top) to PEA, but can be transferred from N2F8 (NMABr-based perovskite, bottom) to PEA. The long-lived triplet excitons in the perovskite layer can impede the population inversion during amplified spontaneous emission.[242] Copyright 2020, Springer Nature.

Figure 13. *Continued*

(F) Optically pumped lasing based on N2F8 quasi-2D halide perovskite can be stable for 3,000 h in the air at room temperature by triplet management. The oxygen-sensitive triplet excitons in P2F8 cannot be passivated under an inert N_2 atmosphere, which can transform into long-lived singlet–triplet excitons and reduce the number of photons.[242] Copyright 2020, Springer Nature.

LED's efficiency. With a similar device configuration (ITO/$MAPbBr_3$/ITO),[273] the LED at 2 V showed a green luminescence with narrow full width at half maximum of ~20 nm, indicating intrinsic high color purity in single-crystal LED devices (Figure 12D). The emission at the crystal edges blinked at a subsecond time interval, possibly due to the low electrical injection caused by the sub-band-gap states and the non-radiative carrier traps. Therefore, incorporating functional charge-transport layers is necessary for passivating the sub-band-gap shallow traps, lowering the interfacial barriers, and providing better charge-injection efficiency. Additionally, 2D layered Pb-free $(CH_3NH_3)_2MnCl_4$ single-crystal LEDs, with a similar device structure where the two electrodes directly contacted the halide perovskite, were demonstrated to exhibit red-light luminescence with a quantum efficiency of 2.4% (Figure 12E).[274] The lack of functional carrier-transport layers prevents further improvement of the device performance.

A lithography-based microfabrication process was invented to integrate functional carrier-transport layers in single-crystal halide perovskite LEDs.[82] The process used halide perovskite bulk crystal as the substrate to homoepitaxially grow the microscale single-crystal arrays. Similar to the solution-based epitaxial growth method using a parylene-C protecting layer as discussed above, the different layers of functional materials (e.g., carrier-transport layers and electrodes) were coated and patterned using standard microfabrication, after which the parylene-C was selectively etched. Washing in unsaturated growth solution removed any debris of the halide perovskite from overetching of the parylene-C. The exposed fresh surface of single-crystal halide perovskites was used to homoepitaxially grow the single-crystal microcrystal array with designed geometry, orientation, and size on top of the patterned functional layers. After depositing a top electrode on the microcrystal array, a micro-LED array was demonstrated with an ITO/$MAPbBr_3$/PEDOT:PSS/Au structure and a relatively high external quantum efficiency of 7.1% (Figure 12F). This approach can potentially be applied to other materials in the halide perovskite family to fabricate patterned single-crystal LEDs with diverse emission characteristics.

Lasers

Hybrid halide perovskites exhibit high optical gain as a result of low defect densities,[284] slow Auger recombination rate, high absorption coefficient, long carrier diffusion length, and high photoluminescence quantum yield,[194,199,284–287] which are all advantageous for lasing applications. An optically pumped laser based on single-crystal nanoplates of $MAPbI_3$ was firstly demonstrated (Figure 13A).[194] Emissions at ~780 nm were observed with a high-quality (Q) factor ($\approx$650) and a low threshold (37 $\mu J \cdot cm^{-2}$). The overall results indicated that these high-quality single-crystal nanoplates were strong candidates for lasers. Later, single-crystal square microdisks of $MAPbBr_3$ were prepared for optically pumped lasing (Figure 13B).[288] The microdisk (2.0 $\mu m \times 2.0 \mu m \times 0.6 \mu m$) contained a built-in microresonator of the whispering gallery mode and showed lasing emissions at 557.5 nm with a high Q factor ($\approx$430) at a low threshold of $3.6 \pm 0.5 \mu J \cdot cm^{-2}$. Single-crystal halide perovskite nanowire-based optically pumped laser was also reported (Figure 13C).[199] The super-low threshold (220 $nJ \cdot cm^{-2}$) and super-high Q factor ($\approx$3,600) strongly indicated that the solution-processed perovskite nanowires were very promising candidates for the development of electrically pumped light sources.

Other than these, many micro-/nanostructured single-crystal halide perovskites of different morphologies were used for optically pumped lasing.[199,285–287] Even though researchers have realized different Q factors and low threshold values, there are still no clear clues as to whether morphologies of the crystals are related to the lasing quality. Additionally, more systematic studies on the design and fabrication of the cavity with precise control of the crystal quality/size/morphology are needed to improve the laser performance.

All of these lasing actions can only be realized under pulsed excitations. Continuous excitation and emission are still challenging because continuous excitation and emission may cause heat-induced degradation of the halide perovskite materials. To overcome this challenge, all-inorganic halide perovskite $CsPbBr_3$ nanowires were exploited to build the continuously optically pumped laser (Figure 13D).[289] Because of the excellent stability of the $CsPbBr_3$, lasing actions with a low threshold of 5 $\mu J \cdot cm^{-2}$ and a high Q factor of 1,009 were achieved under continuous excitation for 1 h at room temperature, which represents a major advance toward practical applications.

Even though continuous lasing has been demonstrated, its mechanism remains largely unclear. Recently, the mechanism of continuous lasing in halide perovskites was investigated (Figure 13E).[242] The abrupt termination of lasing under optical pumping was attributed to the long-lived triplet excitons in the perovskite layer, which considerably impeded the population inversion during amplified spontaneous emission. By applying triplet management strategies to modify the perovskite components, optically pumped stable lasing in the air at room temperature based on quasi-2D halide perovskites was realized without obvious performance degradation (Figure 13F). These results may pave the way for realizing electrically pumped lasers in the future.

Field-effect transistors

Due to the superb carrier-transport properties, single-crystal halide perovskites are excellent candidates for FETs. The presence of grain boundaries, interfacial contamination, and abundant point defects in polycrystalline halide perovskites can severely hinder field-effect carrier mobility and device operation. FETs based on polycrystalline halide perovskites show electron mobilities typically from 0.5 to 2 $cm^2 \cdot V^{-1} \cdot s^{-1}$.[192,290–294] This modest performance has been linked to significant lateral tunnel junctions,[122] i.e., the barrier between the source and drain the carriers have to pass. Additionally, the near-surface composition, structure, morphology, and electronic properties of the FET will be affected by the incomplete precursor conversion (e.g., partly converted PbI_2, MAI, and Pb cluster by-products that are not semiconductors)[295,296] and the hydration issue of the perovskite crystal interfaces and grain boundaries,[122] which can further exacerbate such problems.

Single-crystal halide perovskites can potentially improve the FET performance. To date, there are only a few reports on using single-crystal halide perovskites to fabricate FETs.[122,297] An improvement in performance has been obtained using single-crystal halide perovskites at room temperature, with field-effect mobilities up to 4.7 and 1.5 $cm^2 \cdot V^{-1} \cdot s^{-1}$ in the N and P channels, respectively. Those problems induced by defects and impurities in polycrystals were significantly minimized in single crystals, which thus lead to improved field-effect mobilities.

Artificial synapses

Inspired by the powerful signal-processing capabilities of the human brain,[298] research related to neuromorphic computing for the implementation of learning and memory behaviors has received growing attention recently.[299,300]

Although much effort has been spent on the structure and function of the brain at the molecular level, the conventional computing systems based on silicon complementary metal-oxide-semiconductor transistors and von Neumann architectures have two insurmountable challenges: (1) the end of Moore's law restricting the feature size of the chip; (2) physical separation of the memory and the central processing units, known as the "von Neumann bottleneck," causing high costs in energy and speed.[301,302] Driven by the requirements of artificial intelligence in the era of big data, it is urgent to discover new computational devices with small device sizes, low energy consumption, and high computation speed.

Recently, single-crystal halide perovskites have been exploited as the active layer in artificial synapses for realizing neuromorphic computing and bioinspired intelligent systems.[303] For human synapses, the most significant factor is plasticity, the changes in synaptic weight, which is responsible for learning and memorization.[304] The synaptic weight is updated by using functional macromolecules such as proteins.[305] For artificial synapses, the synaptic weight can be updated by changing the device conductivity. In a nutshell, the realization of synaptic functions requires a device with a flexible regulation of conductance and appropriate retention. In other words, hysteresis properties (e.g., electrical or optical) are necessary for the basic functions of artificial synapses.

Halide perovskites suffer from unavoidable hysteresis issues. In this case, these properties can be pivoted to provide tunable charge-trapping capabilities, resulting in flexible regulation of charge conductance and retention. Additionally, halide perovskites have low ion-migration activation energies, which are ideal for building low-energy-consumption artificial synapses. Also, 2D halide perovskites can leverage molecular electronics through self-assembly and potentially shrink the size of artificial synapses.

Two-terminal lateral-structured artificial synapses based on $MAPbBr_3$ single-crystal platelets have been fabricated with an ultralow operating current (down to sub-picoamperes) (Figure 14A).[303] The mechanism of this artificial synapse is based on ion migration and interfacial charge trapping. When low-frequency or small-amplitude pulses are applied to the electrodes, ions in $MAPbBr_3$ will redistribute, which makes the conductance change sharp and short. However, high-frequency or high-amplitude pulses allow ions to have sufficient driving forces to move and to be trapped so that vacancies at their initial sites will form a stable conductive path causing the long-term enhancement of the conductance, which is slow and difficult to switch and thus inappropriate for artificial synapses.

Based on such a structure, essential excitatory postsynaptic current (EPSC) behaviors have been realized, including presynaptic-spike-dependent EPSC and spike-frequency-dependent EPSC (Figure 14B). These results provide a new protocol for designing lateral-structure synaptic devices and future neuromorphic bioelectronics using single-crystal halide perovskites. With the new capability of integrating different layers of functional materials with single-crystal halide perovskites in a vertical structure,[11,82] the charge transport is expected to be even faster, leading to a higher computing speed of the artificial synapses. However, the simple

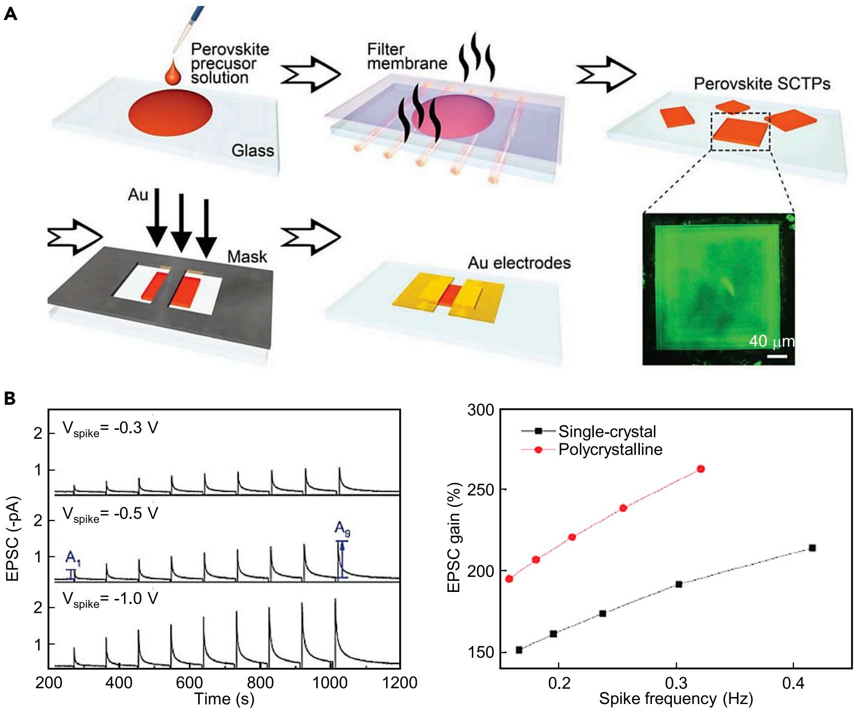

Figure 14. Single-crystal halide perovskite artificial synapses

(A) Schematic fabrication procedures and a fluorescent optical image of the single-crystal $MAPbBr_3$ synaptic device.[303] Copyright 2020, John Wiley and Sons.

(B) The presynaptic spike-dependent EPSC (left) and the spike frequency-dependent EPSC (right). Spikes with large amplitudes or high frequency can enhance the ion migration by suppressing the back-diffusion of ions, which increases the EPSC gain. Especially, the higher gain in the polycrystalline devices suggests more ions are migrating, but the grain boundaries in polycrystalline devices will trap the mobile ions and reduce the gain. The final performance will be a tradeoff. These results illustrate the basic functionality of the artificial synapse.[303] Copyright 2020, John Wiley and Sons.

demonstration of synaptic plasticity on a single device so far cannot meet the requirements for implementing a neuromorphic network, which poses difficulties for defining clearly the logical functions and energy consumptions. Fabrication strategies for integrating arrayed artificial synapses are needed for advanced artificial synapse applications. Also, considering the limited understanding of the biological neuronal network per se, a better interpretation of its computational mechanism is needed to guide the development of next-generation artificial synapses.

FUTURE OPPORTUNITIES

Halide perovskites with an array of alluring merits hold significant implications for various electronic and optoelectronic applications. Single-crystal halide perovskites are particularly desirable owing to their suppressed point defects, lack of grain boundaries, and superior thermal and structural stabilities.[306] However, there are still several grand challenges that need to be overcome to drive the research and development of single-crystal halide perovskites to the next stage, as discussed in the following.

1. Growth methods of single-crystal halide perovskite thin films play a paramount role in determining their optoelectronic properties and final device performance. Effective optimizations of existing strategies and further

exploration of new strategies are needed for more efficient growth to control crystal quality, time efficiency, and yield of single-crystal halide perovskite thin films. Especially for 2D perovskites, there is a lack of effective ways to grow large-sized single crystals.

2. To date, most studies of single-crystal halide perovskite thin films have mainly focused on hybrid halide perovskites (e.g., $MAPbBr_3$ and $MAPbI_3$). Given the instability of the volatile organic components, candidates for stable all-inorganic compositions and associated effective growth and fabrication methods are still needed. Besides, strategies for component engineering should be further developed to design the band structure of single-crystal halide perovskites for different applications.
3. High-performance halide perovskites typically contain Pb, which poses serious environmental and health threats. Therefore, Pb-free perovskites are critically required for large-scale manufacturing and deployment of such functional devices. However, current Pb-free perovskites such as Sn-based, Ge-based, and double perovskites are facing either low-performance or instability problems due to rapid self-doping and intrinsically moderate optoelectronic properties.[307,308] To solve these problems, few solutions have been reported besides doping different chemicals,[309,310] suggesting that more innovative candidates of Pb-free perovskites are called for.
4. The surface quality of single crystals is central for high device performance. Despite very low trap densities in the bulk phase, hybrid single-crystal halide perovskites grown in solution still possess a large number of surface charge traps, which are probably generated from the loss of the organic amine ions.[311,312] The resultant substantial surface recombination may nullify the intrinsic superiority of the single crystals, leading to compromised performance of the overall devices.[232,313–315] Therefore, besides carefully improving the crystal quality in bulk, developing rational techniques for surface passivation would determine the fate of single-crystal devices regarding whether they will eventually be able to rival their polycrystalline counterparts. From the authors' unpublished results, the surface state of single crystals is very different from those in polycrystalline films, which makes existing passivation methods that have been optimized for polycrystals inapplicable to single-crystal devices. Existing passivation methods would not improve, or sometimes even worsen, the performance of single-crystal devices.

Seemingly daunting, these grand challenges can still be tackled. Borrowing ideas from polycrystalline thin films, precursor engineering (e.g., modifying the solvents and compositions) may further improve the quality of the single-crystal halide perovskites during growth. Additionally, considering the structure/component similarity in the halide perovskite family, strained/alloyed epitaxial growth processes among all-inorganic and 2D halide perovskites are promising for addressing the issues of instability and electrical properties, which may bring the performance of single-crystal halide perovskite devices closer to their theoretical predictions. In this way, identifying a master perovskite as a ''perovskite wafer'' may realize an ''epitaxial printing procedure'' of single-crystals, where the substrate can easily control the crystallization of the printed layer with designed patterns. This epitaxial printing procedure may open up new avenues for large-scale halide perovskite-based electronics. All in all, given the already rapid developments in polycrystals and the huge potential of single crystals, future studies of single-crystal halide perovskites represent a fertile ground for new breakthroughs and are therefore even more exciting.

ACKNOWLEDGMENTS

We thank all of the researchers whose results are reviewed here. We also acknowledge the support of a Lattimer Faculty Research Fellowship from the University of California, San Diego and a Sloan Research Fellowship from the Alfred P. Sloan Foundation.

AUTHOR CONTRIBUTIONS

Conceptualization, Y.L., Y.C., and S.X.; Writing – initial draft, Y.L. and Y.C.; Writing – review & editing, S.X.; Copyright, Y.L. and Y.C.; Supervision, S.X.

DECLARATION OF INTERESTS

The authors declare no competing interests.

REFERENCES

1. Chen, Y., He, M., Peng, J., Sun, Y., and Liang, Z. (2016). Structure and growth control of organic-inorganic halide perovskites for optoelectronics: from polycrystalline films to single crystals. Adv. Sci. *3*, 1500392.
2. Park, N.G., and Zhu, K. (2020). Scalable fabrication and coating methods for perovskite solar cells and solar modules. Nat. Rev. Mater. *5*, 333–350.
3. Ball, J.M., and Petrozza, A. (2016). Defects in perovskite-halides and their effects in solar cells. Nat. Energy *1*, 16149.
4. Shi, D., Adinolfi, V., Comin, R., Yuan, M., Alarousu, E., Buin, A., Chen, Y., Shi, D., Hoogland, S., Rothenberger, A., et al. (2015). Low trap-state density and long carrier diffusion in organolead trihalide perovskite single crystals. Science *347*, 519–522.
5. Chen, L., Tan, Y.-Y., Chen, Z.-X., Wang, T., Hu, S., Nan, Z.-A., Xie, L.-Q., Hui, Y., Huang, J.-X., Zhan, C., et al. (2019). Toward long-term stability: single-crystal alloys of cesium-containing mixed cation and mixed halide perovskite. J. Am. Chem. Soc. *141*, 1665–1671.
6. Kong, W., Wang, S., Li, F., Zhao, C., Xing, J., Zou, Y., Yu, Z., Lin, C.-H., Shan, Y., Lai, Y.H., et al. (2020). Ultrathin perovskite monocrystals boost the solar cell performance. Adv. Energy Mater. *10*, 2000453.
7. Fu, M., Tamarat, P., Trebbia, J.-B., Bodnarchuk, M.I., Kovalenko, M.V., Even, J., and Lounis, B. (2018). Unraveling exciton–phonon coupling in individual FAPbI$_3$ nanocrystals emitting near-infrared single photons. Nat. Commun. *9*, 3318.
8. Ni, Z., Bao, C., Liu, Y., Jiang, Q., Wu, W.-Q., Chen, S., Dia, X., Chen, B., Hartweg, B., Yu, Z., et al. (2020). Resolving spatial and energetic distributions of trap states in metal halide perovskite solar cells. Science *367*, 1352–1358.
9. Kelso, M.V., Mahenderkar, N.K., Chen, Q., Tubbesing, J.Z., and Switzer, J.A. (2019). Spin coating epitaxial films. Science *364*, 166.
10. Shi, E., Yuan, B., Shiring, S.B., Gao, Y., Akriti, C, S., D, X., C, B., H, B., Y, Z., et al. (2020). Two-dimensional halide perovskite lateral epitaxial heterostructures. Nature *580*, 614–620.
11. Lei, Y., Chen, Y., Zhang, R., Li, Y., Yan, Q., Lee, S., Yu, Y., Tsai, H., Choi, W., Wang, K., et al. (2020). A fabrication process for flexible single-crystal perovskite devices. Nature *583*, 790–795.
12. Chen, Y., Lei, Y., Li, Y., Yu, Y., Cai, J., Chui, M.-H., Rao, R., Gu, Y., Wang, C., Choi, W., et al. (2020). Strain engineering and epitaxial stabilization of halide perovskites. Nature *577*, 209–215.
13. Rose, G. (1839). Description of some new minerals from the Urals. Ann. Phys. *124*, 551–573.
14. Boyd, C.C., Cheacharoen, R., Leijtens, T., and McGehee, M.D. (2019). Understanding degradation mechanisms and improving stability of perovskite photovoltaics. Chem. Rev. *119*, 3418–3451.
15. Kour, R., Arya, S., Verma, S., Gupta, J., Banhoria, P., Bharti, V., Datt, R., and Gupta, V. (2019). Potential substitutes for replacement of lead in perovskite solar cells: a review. Glob. Chall. *3*, 1900050.
16. Saliba, M., Matsui, T., Domanski, K., Seo, J.-Y., Ummadisingu, A., Zakeeruddin, S.M., Correa-Baena, J.-P., Tress, W.R., Abate, A., Hagfeldt, A., and Grätzel, M. (2016). Incorporation of rubidium cations into perovskite solar cells improves photovoltaic performance. Science *354*, 206–209.
17. Abdi-Jalebi, M., Andaji-Garmaroudi, Z., Cacovich, S., Stavrakas, C., Philippe, B., Richter, J.M., Alsari, M., Booker, E.P., Hutter, E.M., Pearson, A.J., et al. (2018). Maximizing and stabilizing luminescence from halide perovskites with potassium passivation. Nature *555*, 497–501.
18. Xiao, K., Lin, R., Han, Q., Hou, Y., Qin, Z., Nguyen, H.T., Wen, J., Wei, M., Yeddu, V., Saidaminov, M.I., et al. (2020). All-perovskite tandem solar cells with 24.2% certified efficiency and area over 1 cm^2 using surface-anchoring zwitterionic antioxidant. Nat. Energy *5*, 870–880.
19. Lu, H., Liu, Y., Ahlawat, P., Mishra, A., Tress, W.R., Eickemeyer, F.T., Yang, Y., Fu, F., Wang, Z., Avalos, C.E., et al. (2020). Vapor-assisted deposition of highly efficient, stable black-phase FAPbI$_3$ perovskite solar cells. Science *370*, eabb8985.
20. Ke, W., Spanopoulos, I., Stoumpos, C.C., and Kanatzidis, M.G. (2018). Myths and reality of HPbI$_3$ in halide perovskite solar cells. Nat. Commun. *9*, 4785.
21. Chu, Z., Zhao, Y., Ma, F., Zhang, C.-X., Deng, H., Gao, F., Ye, Q., Meng, J., Yin, Z., Zhang, X., and You, J. (2020). Large cation ethylammonium incorporated perovskite for efficient and spectra stable blue light-emitting diodes. Nat. Commun. *11*, 4165.
22. Jodlowski, A.D., Roldán-Carmona, C., Grancini, G., Salado, M., Ralaiarisoa, M., Ahmad, S., Koch, N., Camacho, L., de Miguel, G., and Nazeeruddin, M.K. (2017). Large guanidinium cation mixed with methylammonium in lead iodide perovskites for 19% efficient solar cells. Nat. Energy *2*, 972.
23. Huang, C., Lin, P., Fu, N., Liu, C., Xu, B., Sun, K., Wang, D., Zeng, X., and Ke, S. (2019). Facile fabrication of highly efficient ETL-free perovskite solar cells with 20% efficiency by defect passivation and interface engineering. Chem. Commun. *55*, 2777–2780.
24. Poli, I., Eslava, S., and Cameron, P. (2017). Tetrabutylammonium cations for moisture-resistant and semitransparent perovskite solar cells. J. Mater. Chem. A *5*, 22325–22333.
25. Zhang, Y., Liu, Y., Xu, Z., Ye, H., Li, Q., Hu, M., Yang, Z., and Liu, S.F. (2019). Two-dimensional (PEA)$_2$PbBr$_4$ perovskite single crystals for a high performance UV-detector. J. Mater. Chem. C *7*, 1584–1591.
26. Li, N., Zhu, Z., Chueh, C.-C., Liu, H., Peng, B., Petrone, A., Li, X., Wang, L., and Jen, A.K.-Y. (2017). Mixed cation FA$_x$PEA$_{1-x}$PbI$_3$ with enhanced phase and ambient stability toward high-performance perovskite solar cells. Adv. Energy Mater. *7*, 1601307.
27. Kim, G., Min, H., Lee, K.S., Lee, D.Y., Yoon, S.M., and Seok, S.I. (2020). Impact of strain relaxation on performance of α-formamidinium lead iodide perovskite solar cells. Science *370*, 108–112.
28. Yang, F., Kamarudin, M.A., Kapil, G., Hirotani, D., Zhang, P., Ng, C.H., Ma, T., and Hayase, S. (2018). Magnesium-doped MAPbI3 perovskite layers for enhanced photovoltaic performance in humid air atmosphere. ACS Appl. Mater. Interfaces *10*, 24543–24548.

29. Chan, S.-H., Wu, M.-C., Lee, K.-M., Chen, W.-C., Lin, T.-H., and Su, W.-F. (2017). Enhancing perovskite solar cell performance and stability by doping barium in methylammonium lead halide. J. Mater. Chem. A *5*, 18044–18052.

30. Liu, W., Chu, L., Liu, N., Ma, Y., Hu, R., Weng, Y., Li, H., Zhang, J., Li, X., and Huang, W. (2019). Efficient perovskite solar cells fabricated by manganese cations incorporated in hybrid perovskites. J. Mater. Chem. C *7*, 11943–11952.

31. Boström, H.L.B., Bruckmoser, J., and Goodwin, A.L. (2019). Ordered B-site vacancies in an ABX_3 formate perovskite. J. Am. Chem. Soc. *141*, 17978–17982.

32. Islam, M.N., Hadi, M.A., and Podder, J. (2019). Influence of Ni doping in a lead-halide and a lead-free halide perovskites for optoelectronic applications. AIP Adv. *9*, 125321.

33. Wang, K.-L., Wang, R., Wang, Z.-K., Li, M., Zhang, Y., Ma, H., Liao, L.-S., and Yang, Y. (2019). Tailored phase transformation of $CsPbI_2Br$ films by copper(II) bromide for high-performance all-inorganic perovskite solar cells. Nano Lett. *19*, 5176–5184.

34. Thapa, S., Adhikari, G.C., Zhu, H., Grigoriev, A., and Zhu, P. (2019). Zn-alloyed all-inorganic halide perovskite-based white light-emitting diodes with superior color quality. Sci. Rep. *9*, 18636.

35. Cai, T., Yang, H., Hills-Kimball, K., Song, J.-P., Zhu, H., Hofman, E., Zheng, W., Rubenstein, B.M., and Chen, O. (2018). Synthesis of all-inorganic Cd-doped $CsPbCl_3$ perovskite nanocrystals with dual-wavelength emission. J. Phys. Chem. Lett. *9*, 7079–7084.

36. Kopacic, I., Friesenbichler, B., Höfler, S.F., Kunert, B., Plank, H., Rath, T., and Trimmel, G. (2018). Enhanced performance of germanium halide perovskite solar cells through compositional engineering. ACS Appl. Energy Mater. *1*, 343–347.

37. Lee, S.J., Shin, S.S., Im, J., Ahn, T.K., Noh, J.H., Jeon, N.J., Seok, S.I., and Seo, J. (2017). Reducing carrier density in formamidinium tin perovskites and its beneficial effects on stability and efficiency of perovskite solar cells. ACS Energy Lett. *3*, 46–53.

38. Xiang, W., Wang, Z., Kubicki, D.J., Tress, W., Luo, J., Prochowicz, D., Akin, S., Emsley, L., Zhao, J., Dietler, G., et al. (2019). Europium-doped $CsPbI_2Br$ for stable and highly efficient inorganic perovskite solar cells. Joule *3*, 205–214.

39. Arumugam, G.M., Xu, C., Karunakaran, S.K., Shi, Z., Qin, F., Zhu, C., and Chen, F. (2018). Low threshold lasing from novel thulium-incorporated $C(NH_2)_3PbI_3$ perovskite thin films in Fabry-Pérot resonator. J. Mater. Chem. C *6*, 12537–12546.

40. Zhou, D., Liu, D., Pan, G., Chen, X., Li, D., Xu, W., Bai, X., and Song, H. (2017). Cerium and ytterbium codoped halide perovskite quantum dots: a novel and efficient downconverter for improving the performance of silicon solar cells. Adv. Mater. *29*, 1704149.

41. Liu, Y., Yang, Z., Cui, D., Ren, X., Sun, J., Liu, X., Zhang, J., Wei, Q., Fan, H., Yu, F., et al. (2015). Two-inch-sized perovskite $CH_3NH_3PbX_3$ (X= Cl, Br, I) crystals: growth and characterization. Adv. Mater. *27*, 5176–5183.

42. Fang, Y., Wei, H., Dong, Q., and Huang, J. (2017). Quantification of re-absorption and re-emission processes to determine photon recycling efficiency in perovskite single crystals. Nat. Commun. *8*, 14417.

43. Li, X., Zhang, F., He, H., Berry, J.J., Zhu, K., and Xu, T. (2020). On-device lead sequestration for perovskite solar cells. Nature *578*, 555–558.

44. Donlan, E.A., Boström, H.L.B., Geddes, H.S., Reynolds, E.M., and Goodwin, A.L. (2017). Compositional nanodomain formation in hybrid formate perovskites. Chem. Commun. *53*, 11233–11236.

45. Lang, C., Jia, Y., Liu, J., Wang, H., Ouyang, L., Zhu, M., and Yao, X. (2018). Dehydrogenation and reaction pathway of perovskite-type $NH_4Ca(BH_4)_3$. Prog. Nat. Sci. Mater. Int. *28*, 194–199.

46. Murali, B., Kolli, H.K., Yin, J., Ketavath, R., Bakr, O.M., and Mohammed, O.F. (2020). Single crystals: the next big wave of perovskite optoelectronics. ACS Mater. Lett. *2*, 184–214.

47. Stranks, S.D., and Snaith, H.J. (2015). Metal-halide perovskites for photovoltaic and light-emitting devices. Nat. Nanotechnol. *10*, 391–402.

48. Li, Z., Yang, M., Park, J.-S., Wei, S.-H., Berry, J.J., and Zhu, K. (2015). Stabilizing perovskite structures by tuning tolerance factor: formation of formamidinium and cesium lead iodide solid-state alloys. Chem. Mater. *28*, 284–292.

49. Blancon, J.-C., Even, J., Stoumpos, C.C., Kanatzidis, M.G., and Mohite, A.D. (2020). Semiconductor physics of organic–inorganic 2D halide perovskites. Nat. Nanotechnol. *15*, 969–985.

50. Jang, D.M., Park, K., Kim, D.H., Park, J., Shojaei, F., Kang, H.S., Ahn, J.-P., Lee, J.W., and Song, J.K. (2015). Reversible halide exchange reaction of organometal trihalide perovskite colloidal nanocrystals for full-range band gap tuning. Nano Lett. *15*, 5191–5199.

51. Dunlap-Shohl, W.A., Zhou, Y., Padture, N.P., and Mitzi, D.B. (2019). Synthetic approaches for halide perovskite thin films. Chem. Rev. *119*, 3193–3295.

52. Zheng, K., Abdellah, M., Zhu, Q., Kong, Q., Jennings, G., Kurtz, C.A., Messing, M.E., Niu, Y., Gosztola, D.J., Al-Marri, M.J., et al. (2016). Direct experimental evidence for photoinduced strong-coupling polarons in organolead halide perovskite nanoparticles. J. Phys. Chem. Lett. *7*, 4535–4539.

53. El-Mellouhi, F., Marzouk, A., Bentria, E.T., Rashkeev, S.N., Kais, S., and Alharbi, F.H. (2016). Hydrogen bonding and stability of hybrid organic-inorganic perovskites. ChemSusChem *9*, 2648–2655.

54. Zhang, W., Eperon, G.E., and Snaith, H.J. (2016). Metal halide perovskites for energy applications. Nat. Energy *1*, 16048.

55. Mehmood, U., Al-Ahmed, A., Afzaal, M., Al-Sulaiman, F.A., and Daud, M. (2017). Recent progress and remaining challenges in organometallic halides based perovskite solar cells. Renew. Sustain. Energy Rev. *78*, 1–14.

56. Zou, C., Chang, C., Sun, D., Böhringer, K.F., and Lin, L.Y. (2020). Photolithographic patterning of perovskite thin films for multicolor display applications. Nano Lett. *20*, 3710–3717.

57. Lu, M., Zhang, Y., Wang, S., Guo, J., Yu, W.W., and Rogach, A.L. (2019). Metal halide perovskite light-emitting devices: promising technology for next-generation displays. Adv. Funct. Mater. *29*, 1902008.

58. Sun, W., Liu, Y., Qu, G., Fan, Y., Dai, W., Wang, Y., Song, Q., Han, J., and Xiao, S. (2020). Lead halide perovskite vortex microlasers. Nat. Commun. *11*, 4862.

59. Wang, K., Xing, G., Song, Q., and Xiao, S. (2020). Micro- and nanostructured lead halide perovskites: from materials to integrations and devices. Adv. Mater. *33*, 2000306.

60. Li, J., Han, Z., Gu, Y., Yu, D., Liu, J., Hu, D., Xu, X., and Zeng, H. (2020). Perovskite single crystals: synthesis, optoelectronic properties, and application. Adv. Funct. Mater. *33*, 2008684.

61. Yang, Z., Surrente, A., Galkowski, K., Bruyant, N., Maude, D.K., Haghighirad, A.A., Snaith, H.J., Plochocka, P., and Nicholas, R.J. (2017). Unraveling the exciton binding energy and the dielectric constant in single-crystal methylammonium lead triiodide perovskite. J. Phys. Chem. Lett. *8*, 1851–1855.

62. Herz, L.M. (2016). Charge-carrier dynamics in organic-inorganic metal halide perovskites. Annu. Rev. Phys. Chem. *67*, 65–89.

63. Zhang, F., Lu, H., Tong, J., Berry, J.J., Beard, M.C., and Zhu, K. (2020). Advances in two-dimensional organic-inorganic hybrid perovskites. Energy Environ. Sci. *13*, 1154–1186.

64. Wang, K., Wang, S., Xiao, S., and Song, Q. (2018). Recent advances in perovskite micro- and nanolasers. Adv. Opt. Mater. *6*, 1800278.

65. Herz, L.M. (2017). Charge-carrier mobilities in metal halide perovskites: fundamental mechanisms and limits. ACS Energy Lett. *2*, 1539–1548.

66. Kim, J., Lee, S.-H., Lee, J.H., and Hong, K.-H. (2014). The role of intrinsic defects in methylammonium lead iodide perovskite. J. Phys. Chem. Lett. *5*, 1312–1317.

67. Brenner, T.M., Egger, D.A., Rappe, A.M., Kronik, L., Hodes, G., and Cahen, D. (2015). Are mobilities in hybrid organic-inorganic halide perovskites actually "high"? J. Phys. Chem. Lett. *6*, 4754–4757.

68. Dubey, S., Paliwal, A., and Ghosh, S. (2016). Frohlich interaction in compound semiconductors: a comparative study. Adv. Mater. Res. *1141*, 44–50.

69. Ahmadi, M., Wu, T., and Hu, B. (2017). A review on organic-inorganic halide perovskite photodetectors: device engineering and

fundamental physics. Adv. Mater. *41*. https://doi.org/10.1002/adma.201605242.

70. Wehrenfennig, C., Liu, M., Snaith, H.J., Johnston, M.B., and Herz, L.M. (2014). Homogeneous emission line broadening in the organo lead halide perovskite $CH_3NH_3PbI_{3-x}Cl_x$. J. Phys. Chem. Lett. *5*, 1300–1306.

71. De Wolf, S., Holovsky, J., Moon, S.-J., Löper, P., Niesen, B., Ledinsky, M., Haug, F.-J., Yum, J.-H., and Ballif, C. (2014). Organometallic halide perovskites: sharp optical absorption edge and its relation to photovoltaic performance. J. Phys. Chem. Lett. *5*, 1035–1039.

72. Huang, J., Yuan, Y., Shao, Y., and Yan, Y. (2017). Understanding the physical properties of hybrid perovskites for photovoltaic applications. Nat. Rev. Mater. *2*, 17042.

73. Yang, Z., Deng, Y., Zhang, X., Wang, S., Chen, H., Yang, S., Khurgin, J., Fang, N.X., Zhang, X., and Ma, R. (2018). High-performance single-crystalline perovskite thin-film photodetector. Adv. Mater. *30*, 1704333.

74. Krogstrup, P., Jørgensen, H.I., Heiss, M., Demichel, O., Holm, J.V., Aagesen, M., Nygard, J., and Fontcuberta i Morral, A. (2013). Single-nanowire solar cells beyond the Shockley-Queisser limit. Nat. Photon. *7*, 306–310.

75. Petrus, M.L., Schlipf, J., Li, C., Gujar, T.P., Giesbrecht, N., Müller-Buschbaum, P., Thelakkat, M., Bein, T., Hüttner, S., and Docampo, P. (2017). Capturing the sun: a review of the challenges and perspectives of perovskite solar cells. Adv. Energy Mater. *7*, 1700264.

76. García de Arquer, F.P., Armin, A., Meredith, P., and Sargent, E.H. (2017). Solution-processed semiconductors for next-generation photodetectors. Nat. Rev. Mater. *2*, 16100.

77. Voznyy, O., Sutherland, B.R., Ip, A.H., Zhitomirsky, D., and Sargent, E.H. (2017). Engineering charge transport by heterostructuring solution-processed semiconductors. Nat. Rev. Mater. *2*, 17026.

78. Luo, D., Su, R., Zhang, W., Gong, Q., and Zhu, R. (2019). Minimizing non-radiative recombination losses in perovskite solar cells. Nat. Rev. Mater. *5*, 44–60.

79. Dong, Q., Fang, Y., Shao, Y., Mulligan, P., Qiu, J., Cao, L., and Huang, J. (2015). Solar cells. Electron-hole diffusion lengths >175 μm in solution-grown $CH_3NH_3PbI_3$ single crystals. Science *347*, 967–970.

80. Liu, Y., Ye, H., Zhang, Y., Zhao, K., Yang, Z., Yuan, Y., Wu, H., Zhao, G., Yang, Z., Tang, J., et al. (2019). Surface-tension-controlled crystallization for high-quality 2D perovskite single crystals for ultrahigh photodetection. Matter *1*, 465–480.

81. Ebadi, F., Taghavinia, N., Mohammadpour, R., Hagfeldt, A., and Tress, W. (2019). Origin of apparent light-enhanced and negative capacitance in perovskite solar cells. Nat. Commun. *10*, 1574.

82. Lei, Y., Chen, Y., Gu, Y., Wang, C., Huang, Z., QIan, H., Nie, J., Hollett, G., Choi, W., Yu, Y., et al. (2018). Controlled homoepitaxial growth of hybrid perovskites. Adv. Mater. *30*, 1705992.

83. Ma, C., and Park, N.-G. (2020). A realistic methodology for 30% efficient perovskite solar cells. Chem *6*, 1254–1264.

84. Jiang, X., Fu, X., Ju, D., Yang, S., Chen, Z., and Tao, X. (2020). Designing large-area single-crystal perovskite solar cells. ACS Energy Lett. *5*, 1797–1803.

85. Saidaminov, M.I., Abdelhady, A.L., Murali, B., Alarousu, E., Burlakov, V.M., Peng, W., Dursun, I., Wang, L., He, Y., Maculan, G., et al. (2015). High-quality bulk hybrid perovskite single crystals within minutes by inverse temperature crystallization. Nat. Commun. *6*, 7586.

86. Lin, R., Guo, Q., Zhu, Q., Zhu, Y., Zheng, W., and Huang, F. (2019). All-inorganic $CsCu_2I_3$ single crystal with high-PLQY (≈15.7%) intrinsic white-light emission via strongly localized 1D excitonic recombination. Adv. Mater. *31*, 1905079.

87. Ham, S., Choi, Y.J., Lee, J.-W., Park, N.-G., and Kim, D. (2017). Impact of excess CH_3NH_3I on free carrier dynamics in high-performance nonstoichiometric perovskites. J. Phys. Chem. C *121*, 3143–3148.

88. Brenes, R., Eames, C., Bulovic, V., Islam, M.S., and Stranks, S.D. (2018). The impact of atmosphere on the local luminescence properties of metal halide perovskite grains. Adv. Mater. *30*, e1706208.

89. Zheng, X., Hou, Y., Bao, C., Yin, J., Yuan, F., Huang, Z., Song, K., Liu, J., Troughton, J., Gasparini, N., et al. (2020). Managing grains and interfaces via ligand anchoring enables 22.3%-efficiency inverted perovskite solar cells. Nat. Energy *5*, 131–140.

90. Haque, M.A., Troughton, J., and Baran, D. (2020). Processing-performance evolution of perovskite solar cells: from large grain polycrystalline films to single crystals. Adv. Energy Mater. *10*, 1902762.

91. Song, J., Zhou, Y., Padture, N.P., and Huey, B.D. (2020). Anomalous 3D nanoscale photoconduction in hybrid perovskite semiconductors revealed by tomographic atomic force microscopy. Nat. Commun. *11*, 3308.

92. Szostak, R., Silva, J.C., Turren-Cruz, S.-H., Moares, M.M., Freitas, R.O., Hagfeldt, A., Tolentino, H.C.N., and Nogueira, A.F. (2019). Nanoscale mapping of chemical composition in organic-inorganic hybrid perovskite films. Sci. Adv. *5*, eaaw6619.

93. Visoly-Fisher, I., Cohen, S.R., Gartsman, K., Ruzin, A., and Cahen, D. (2006). Understanding the beneficial role of grain boundaries in polycrystalline solar cells from single-grain-boundary scanning probe microscopy. Adv. Funct. Mater. *16*, 649–660.

94. Li, J.B., Chawla, V., and Clemens, B.M. (2012). Investigating the role of grain boundaries in CZTS and CZTSSe thin film solar cells with scanning probe microscopy. Adv. Mater. *24*, 720–723.

95. Sherkar, T.S., Momblona, C., Gil-Escrig, L., Ávila, J., Sessolo, M., Bolink, H.J., and Koster, L.J.A. (2017). Recombination in perovskite solar cells: significance of grain boundaries, interface traps, and defect ions. ACS Energy Lett. *2*, 1214–1222.

96. Seeger, K. (2004). Semiconductor Physics (Springer-Verlag).

97. Chu, Z., Yang, M., Schulz, P., Wu, D., Ma, X., Seifert, E., Liuyang, S., Li, X., Zhu, K., and Lai, K. (2017). Impact of grain boundaries on efficiency and stability of organic-inorganic trihalide perovskites. Nat. Commun. *8*, 2230.

98. Wenger, B., Nayak, P.K., Wen, X., Kesava, S.V., Noel, N.K., and Snaith, H.J. (2017). Consolidation of the optoelectronic properties of $CH_3NH_3PbBr_3$ perovskite single crystals. Nat. Commun. *8*, 590.

99. Reid, O.G., Yang, M., Kopidakis, N., Zhu, K., and Rumbles, G. (2016). Grain-size-limited mobility in methylammonium lead iodide perovskite thin films. ACS Energy Lett. *1*, 561–565.

100. Liu, Y., Yang, Z., and Liu, S.F. (2017). Recent progress in single-crystalline perovskite research including crystal preparation, property evaluation, and applications. Adv. Sci. *5*, 1700471.

101. He, Y., Petryk, M., Liu, Z., Chica, D.G., Hadar, I., Leak, C., Ke, W., Spanopoulos, I., Lin, W., Chung, D.Y., et al. (2020). $CsPbBr_3$ perovskite detectors with 1.4% energy resolution for high-energy γ-rays. Nat. Photon. *15*, 36–42.

102. Huang, Y., Li, L., Liu, Z., Jiao, H., He, Y., Wang, X., Zhu, R., Wang, D., Sun, J., Chen, Q., and Zhou, H. (2017). The intrinsic properties of $FA_{(1-x)}MA_xPbI_3$ perovskite single crystals. J. Mater. Chem. A *5*, 8537–8544.

103. Li, H., Song, J., Pan, W., Xu, D., Zhu, W.-A., Wei, H., and Yang, B. (2020). Sensitive and stable 2D perovskite single-crystal X-ray detectors enabled by a supramolecular anchor. Adv. Mater. *32*, 2003790.

104. Zhu, H.L., Liang, Z., Huo, Z., Ng, W.K., Mao, J., Wong, K.S., Y, W.-J., and Choy, W.C.H. (2018). Low-bandgap methylammonium-rubidium cation Sn-rich perovskites for efficient ultraviolet-visible-near infrared photodetectors. Adv. Funct. Mater. *28*, 1706068.

105. Valverde-Chávez, D.A., Ponseca Jr., C.S.,, Stoumpos, C.C., Yartsey, A., Kanatzidis, M.G., Sundström, V., and Cooke, D.G. (2015). Intrinsic femtosecond charge generation dynamics in single crystal $CH_3NH_3PbI_3$. Energy Environ. Sci. *8*, 3700–3707.

106. Ponseca, C.S., Savenije, T.J., Abdellah, M., Zheng, K., Yartsev, A., Pascher, T., Harlang, T., Chabera, P., Pullerits, T., Stepanov, A., et al. (2014). Organometal halide perovskite solar cell materials rationalized: ultrafast charge generation, high and microsecond-long balanced mobilities, and slow recombination. J. Am. Chem. Soc. *136*, 5189–5192.

107. Gong, X., Huang, Z., Sabatini, R., Tan, C.-S., Bappi, G., Walters, G., Proppe, A., Saidaminov, M.I., Voznyy, O., Kelley, S.O., and Sargent, E.H. (2019). Contactless measurements of photocarrier transport properties in perovskite single crystals. Nat. Commun. *10*, 1591.

108. Cheng, X., Yang, S., Cao, B., Tao, X., and Chen, Z. (2020). Single crystal perovskite solar cells: development and perspectives. Adv. Funct. Mater. *30*, 1905021.

109. Bao, C., Xu, W., Yang, J., Bai, S., Teng, P., Yang, Y., Wang, J., Zhao, N., Zhang, W., Huang, W., and Gao, F. (2020). Bidirectional optical signal transmission between two identical devices using perovskite diodes. Nat. Electron. *3*, 156–164.

110. Huang, C., Zhang, C., Xiao, S., Wang, Y., Fan, Y., Liu, Y., Zhang, N., Qu, G., Ji, H., Han, J., et al. (2020). Ultrafast control of vortex microlasers. Science *367*, 1018–1021.

111. Bao, C., Chen, Z., Fang, Y., Wei, H., Deng, Y., Xiao, X., Li, L., and Huang, J. (2017). Low-noise and large-linear-dynamic-range photodetectors based on hybrid-perovskite thin-single-crystals. Adv. Mater. *29*, 1703209.

112. Shao, Y., Fang, Y., Li, T., Wang, Q., Dong, Q., Deng, Y., Yuan, Y., Wei, H., Wang, M., Gruverman, A., et al. (2016). Grain boundary dominated ion migration in polycrystalline organic-inorganic halide perovskite films. Energy Environ. Sci. *9*, 1752–1759.

113. Motti, S.G., Meggiolaro, D., Martani, S., Sorrentino, R., Barker, A.J., De Angelis, F., and Petrozza, A. (2019). Defect activity in lead halide perovskites. Adv. Mater. *0*, 1901183.

114. Hong, K., Le, Q.V., Kim, S.Y., and Jang, H.W. (2018). Low-dimensional halide perovskites: review and issues. J. Mater. Chem. C *6*, 2189–2209.

115. Zhang, Y., Liu, Y., Xu, Z., Yang, Z., and Liu, S. (2020). 2D perovskite single crystals with suppressed ion migration for high-performance planar-type photodetectors. Small *16*, 2003145.

116. Lee, J.-W., Kim, S.-G., Yang, J.-M., Yang, Y., and Park, N.-G. (2019). Verification and mitigation of ion migration in perovskite solar cells. APL Mater. *7*, 041111.

117. Liu, Y., Ievlev, A.V., Borodinov, N., Lorenz, M., Xiao, K., Ahmadi, M., Hu, B., Kalinin, S.V., and Ovchinnikova, O.S. (2020). Direct observation of photoinduced ion migration in lead halide perovskites. Adv. Funct. Mater. *31*, 2008777.

118. Wang, K., Yang, D., Wu, C., Shapter, J., and Priya, S. (2019). Mono-crystalline perovskite photovoltaics toward ultrahigh efficiency? Joule *3*, 311–316.

119. Xing, J., Wang, Q., Dong, Q., Yuan, Y., Fang, Y., and Huang, J. (2016). Ultrafast ion migration in hybrid perovskite polycrystalline thin films under light and suppression in single crystals. Phys. Chem. Chem. Phys. *18*, 30484–30490.

120. Liu, Y., Chen, P.-A., and Hu, Y. (2020). Recent developments in fabrication and performance of metal halide perovskite field-effect transistors. J. Mater. Chem. C *8*, 16691–16715.

121. Wu, T., Pisula, W., Rashid, M.Y.A., and Gao, P. (2019). Application of perovskite-structured materials in field-effect transistors. Adv. Electron. Mater. *5*, 1900444.

122. Yu, W., Li, F., Yu, L., Niazi, M.R., Zou, Y., Corzo, D., Basu, A., Ma, C., Dey, S., Tietze, M.L., et al. (2018). Single crystal hybrid perovskite field-effect transistors. Nat. Commun. *9*, 5354.

123. Liu, F., Wang, L., Wang, J., Wang, F., Chen, Y., Zhang, S., Sun, H., Liu, J., Wang, G., Hu, Y., and Jiang, Chao. (2020). 2D Ruddlesden-Popper perovskite single crystal field-effect transistors. Adv. Funct. Mater. *31*, 2005662.

124. Wang, Q., Chen, B., Liu, Y., Deng, Y., Bai, Y., Dong, Q., and Huang, J. (2017). Scaling behavior of moisture-induced grain degradation in polycrystalline hybrid perovskite thin films. Energy Environ. Sci. *10*, 516–522.

125. Song, Y., Bi, W., Wang, A., Liu, X., Kang, Y., and Dong, Q. (2020). Efficient lateral-structure perovskite single crystal solar cells with high operational stability. Nat. Commun. *11*, 274.

126. Babu, R., Giribabu, L., and Singh, S.P. (2018). Recent advances in halide-based perovskite crystals and their optoelectronic applications. Cryst. Growth Des. *18*, 2645–2664.

127. Dang, Y., Liu, Y., Sun, Y., Yuan, D., Liu, X., Lu, W., Liu, G., Xia, H., and Tao, X. (2015). Bulk crystal growth of hybrid perovskite material $CH_3NH_3PbI_3$. CrystEngComm *17*, 665–670.

128. Yoon, E., Jang, K.Y., Park, J., and Lee, T.-W. (2020). Understanding the synergistic effect of device architecture design toward efficient perovskite light-emitting diodes using interfacial layer engineering. Adv. Mater. Interfaces *8*, 2001712.

129. Xu, W., Hu, Q., Bai, S., Bao, C., Miao, Y., Yuan, Z., Borzda, T., Barker, A.J., Tyukalova, E., Hu, Z., et al. (2019). Rational molecular passivation for high-performance perovskite light-emitting diodes. Nat. Photon. *13*, 418–424.

130. Hong, M., Kwo, J., Kortan, A.R., Mannaerts, J.P., and Sergent, A.M. (1999). Epitaxial cubic Gadolinium oxide as a dielectric for gallium arsenide passivation. Science *283*, 1897–1900.

131. Mårtensson, T., Svensson, C.P.T., Wacaser, B.A., Larsson, M.W., Seifert, W., Deppert, K., Gustafsson, A., Wallenberg, L.R., and Samuelson, L. (2004). Epitaxial III-V nanowires on silicon. Nano Lett. *4*, 1987–1990.

132. Hu, Y., Guo, Y., Wang, Y., Chen, Z., Sun, X., Feng, J., Lu, T.-M., Wertz, E., and Shi, J. (2017). A review on low dimensional metal halides: vapor phase epitaxy and physical properties. J. Mater. Res. *32*, 3992–4024.

133. Wang, L., Chen, P., Thongprong, Non., Young, M., Kuttipillai, P.S., Jiang, C., Zhang, P., Sun, K., Duxbury, P., and Lunt, R.R. (2017). Unlocking the single-domain epitaxy of halide perovskites. Adv. Mater. Interfaces *4*, 1701003.

134. Sun, M., Fang, Q., Zhang, Z., Xie, D., Sun, Y., Xu, J., Li, W., Ren, T., and Zhang, Y. (2018). All-inorganic perovskite nanowires-ingazno heterojunction for high-performance ultraviolet–visible photodetectors. ACS Appl. Mater. Interfaces *10*, 7231–7238.

135. Wang, L., Xu, X., Zhang, L., Qiao, R., Wu, M., Wang, Z., Zhang, S., Liang, J., Zhang, Z., Zhang, Z., et al. (2019). Epitaxial growth of a 100-square-centimetre single-crystal hexagonal boron nitride monolayer on copper. Nature, 91–95.

136. Wang, K., Puretzky, A.A., Hu, Z., Srijanto, B.R., Li, X., Gupta, N., Yu, H., Tian, M., Mahjouri-Samani, M., Gao, X., et al. (2019). Strain tolerance of two-dimensional crystal growth on curved surfaces. Sci. Adv. *5*, eaav4028.

137. Zhang, Z., Chen, P., Duan, X., Zang, K., Luo, J., and Duan, X. (2017). Robust epitaxial growth of two-dimensional heterostructures, multiheterostructures, and superlattices. Science *357*, 788–792.

138. Kuchuk, A.V., Kryvyi, S., Lvtvyn, P.M., Li, S., Kladko, V.P., Ware, M.E., Mazur, Y.I., Safryuk, N.V., Stanchu, H.V., Belyaev, A.E., and Salamo, G.J. (2016). The peculiarities of strain relaxation in GaN/AlN superlattices grown on vicinal GaN (0001) substrate: comparative XRD and AFM study. Nanoscale Res. Lett. *11*, 252.

139. Oksenberg, E., Sanders, E., Popovitz-Biro, R., Houben, L., and Joselevich, E. (2018). Surface-guided $CsPbBr_3$ perovskite nanowires on flat and faceted sapphire with size-dependent photoluminescence and fast photoconductive response. Nano Lett. *18*, 424–433.

140. Chen, J., Luo, Z., Fu, Y., Wang, X., Czech, K.J., Shen, S., Guo, L., Wright, J.C., Pan, A., and Jin, S. (2019). Tin(IV)-Tolerant Vapor-Phase Growth and Photophysical Properties of Aligned Cesium Tin Halide Perovskite ($CsSnX_3$; X = Br, I) Nanowires. ACS Energy Letters 4, 1045–1052. https://doi.org/10.1021/acsenergylett.9b00543.

141. Zhang, Y., Huang, F., and Mi, Q. (2016). Preferential facet growth of methylammonium lead halide single crystals promoted by halide coordination. Chem. Lett. *45*, 1030–1032.

142. Jao, M.-H., Lu, C.-F., Tai, P.-Y., and Su, W.-F. (2017). Precise facet engineering of perovskite single crystals by ligand-mediated strategy. Cryst. Growth Des. *17*, 5945–5952.

143. Kim, D., Yun, J.-H., Lyu, M., Kim, J., Lim, S., Yun, J.S., Wang, L., and Seidel, J. (2019). Probing facet-dependent surface defects in $MAPbI_3$ perovskite single crystals. J. Phys. Chem. C *123*, 14144–14151.

144. Wang, Y. (2018). Nontrivial strength of van der Waals epitaxial interaction in soft perovskites. Phys. Rev. Mater. *2*, 076002.

145. Wang, P., Zhao, J., Wei, L., Zhu, Q., Xie, S., Liu, J., Meng, X., and Li, J. (2017). Photo-induced ferroelectric switching in perovskite $CH_3NH_3PbI_3$ films. Nanoscale *9*, 3806–3817.

146. Xiao, X., Li, W., Fang, Y., Liu, Y., Shao, Y., Yang, S., Zhao, J., Dai, X., Zia, R., and Huang, J. (2020). Benign ferroelastic twin boundaries in halide perovskites for charge carrier transport and recombination. Nat. Commun. *11*, 2215.

147. Huang, B., Kong, G., Esfahani, E.N., Chen, S., Li, Q., Yu, J., Xu, N., Zhang, Y., Xie, S., Wen, H., et al. (2018). Ferroic domains regulate photocurrent in single-crystalline $CH_3NH_3PbI_3$ films self-grown on FTO/TiO_2 substrate. NPJ Quantum Mater. *3*, 30.

148. Qiao, W.-C., Wu, J., Zhang, R., Ou-Yang, W., Chen, X., Yang, G., Chen, Q., Wang, X.L., Wang, H.F., and Yao, Y.F. (2020). In situ NMR investigation of the photoresponse of perovskite crystal. Matter *3*, 2042–2054.

149. Dursun, I., Zheng, Y., Guo, T., De Bastiani, M., Turedi, B., Sinatra, L., Haque, M.D., Sun, B., Zhumekenov, A.A., Saidaminov, M.I., et al. (2018). Efficient photon recycling and radiation trapping in cesium lead halide perovskite waveguides. ACS Energy Lett. 1492–1498.

150. Li, X.Y., Luo, Y.Q., Holt, M.V., Cai, Z.H., and Fenning, D.P. (2019). Residual nanoscale strain in cesium lead bromide perovskite reduces stability and shifts local luminescence. Chem. Mater. *31*, 2778–2785.

151. Bush, K.A., Rolston, N., Gold-Parker, A., Manzoor, S., Hausele, J., Yu, Z.J., Raiford, J.A., Cheacharoen, R., Holman, Z.C., Toney, M.F., et al. (2018). Controlling thin-film stress and wrinkling during perovskite film formation. ACS Energy Lett. *3*, 1225–1232.

152. Zheng, X., Wu, C., Jha, S.K., and Li, Z. (2016). Improved phase stability of formamidinium lead triiodide perovskite by strain relaxation. ACS Energy Lett. *1*, 1014–1020.

153. Wang, Y., Sun, X., Chen, Z., Cai, Z., Zhou, H., Lu, T.-M., and Shi, J. (2018). Defect-engineered epitaxial VO2$\pm\delta$ in strain engineering of heterogeneous soft crystals. Sci. Adv. *4*, eaar3679.

154. Zhang, X. (2020). Strain control for halide perovskites. Matter *2*, 294–296.

155. Liu, M., Chen, Y., Tan, C.-S., Quintero-Bermudez, R., Proppe, A.H., Munir, R., Tan, H., Voznyy, O., Scheffel, B., Walters, G., et al. (2019). Lattice anchoring stabilizes solution-processed semiconductors. Nature *570*, 96–101.

156. Xu, Y., Park, J.-H., Yao, Z., Wolverton, C., Razeghi, M., Wu, J., and Dravid, V.P. (2019). Strain-induced metastable phase stabilization in $\mathrm{Ga_2O_3}$ thin films. ACS Appl. Mater. Interfaces, 5536–5543.

157. Langenberg, E., Guzmán, R., Maurel, L., Martínez de Baños, L., Morellón, L., Ibarra, M.R., Herrero-Martín, J., Blasco, J., Magén, C., Algarabel, P.A., and Pardo, J.A. (2015). Epitaxial stabilization of the perovskite phase in $\mathrm{(Sr_{1\text{-}x}Ba_x)MnO_3}$ thin films. ACS Appl. Mater. Interfaces *7*, 23967–23977.

158. Arakawa, Y., and Sakaki, H. (1982). Multidimensional quantum well laser and temperature dependence of its threshold current. Appl. Phys. Lett. *40*, 939–941.

159. Ramesh, R., and Schlom, D.G. (2019). Creating emergent phenomena in oxide superlattices. Nat. Rev. Mater. *4*, 257–268.

160. Brown, A.A.M., Damodaran, B., Jiang, L., Tey, J.N., Pu, S.H., Mathews, N., and Mhaisalkar, S.G. (2020). Lead halide perovskite nanocrystals: room temperature syntheses toward commercial viability. Adv. Energy Mater. *10*, 2001349.

161. Schulz, A.D., Röhm, H., Leonhard, T., Wagner, S., Hoffman, M.J., and Colsmann, A. (2019). On the ferroelectricity of $\mathrm{CH_3NH_3PbI_3}$ perovskites. Nat. Mater. *18*, 1050.

162. Garten, L.M., Moore, D.T., Nanayakkara, S.U., Dwaraknath, S., Schulz, P., Wands, J., Rockett, A., Newell, B., Persson, K.A., Trolier-McKinstry, S., and Ginley, D.S. (2019). The existence and impact of persistent ferroelectric domains in $\mathrm{MAPbI_3}$. Sci. Adv. *5*, eaas9311.

163. Vorpahl, S.M., Giridharagopal, R., Eperon, G.E., Hermes, I.M., Weber, S.A.L., and Ginger, D.S. (2018). Orientation of ferroelectric domains and disappearance upon heating methylammonium lead triiodide perovskite from tetragonal to cubic phase. ACS Appl. Energy Mater. *1*, 1534–1539.

164. Röhm, H., Leonhard, T., Hoffmann, M.J., and Colsmann, A. (2017). Ferroelectric domains in methylammonium lead iodide perovskite thin-films. Energy Environ. Sci. *10*, 950–955.

165. Liu, Y., Collins, L., Proksch, R., Kim, S., Watson, B.R., Doughty, B., Calhoun, T.R., Ahmadi, M., Ievlev, A.V., Jesse, S., et al. (2019). Reply to: on the ferroelectricity of $\mathrm{CH_3NH_3PbI_3}$ perovskites. Nat. Mater. *18*, 1051–1053.

166. Liu, Y., Collins, L., Proksch, R., Kim, S., Watson, B.R., Doughty, B., Calhoun, T.R., Ahmadi, M., Ievlev, A.V., Jesse, S., et al. (2018). Chemical nature of ferroelastic twin domains in $\mathrm{CH_3NH_3PbI_3}$ perovskite. Nat. Mater. *17*, 1013–1019.

167. Peláiz-Barranco, A. (2015). Ferroelectric Materials: Synthesis and Characterization (BoD-Books on Demand).

168. Wilson, J.N., Frost, J.M., Wallace, S.K., and Walsh, A. (2019). Dielectric and ferroic properties of metal halide perovskites. APL Mater. *7*, 010901.

169. Hu, S., Gao, H., Qi, Y., Tao, Y., Li, Y., Reimers, J.R., Bokdam, M., Franchini, C., Di Sante, D., Stroppa, A., and Ren, W. (2017). Dipole order in halide perovskites: polarization and rashba band splittings. J. Phys. Chem. C *121*, 23045–23054.

170. Govinda, S., Kore, B.P., Swain, D., Hossain, A., De, C., Guru Row, T.N., and Sarma, D.D. (2018). Critical comparison of $\mathrm{FAPbX_3}$ and $\mathrm{MAPbX_3}$ (X = Br and Cl): how do they differ? J. Phys. Chem. C *122*, 13758–13766.

171. Xu, Y. (2013). Ferroelectric Materials and Their Applications (Elsevier).

172. Wright, A.D., Verdi, C., Milot, R.L., Eperon, G.E., Pérez-Osorio, M.A., Snaith, H.J., Giustino, F., Johnston, M.B., and Herz, L.M. (2016). Electron-phonon coupling in hybrid lead halide perovskites. Nat. Commun. *7*, 11755.

173. Mante, P.-A., Stoumpos, C.C., Kanatzidis, M.G., and Yartsev, A. (2017). Electron-acoustic phonon coupling in single crystal $\mathrm{CH_3NH_3PbI_3}$ perovskites revealed by coherent acoustic phonons. Nat. Commun. *8*, 14398.

174. Franssen, W.M.J., and Kentgens, A.P.M. (2019). Solid-state NMR of hybrid halide perovskites. Solid State Nucl. Magn. Reson. *100*, 36–44.

175. Yamada, T., Yamada, Y., and Kanemitsu, Y. (2020). Photon recycling in perovskite $\mathrm{CH_3NH_3PbX_3}$ (X = I, Br, Cl) bulk single crystals and polycrystalline films. J. Lumin. *220*, 116987.

176. Rakita, Y., Cohen, S.R., Kedem, N.K., Hodes, G., and Cahen, D. (2015). Mechanical properties of $\mathrm{APbX_3}$ (A= Cs or $\mathrm{CH_3NH_3}$; X= I or Br) perovskite single crystals. MRS Commun. *5*, 623–629.

177. Sun, S., Fang, Y., Kieslich, G., White, T.J., and Cheetham, A.K. (2015). Mechanical properties of organic-inorganic halide perovskites, $\mathrm{CH_3NH_3PbX_3}$ (X= I, Br and Cl), by nanoindentation. J. Mater. Chem. A *3*, 18450–18455.

178. Strelcov, E., Dong, Q., Li, T., Chae, J., Shao, Y., Deng, Y., Gruverman, A., Huang, J., and Centrone, A. (2017). $\mathrm{CH_3NH_3PbI_3}$ perovskites: ferroelasticity revealed. Sci. Adv. *3*, e1602165.

179. Shahrokhi, S., Gao, W., Wang, Y., Anandan, P.R., Rahaman, M.Z., Singh, S., Wang, D., Cazorla, C., Yuan, G., Liu, J.-M., and Wu, T. (2020). Emergence of ferroelectricity in halide perovskites. Small Methods, 2000149.

180. Zhang, P., Zhang, G., Liu, L., Ju, D., Zhang, L., Cheng, K., and Tao, X. (2018). Anisotropic optoelectronic properties of melt-grown bulk $\mathrm{CsPbBr_3}$ single crystal. J. Phys. Chem. Lett. *9*, 5040–5046.

181. Song, J., Cui, Q., Li, J., Xu, J., Wang, Y., Xu, L., Xue, J., Dong, Y., Tian, T., Sun, H., and Zeng, H. (2017). Ultralarge all-inorganic perovskite bulk single crystal for high-performance visible-infrared dual-modal photodetectors. Adv. Opt. Mater. *5*, 1700157.

182. Stoumpos, C.C., Malliakas, C.D., Peters, J.A., Liu, Z., Maria, S., Im, J., Chasapis, T.C., Wibowo, A.C., Chung, D.Y., Freeman, A.J., et al. (2013). Crystal growth of the perovskite semiconductor $\mathrm{CsPbBr_3}$: a new material for high-energy radiation detection. Cryst. Growth Des. *13*, 2722–2727.

183. Rodová, M., Brožek, J., Knížek, K., and Nitsch, K. (2003). Phase transitions in ternary caesium lead bromide. J. Therm. Anal. Calorim. *71*, 667–673.

184. Lee, B., He, J., Chang, R.P., and Kanatzidis, M.G. (2012). All-solid-state dye-sensitized solar cells with high efficiency. Nature *485*, 486–489.

185. Liao, W.-Q., Zhang, Y., Hu, C.-L., Mao, J.-G., Ye, H.-Y., Li, P.-F., Huang, S.D., and Xiong, R.-G. (2015). A lead-halide perovskite molecular ferroelectric semiconductor. Nat. Commun. *6*, 7338.

186. Saidaminov, M.I., Abdelhady, A.L., Maculan, G., and Bakr, O.M. (2015). Retrograde solubility of formamidinium and methylammonium lead halide perovskites enabling rapid single crystal growth. Chem. Commun. *51*, 17658–17661.

187. Maculan, G., Sheikh, A.D., Abdelhady, A.L., Saidaminov, M.I., Haque, M.A., Murali, B., Alarousu, E., Mohammed, O.F., Wu, T., and Bakr, O.M. (2015). $\mathrm{CH_3NH_3PbCl_3}$ single crystals: inverse temperature crystallization and visible-blind UV-photodetector. J. Phys. Chem. Lett. *6*, 3781–3786.

188. Dirin, D.N., Cherniukh, I., Yakunin, S., Shynkarenko, Y., and Kovalenko, M.V. (2016). Solution-grown $\mathrm{CsPbBr_3}$ perovskite single crystals for photon detection. Chem. Mater. *28*, 8470–8474.

189. Andričević, P., Frajtag, P., Lamirand, V.P., Pautz, A., Kollár, M., Náfrádi, B., Sienkiewicz, A., Garma, T., Forró, L., and Horváth, E. (2020).

Kilogram-scale crystallogenesis of halide perovskites for gamma-rays dose rate measurements. Adv. Sci. 2001882.

190. Tong, Y., Ehrat, F., Vanderlinden, W., Cardenas-Daw, C., Stolarczyk, J.K., Polavarapu, L., and Urban, A.S. (2016). Dilution-induced formation of hybrid perovskite nanoplatelets. ACS Nano *10*, 10936–10944.

191. Weidman, M.C., Seitz, M., Stranks, S.D., and Tisdale, W.A. (2016). Highly tunable colloidal perovskite nanoplatelets through variable cation, metal, and halide composition. ACS Nano *10*, 7830–7839.

192. Wang, G., Li, D., Cheng, H.-C., Li, Y., Chen, C.-Y., Yin, A., Zhao, Z., Lin, Z., Wu, H., He, Q., et al. (2015). Wafer-scale growth of large arrays of perovskite microplate crystals for functional electronics and optoelectronics. Sci. Adv. *1*, e1500613.

193. Liang, D., Peng, Y., Fu, Y., Shearer, M.J., Zhang, J., Zhai, J., Zhang, Y., Hamers, R.J., Andrew, T.L., and Jin, S. (2016). Color-pure violet-light-emitting diodes based on layered lead halide perovskite nanoplates. ACS Nano *10*, 6897–6904.

194. Zhang, Q., Ha, S.T., Liu, X., Sum, T.C., and Xiong, Q. (2014). Room-temperature near-infrared high-Q perovskite whispering-gallery planar nanolasers. Nano Lett. *14*, 5995–6001.

195. Zhang, Q., Su, R., Liu, X., Xing, J., Sum, T.C., and Xiong, Q. (2016). High-quality whispering-gallery-mode lasing from cesium lead halide perovskite nanoplatelets. Adv. Funct. Mater. *26*, 6238–6245.

196. Hu, X., Zhou, H., Jiang, Z., Wang, X., Yuan, S., Lan, J., Fu, Y., Zhang, X., Zheng, W., Wang, X., et al. (2017). Direct vapor growth of perovskite $CsPbBr_3$ nanoplate electroluminescence devices. ACS Nano *11*, 9869–9876.

197. Wang, Y., Shi, Y., Xin, G., Lian, J., and Shi, J. (2015). Two-dimensional van der Waals epitaxy kinetics in a three-dimensional perovskite halide. Cryst. Growth Des. *15*, 4741–4749.

198. Akkerman, Q.A., Motti, S.G., Srimath Kandada, A.R., Mosconi, E., D'Innocenzo, V., Bertoni, G., Marras, S., Kamino, B.A., Miranda, L., De Angelis, F., et al. (2016). Solution synthesis approach to colloidal cesium lead halide perovskite nanoplatelets with monolayer-level thickness control. J. Am. Chem. Soc. *138*, 1010–1016.

199. Zhu, H., Fu, Y., Meng, F., Wu, X., Gong, Z., Ding, Q., Gustafsson, M.V., Trinh, M.T., Jin, S., and Zhu, X.Y. (2015). Lead halide perovskite nanowire lasers with low lasing thresholds and high quality factors. Nat. Mater. *14*, 636–642.

200. Protesescu, L., Yakunin, S., Bodnarchuk, M.I., Krieg, F., Caputo, R., Hendon, C.H., Yang, R.X., Walsh, A., and Kovalenko, M. (2015). Nanocrystals of cesium lead halide perovskites ($CsPbX_3$, X= Cl, Br, and I): novel optoelectronic materials showing bright emission with wide color gamut. Nano Lett. *15*, 3692–3696.

201. Tyagi, P., Arveson, S.M., and Tisdale, W.A. (2015). Colloidal organohalide perovskite nanoplatelets exhibiting quantum confinement. J. Phys. Chem. Lett. *6*, 1911–1916.

202. He, X., Liu, P., Wu, S., Liao, Q., Yao, J., and Fu, H. (2017). Multi-color perovskite nanowire lasers through kinetically controlled solution growth followed by gas-phase halide exchange. J. Mater. Chem. C *5*, 12707–12713.

203. Jiang, J., Sun, X., Chen, X., Wang, B., Chen, Z., Hu, Y., Guo, Y., Zhang, L., Ma, Y., Gao, L., et al. (2019). Carrier lifetime enhancement in halide perovskite via remote epitaxy. Nat. Commun. *10*, 4145.

204. Chen, J., Fu, Y., Samad, L., Dang, L., Zhao, Y., Shen, S., Guo, L., and Jin, S. (2017). Vapor-phase epitaxial growth of aligned nanowire networks of cesium lead halide perovskites ($CsPbX_3$, X= Cl, Br, I). Nano Lett. *17*, 460–466.

205. Shoaib, M., Zhang, X., Wang, X., Zhou, H., Xu, T., Wang, X., Hu, X., Liu, H., Fan, X., Zheng, W., et al. (2017). Directional growth of ultralong $CsPbBr_3$ perovskite nanowires for high-performance photodetectors. J. Am. Chem. Soc. *139*, 15592–15595.

206. Schmidt, L.C., Pertegás, A., González-Carrero, S., Malinkiewicz, O., Agouram, S., Mínguez Espallargas, G., Bolink, H.J., Galian, R.E., and Pérez-Prieto, J. (2014). Nontemplate synthesis of $CH_3NH_3PbBr_3$ perovskite nanoparticles. J. Am. Chem. Soc. *136*, 850–853.

207. Pan, J., Quan, L.N., Zhao, Y., Peng, W., Murali, B., Sarmah, S.P., Yuan, M., Sinatra, L., Alyami, N.M., Liu, J., et al. (2016). Highly efficient perovskite-quantum-dot light-emitting diodes by surface engineering. Adv. Mater. *28*, 8718–8725.

208. Gonzalez-Carrero, S., Galian, R.E., and Pérez-Prieto, J. (2015). Maximizing the emissive properties of $CH_3NH_3PbBr_3$ perovskite nanoparticles. J. Mater. Chem. A *3*, 9187–9193.

209. Shamsi, J., Urban, A.S., Imran, M., De Trizio, L., and Manna, L. (2019). Metal halide perovskite nanocrystals: synthesis, post-synthesis modifications, and their optical properties. Chem. Rev. *119*, 3296–3348.

210. Song, J., Li, J., Li, X., Xu, L., Dong, Y., and Zeng, H. (2015). Quantum dot light-emitting diodes based on inorganic perovskite cesium lead halides ($CsPbX_3$). Adv. Mater. *27*, 7162–7167.

211. Katan, C., Mercier, N., and Even, J. (2019). Quantum and dielectric confinement effects in lower-dimensional hybrid perovskite semiconductors. Chem. Rev. *119*, 3140–3192.

212. Xu, L., Li, J., Cai, B., Song, J., Zhang, F., Fang, T., and Zeng, H. (2020). A bilateral interfacial passivation strategy promoting efficiency and stability of perovskite quantum dot light-emitting diodes. Nat. Commun. *11*, 3902.

213. Protesescu, L., Yakunin, S., Bodnarchuk, M.I., Bertolotti, F., Masciocchi, N., Guagliardi, A., and Kovalenko, M.V. (2016). Monodisperse formamidinium lead bromide nanocrystals with bright and stable green photoluminescence. J. Am. Chem. Soc. *138*, 14202–14205.

214. Protesescu, L., Yakunin, S., Kumar, S., Bär, J., Bertolotti, F., Masciocchi, N., Guagliardi, A., Grotevent, M., Shorubalki, I., Bodnarchuk, M.I., et al. (2017). Dismantling the "red wall" of colloidal perovskites: highly luminescent formamidinium and formamidinium-cesium lead iodide nanocrystals. ACS Nano *11*, 3119–3134.

215. Huang, H., Chen, B., Wang, Z., Hung, T.F., Susha, A.S., Zhong, H., and Rogach, A.L. (2016). Water resistant $CsPbX_3$ nanocrystals coated with polyhedral oligomeric silsesquioxane and their use as solid state luminophores in all-perovskite white light-emitting devices. Chem. Sci. *7*, 5699–5703.

216. Li, X., Wu, Y., Zhang, S., Cai, B., Gu, Y., Song, J., and Zeng, H. (2016). $CsPbX_3$ quantum dots for lighting and displays: room-temperature synthesis, photoluminescence superiorities, underlying origins and white light-emitting diodes. Adv. Funct. Mater. *26*, 2435–2445.

217. Zhou, Q., Bai, Z., Lu, W.-G., Wang, Y., Zou, B., and Zhong, H. (2016). In situ fabrication of halide perovskite nanocrystal-embedded polymer composite films with enhanced photoluminescence for display backlights. Adv. Mater. *28*, 9163–9168.

218. Li, Y., Yan, W., Li, Y., Wang, S., Wang, W., Bian, Z., Xiao, L., and Gong, Q. (2015). Direct observation of long electron-hole diffusion distance in $CH_3NH_3PbI_3$ perovskite thin film. Sci. Rep. *5*, 14485.

219. Stranks, S.D., Eperon, G.E., Grancini, G., Menelaou, C., Alcocer, M.J.P., Leijtens, T., Herz, L.M., Petrozza, A., and Snaith, H.J. (2013). Electron-hole diffusion lengths exceeding 1 micrometer in an organometal trihalide perovskite absorber. Science *342*, 341–344.

220. Liu, Y., Sun, J., Yang, Z., Yang, D., Ren, X., Xu, H., Yang, Z., and Liu, S.F. (2016). 20-mm-Large single-crystalline formamidinium-perovskite wafer for mass production of integrated photodetectors. Adv. Opt. Mater. *4*, 1829–1837.

221. Lv, Q., Lian, Z., He, W., Sun, J.-L., Li, Q., and Yan, Q. (2018). A universal top-down approach toward thickness-controllable perovskite single-crystalline thin films. J. Mater. Chem. C *6*, 4464–4470.

222. Liu, Y., Zhang, Y., Yang, Z., Yang, D., Ren, X., Pang, L., and Liu, S.F. (2016). Thinness-and shape-controlled growth for ultrathin single-crystalline perovskite wafers for mass production of superior photoelectronic devices. Adv. Mater. *28*, 9204–9209.

223. Chen, Y.-X., Ge, Q.-Q., Shi, Y., Liu, J., Xue, D.-J., Ma, J.-Y., Ding, J., Yan, H.-J., Hu, J.-S., and Wan, L.-J. (2016). General space-confined on-substrate fabrication of thickness-adjustable hybrid perovskite single-crystalline thin films. J. Am. Chem. Soc. *138*, 16196–16199.

224. Chen, Z., Dong, Q., Liu, Ye., Bao, C., Fang, Y., Lin, Y., Tang, S., Wang, Q., Xiao, X., Bai, Y., et al. (2017). Thin single crystal perovskite solar cells to harvest below-bandgap light absorption. Nat. Commun. *8*, 1890.

225. Zhumekenov, A.A., Burlakov, V.M., Saidaminov, M.I., Alofi, A., Haque, M., Turedi, B., Davaasuren, B., Dursun, I., Cho, N.C., El-Zohry, A.M., et al. (2017). The role of surface

tension in the crystallization of metal halide perovskites. ACS Energy Lett. *2*, 1782–1788.

226. Lee, L., Baek, J., Park, K.S., Lee, Y.-E., Shrestha, N.K., and Sung, M.M. (2017). Wafer-scale single-crystal perovskite patterned thin films based on geometrically-confined lateral crystal growth. Nat. Commun. *8*, 15882.

227. Gu, Z., Huang, Z., Li, C., Li, M., and Song, Y. (2018). A general printing approach for scalable growth of perovskite single-crystal films. Sci. Adv. *4*, 2390.

228. Wang, Y., Sun, X., Chen, Z., Sun, Y.-Y., Zhang, S., Lu, T.-M., Wertz, E., and Shi, J. (2017). High-temperature ionic epitaxy of halide perovskite thin film and the hidden carrier dynamics. Adv. Mater. *29*, 1702643.

229. Zhu, W., Ma, W., Su, Y., Chen, Z., Chen, X., Ma, Y., Bai, L., Xiao, W., Liu, T., Zhu, H., et al. (2020). Low-dose real-time X-ray imaging with nontoxic double perovskite scintillators. Light Sci. Appl. *9*, 112.

230. Chen, J., Morrow, D.J., Fu, Y., Zheng, W., Zhao, Y., Dang, L., Stolt, M., Kohler, D.D., Wang, X., Czech, K.J., et al. (2017). Single-crystal thin films of cesium lead bromide perovskite epitaxially grown on metal oxide perovskite ($SrTiO_3$). J. Am. Chem. Soc. *139*, 13525–13532.

231. Xu, S., Shen, Y., Ding, Y., and Wang, Z.L. (2010). Growth and transfer of monolithic horizontal ZnO nanowire superstructures onto flexible substrates. Adv. Funct. Mater. *20*, 1493–1497.

232. Jiang, Q., Zhao, Y., Zhang, X., Yang, X., Chen, Y., Chu, Z., Ye, Q., Li, X., Yin, Z., and You, J. (2019). Surface passivation of perovskite film for efficient solar cells. Nat. Photon. *13*, 460–466.

233. Li, W., Zheng, J., Hu, B., Fu, H.-C., Hu, M., Veyssal, A., Zhao, Y., He, J.-H., Liu, T.L., Ho-Baillie, A., and Jin, S. (2020). High-performance solar flow battery powered by a perovskite/silicon tandem solar cell. Nat. Mater. 1326–1331.

234. Hou, Y., Aydin, E., De Bastiani, M., Xiao, C., Isikgor, F.H., Xue, D.-J., Chen, B., Chen, H., Bahrami, B., Chowdhury, A.H., et al. (2020). Efficient tandem solar cells with solution-processed perovskite on textured crystalline silicon. Science *367*, 1135–1140.

235. Li, C., Hailu, W., Wang, F., Li, T., Xu, M., Wang, H., Zhen, W., Zhan, X., Hu, W., and Shen, L. (2020). Ultrafast and broadband photodetectors based on a perovskite/organic bulk heterojunction for large-dynamic-range imaging. Light Sci. Appl. *9*, 31.

236. Xu, Z., Yu, Y., Arya, S., Niaz, I.A., Chen, Y., Lei, Y., Miah, M.A.R., Zhou, J., Zhang, A.C., Yan, L., et al. (2020). Frequency- and power-dependent photoresponse of a perovskite photodetector down to the single-photon level. Nano Lett. *20*, 2144–2151.

237. Mica, N.A., Bian, R., Manousiadis, P., Jagadamma, L.K., Tavakkolnia, I., Haas, H., Turnbull, G.A., and Samuel, I.D.W. (2020). Triple-cation perovskite solar cells for visible light communications. Photon. Res. *8*, A16–A24.

238. Yakunin, S., Dirin, D.N., Shynkarenko, Y., Morad, V., Cherniukh, I., Nazarenko, O., Kreil, D., Nauser, T., and Kovalenko, M.V. (2016). Detection of gamma photons using solution-grown single crystals of hybrid lead halide perovskites. Nat. Photon. *10*, 585–589.

239. Kim, Y.-H., Kim, S., Kakekhani, A., Park, J., Park, J., Lee, Y.-H., Xu, H., Nagane, S., Wexler, R.B., Kim, D.-H., et al. (2021). Comprehensive defect suppression in perovskite nanocrystals for high-efficiency light-emitting diodes. Nat. Photon. *15*, 148–155.

240. Cao, Y., Wang, N., Tian, H., Guo, J., Wei, Y., Chen, H., Miao, Y., Zou, W., Pan, K., He, Y., et al. (2018). Perovskite light-emitting diodes based on spontaneously formed submicrometre-scale structures. Nature *562*, 249–253.

241. Matsushima, T., Bencheikh, F., Komino, T., Leyden, M.R., Sandanayaka, A.S.D., Qin, C., and Adachi, C. (2019). High performance from extraordinarily thick organic light-emitting diodes. Nature, 502–506.

242. Qin, C., Sandanayaka, A.S.D., Zhao, C., Matsushima, T., Zhang, D., Fujihara, T., and Adachi, C. (2020). Stable room-temperature continuous-wave lasing in quasi-2D perovskite films. Nature *585*, 53–57.

243. Huang, C., Sun, W., Fan, Y., Wang, Y., Gao, Y., Zhang, N., Wang, K., Liu, S., Wang, S., Xiao, S., and Song, Q. (2018). Formation of lead halide perovskite based plasmonic nanolasers and nanolaser arrays by tailoring the substrate. ACS Nano, 3865–3874.

244. Zhang, N., Fan, Y., Wang, K., Gu, Z., Wang, Y., Ge, L., Xiao, S., and Song, Q. (2019). All-optical control of lead halide perovskite microlasers. Nat. Commun. *10*, 1770.

245. Haihua, Z., Wu, Y., Liao, Q., Zhang, Z., Liu, Y., Gao, Q., Liu, P., Li, M., Yao, J., and Fu, H. (2018). A two-dimensional Ruddlesden-Popper perovskite nanowire laser array based on ultrafast light-harvesting quantum wells. Angew. Chem. Int. Ed. *0*, 7748–7752.

246. Yang, Z., Lu, J., ZhuGe, M., Cheng, Y., Hu, J., Li, F., Qiao, S., Zhang, Y., Hu, G., Yang, Q., et al. (2019). Controllable growth of aligned monocrystalline $CsPbBr_3$ microwire arrays for piezoelectric-induced dynamic modulation of single-mode lasing. Adv. Mater. *31*, 1900647.

247. Fang, H.-H., Adjokatse, S., Wei, H., Yang, J., Blake, G.R., Huang, J., Even, J., and Loi, M.A. (2016). Ultrahigh sensitivity of methylammonium lead tribromide perovskite single crystals to environmental gases. Sci. Adv. *2*, e1600534.

248. Huang, Y., Feng, Y., Li, F., Lin, F., Wang, Y., Chen, X., and Xie, R. (2020). Sensing studies and applications based on metal halide perovskite materials: current advances and future perspectives. Trends Anal. Chem. 116127.

249. Lu, H., Wang, J., Xiao, C., Pan, X., Chen, X., Brunecky, R., Berry, J.J., Zhu, K., Beard, M.C., and Vardeny, Z.V. (2019). Spin-dependent charge transport through 2D chiral hybrid lead-iodide perovskites. Sci. Adv. *5*, eaay0571.

250. Zhu, X., Lin, Y., San Martin, J., Sun, Y., Zhu, D., and Yan, Y. (2019). Lead halide perovskites for photocatalytic organic synthesis. Nat. Commun. *10*, 2843.

251. Sun, Y., Qian, L., Xie, D., Lin, Y., Sun, M., Li, W., Ding, L., Ren, T., and Palacios, T. (2019). Photoelectric synaptic plasticity realized by 2D perovskite. Adv. Funct. Mater. *29*, 1902538.

252. Sun, M.-J., Zheng, C., Gao, Y., Johnston, A., Najarian, A.M., Wang, P.X., Voznyy, O., Hoogland, S., and Sargent, E.H. (2021). Linear electro-optic modulation in highly polarizable organic perovskites. Adv. Mater. *33*, 2006368.

253. Tan, H., Jain, A., Voznyy, O., Lan, X., García de Arquer, F.P., Fan, J.Z., Quintero-Bermudez, R., Yuan, M., Zhang, B., Zhao, Y., et al. (2017). Efficient and stable solution-processed planar perovskite solar cells via contact passivation. Science *355*, 722–726.

254. Zhu, C., Niu, X., Fu, Y., Li, N., Hu, C., Chen, Y., He, X., Na, G., Liu, P., Zai, H., et al. (2019). Strain engineering in perovskite solar cells and its impacts on carrier dynamics. Nat. Commun. *10*, 815.

255. Zhao, J., Deng, Y., Wei, H., Zheng, X., Yu, Z., Shao, Y., Shield, J.E., and Huang, J. (2017). Strained hybrid perovskite thin films and their impact on the intrinsic stability of perovskite solar cells. Sci. Adv. *3*, eaao5616.

256. Tsai, H., Asadpour, R., Blancon, J.C., Stoumpos, C.C., Durand, O., Strzalka, J.W., Chen, B., Verduzco, R., Ajayan, P.M., Tretiak, S., et al. (2018). Light-induced lattice expansion leads to high-efficiency perovskite solar cells. Science *360*, 67–70.

257. Juarez-Perez, E.J., Hawash, Z., Raga, S.R., Ono, L.K., and Qi, Y. (2016). Thermal degradation of $CH_3NH_3PbI_3$ perovskite into NH_3 and CH_3I gases observed by coupled thermogravimetry–mass spectrometry analysis. Energy Environ. Sci. *9*, 3406–3410.

258. Zhao, Y.-C., Zhou, W.-K., Zhou, X., Liu, K.-H., Yu, D.-P., and Zhao, Q. (2017). Quantification of light-enhanced ionic transport in lead iodide perovskite thin films and its solar cell applications. Light Sci. Appl. *6*, e16243.

259. Nie, W., Tsai, H., Asadpour, R., Blancon, J.-C., Neukirch, A.J., Gupta, G., Crochet, J.J., Chhowalla, M., Tretiak, S., Alam, M.A., et al. (2015). High-efficiency solution-processed perovskite solar cells with millimeter-scale grains. Science *347*, 522–525.

260. Li, Y., and Ding, L. (2020). Single-crystal perovskite devices. Sci. Bull. *66*, 214–218.

261. Peng, W., Wang, L., Murali, B., Ho, K.-T., Bera, A., Cho, N., Kang, C.-F., Burlakov, V.M., Pan, J., Sinatra, L., et al. (2016). Solution-grown monocrystalline hybrid perovskite films for hole-transporter-free solar cells. Adv. Mater. *28*, 3383–3390.

262. Rao, H.-S., Chen, B.-X., Wang, X.-D., Kuang, D.-B., and Su, C.-Y. (2017). A micron-scale laminar $MAPbBr_3$ single crystal for an efficient and stable perovskite solar cell. Chem. Commun. *53*, 5163–5166.

263. Zhao, J., Guoli, K., Chen, S., Li, Q., Huang, B., Liu, Z., San, X., Wang, Y., Wang, C., Zhen, Y., et al. (2017). Single crystalline $CH_3NH_3PbI_3$ self-grown on FTO/TiO_2 substrate for high

efficiency perovskite solar cells. Sci. Bull. *62*, 1173–1176.

264. Yue, H.L., Sung, H.H., and Chen, F.C. (2018). Seeded space-limited crystallization of $CH_3NH_3PbI_3$ single-crystal plates for perovskite solar cells. Adv. Electron. Mater. *4*, 1700655.

265. Chen, Z., Turedi, B., Alsalloum, A., Yang, C., Zheng, X., Gereige, I., AlSaggaf, A., Mohammed, O.F., and Bakr, O. (2019). Single-crystal $MAPbI_3$ perovskite solar cells exceeding 21% power conversion efficiency. ACS Energy Lett. *4*, 1258–1259.

266. Tsai, H., Asadpour, R., Blancon, J.-C., Stoumpos, C.C., Even, J., Ajayan, P.M., Kanatzidis, M.G., Alam, M.A., Mohite, A.D., and Nie, W. (2018). Design principles for electronic charge transport in solution-processed vertically stacked 2D perovskite quantum wells. Nat. Commun. *9*, 2130.

267. Liu, Y., Ren, X., Zhang, J., Yang, Z., Yang, D., Yu, F., Sun, J., Zhao, C., Yao, Z., Wang, B., et al. (2017). 120 mm single-crystalline perovskite and wafers: towards viable applications. Sci. China Chem. *60*, 1367–1376.

268. Liu, Y., Dong, Q., Fang, Y., Lin, Y., Deng, Y., and Huang, J. (2019). Fast growth of thin $MAPbI_3$ crystal wafers on aqueous solution surface for efficient lateral-structure perovskite solar cells. Adv. Funct. Mater. *29*, 1807707.

269. Huang, Y., Zhang, Y., Sun, J., Wang, X., Sun, J., Chen, Q., Pan, C., and Zhou, H. (2018). The exploration of carrier behavior in the inverted mixed perovskite single-crystal solar cells. Adv. Mater. Interfaces *5*, 1800224.

270. Liu, Y., Zhang, Y., Yang, Z., Ye, H., Feng, J., Xu, Z., Zhang, X., Munir, R., Liu, J., Zuo, P., et al. (2018). Multi-inch single-crystalline perovskite membrane for high-detectivity flexible photosensors. Nat. Commun. *9*, 5302.

271. Fang, Y., Dong, Q., Shao, Y., Yuan, Y., and Huang, J. (2015). Highly narrowband perovskite single-crystal photodetectors enabled by surface-charge recombination. Nat. Photon. *9*, 679.

272. Chen, M., Shan, X., Geske, T., Li, J., and Yu, Z. (2017). Manipulating ion migration for highly stable light-emitting diodes with single-crystalline organometal halide perovskite microplatelets. ACS Nano *11*, 6312–6318.

273. Nguyen, V.-C., Katsuki, H., Sasaki, F., and Yanagi, H. (2018). Single-crystal perovskite $CH_3NH_3PbBr_3$ prepared by cast capping method for light-emitting diodes. Jpn. J. Appl. Phys. *57*, 04FL10.

274. Cheng, X., Jing, L., Yuan, Y., Du, S., Yao, Q., Zhang, J., Ding, J., and Zhou, T. (2019). Centimeter-size square 2D layered Pb-free hybrid perovskite single crystal $(CH_3NH_3)_2MnCl_4$ for red photoluminescence. CrystEngComm *21*, 4085–4091.

275. Wei, H., Fang, Y., Mulligan, P., Chuirazzi, W., Fang, H.-H., Wang, C., Ecker, B.R., Gao, Y., Loi, M.A., Cao, L., and Huang, J. (2016). Sensitive X-ray detectors made of methylammonium lead tribromide perovskite single crystals. Nat. Photon. *10*, 333.

276. Rao, H.S., Li, W.G., Chen, B.X., Kuang, D.B., and Su, C.Y. (2017). In situ growth of 120 cm^2 $CH_3NH_3PbBr_3$ perovskite crystal film on FTO glass for narrowband-photodetectors. Adv. Mater. *29*, 1602639.

277. Saidaminov, M.I., Haque, M.A., Savoie, M., Abdelhady, A.L., Cho, N., Dursun, I., Buttner, U., Alarousu, E., Wu, T., and Bakr, O.M. (2016). Perovskite photodetectors operating in both narrowband and broadband regimes. Adv. Mater. *28*, 8144–8149.

278. Zhang, M., Zhang, F., Wang, Y., Zhu, L., Hu, Y., Lou, Z., Hou, Y., and Teng, F. (2018). High-performance photodiode-type photodetectors based on polycrystalline formamidinium lead iodide perovskite thin films. Sci. Rep. *8*, 11157.

279. Li, D., Dong, G., Li, W., and Wang, L. (2015). High performance organic-inorganic perovskite-optocoupler based on low-voltage and fast response perovskite compound photodetector. Sci. Rep. *5*, 7902.

280. Liu, C., Wang, K., Yi, C., Shi, X., Du, P., Smith, A.W., Karim, A., and Gong, X. (2015). Ultrasensitive solution-processed perovskite hybrid photodetectors. J. Mater. Chem. C *3*, 6600–6606.

281. Fu, Y., Song, Q., Lin, T., Wang, Y., Sun, X., Su, Z., Chu, B., Jin, F., Zhao, H., Li, W., and Lee, C.S. (2017). High performance photomultiplication perovskite photodetectors with $PC_{60}BM$ and NPB as the interlayers. Org. Electronics *51*, 200–206.

282. Domanski, K., Tress, W., Moehl, T., Saliba, M., Nazeeruddin, M.K., and Grätzel, M. (2015). Working principles of perovskite photodetectors: analyzing the interplay between photoconductivity and voltage-driven energy-level alignment. Adv. Funct. Mater. *25*, 6936–6947.

283. Dong, R., Fang, Y., Chae, J., Dai, J., Xiao, Z., Dong, Q., Yuan, Y., Centrone, A., Zeng, X.C., and Huang, J. (2015). High-gain and low-driving-voltage photodetectors based on organolead triiodide perovskites. Adv. Mater. *27*, 1912–1918.

284. Deschler, F., Price, M., Pathak, S., Klintberg, L.E., Jarausch, D.-D., Higler, R., Hüttner, S., Leijtens, T., Stranks, S.D., Snaith, H.J., et al. (2014). High photoluminescence efficiency and optically pumped lasing in solution-processed mixed halide perovskite semiconductors. J. Phys. Chem. Lett. *5*, 1421–1426.

285. Zhizhchenko, A., Syubaev, S., Berestennikov, A., Yulin, A.V., Porfirev, A., Pushkarev, A., Shishkin, I., Golokhvast, K., Bogdanov, A.A., Zakhidov, A.A., et al. (2019). Single-mode lasing from imprinted halide-perovskite microdisks. ACS Nano *13*, 4140–4147.

286. Ren, K., Wang, J., Chen, S., Yang, Q., Tian, J., Yu, H., Sun, M., Zhu, X., Yue, S., Sun, Y., et al. (2019). Realization of perovskite-nanowire-based plasmonic lasers capable of mode modulation. Laser Photon. Rev. *13*, 1800306.

287. Li, X., Wang, K., Chen, M., Wang, S., Fan, Y., Liang, T., Song, Q., Xing, G., and Tang, Z. (2020). Stable whispering gallery mode lasing from solution-processed formamidinium lead bromide perovskite microdisks. Adv. Opt. Mater. 2000030.

288. Liao, Q., Hu, K., Zhang, H., Wang, X., Yao, J., and Fu, H. (2015). Perovskite microdisk microlasers self-assembled from solution. Adv. Mater. *27*, 3405–3410.

289. Eaton, S.W., Lai, M., Gibson, N.A., Wong, A.B., Dou, L., Ma, J., Wang, L.-W., Leone, S.R., and Yang, P. (2016). Lasing in robust cesium lead halide perovskite nanowires. Proc. Natl. Acad. Sci. *113*, 1993–1998.

290. Li, F., Ma, C., Wang, H., Hu, W., Yu, W., Sheikh, A.D., and Wu, T. (2015). Ambipolar solution-processed hybrid perovskite phototransistors. Nat. Commun. *6*, 8238.

291. Li, D., Wang, G., Cheng, H.-C., Chen, C.-Y., Wu, H., Liu, Y., Huang, Y., and Duan, X. (2016). Size-dependent phase transition in methylammonium lead iodide perovskite microplate crystals. Nat. Commun. *7*, 11330.

292. Chin, X.Y., Cortecchia, D., Yin, J., Bruno, A., and Soci, C. (2015). Lead iodide perovskite light-emitting field-effect transistor. Nat. Commun. *6*, 7383.

293. Matsushima, T., Hwang, S., Sandanayaka, A.S.D., Qin, C., Terakawa, S., Fujihara, T., Yahiro, M., and Adachi, C. (2016). Solution-processed organic-inorganic perovskite field-effect transistors with high hole mobilities. Adv. Mater. *28*, 10275–10281.

294. Yusoff, A.R.b.M., Kim, H.P., Li, X., Kim, J., Jang, J., and Nazeeruddin, M.K. (2017). Ambipolar triple cation perovskite field effect transistors and inverters. Adv. Mater. *29*, 1602940.

295. Yuan, Y., Li, T., Wang, Q., Xing, J., Gruverman, A., and Huang, J. (2017). Anomalous photovoltaic effect in organic-inorganic hybrid perovskite solar cells. Sci. Adv. *3*, e1602164.

296. Christians, J.A., Miranda Herrera, P.A., and Kamat, P.V. (2015). Transformation of the excited state and photovoltaic efficiency of $CH_3NH_3PbI_3$ perovskite upon controlled exposure to humidified air. J. Am. Chem. Soc. *137*, 1530–1538.

297. Wang, K., Wu, C., Hou, Y., Yang, D., and Priya, S. (2019). Monocrystalline perovskite wafers/thin films for photovoltaic and transistor applications. J. Mater. Chem. A *7*, 24661–24690.

298. Wang, Z., Wang, L., Nagai, M., Xie, L., Yi, M., and Huang, W. (2017). Nanoionics-enabled memristive devices: strategies and materials for neuromorphic applications. Adv. Electron. Mater. *3*, 1600510.

299. Wang, Y., Lv, Z., Chen, J., Wang, Z., Zhou, Y., Zhou, L., Chen, X., and Han, S.-T. (2018). Photonic synapses based on inorganic perovskite quantum dots for neuromorphic computing. Adv. Mater. *30*, 1802883.

300. Xu, W., Cho, H., Kim, Y.-H., Kim, Y.-T., Wolf, C., Park, C.-G., and Lee, T.-W. (2016). Organometal halide perovskite artificial synapses. Adv. Mater. *28*, 5916–5922.

301. Manipatruni, S., Nikonov, D.E., and Young, I.A. (2018). Beyond CMOS computing with spin and polarization. Nat. Phys. *14*, 338–343.

302. Zidan, M.A., Strachan, J.P., and Lu, W.D. (2018). The future of electronics based on memristive systems. Nat. Electron. *1*, 22–29.

303. Gong, J., Yu, H., Zhou, X., Wei, H., Ma, M., Han, H., Zhang, S., Ni, Y., Li, Y., and Xu, W. (2020). Lateral artificial synapses on hybrid perovskite platelets with modulated neuroplasticity. Adv. Funct. Mater. 2005413.

304. Bi, G.-q., and Poo, M.-m. (1998). Synaptic modifications in cultured hippocampal neurons: dependence on spike timing, synaptic strength, and postsynaptic cell type. J. Neurosci. *18*, 10464–10472.

305. Lamprecht, R., and LeDoux, J. (2004). Structural plasticity and memory. Nat. Rev. Neurosci. *5*, 45–54.

306. Turedi, B., Yeddu, V., Zheng, X., Kim, D.Y., Bakr, O., and Saidaminov, M.I. (2021). Perovskite single-crystal solar cells: going forward. ACS Energy Lett. *6*, 631–642.

307. Ke, W., Stoumpos, C.C., and Kanatzidis, M.G. (2019). "Unleaded" perovskites: status quo and future prospects of tin-based perovskite solar cells. Adv. Mater. *31*, 1803230.

308. Cai, B., Chen, X., Xie, M., Zhang, S., Liu, X., Yang, J., Zhou, W., Guo, S., and Haibo, Z. (2018). A class of Pb-free double perovskite halide semiconductors with intrinsic ferromagnetism, large spin splitting and high Curie temperature. Mater. Horizon. *5*, 961–968.

309. Nakamura, T., Yakumaru, S., Truong, M.A., Kim, K., Liu, J., Hu, S., Otsuka, K., Hashimoto, R., Murdey, R., Sasamori, T., et al. (2020). Sn(IV)-free tin perovskite films realized by in situ Sn(0) nanoparticle treatment of the precursor solution. Nat. Commun. *11*, 3008.

310. Lin, R., Xiao, K., Qin, Z., Han, Q., Zhang, C., Wei, M., Saidaminov, M.I., Gao, Y., Xu, J., Xiao, M., et al. (2019). Monolithic all-perovskite tandem solar cells with 24.8% efficiency exploiting comproportionation to suppress Sn(II) oxidation in precursor ink. Nat. Energy *4*, 864–873.

311. Yang, W.S., Park, B.-W., Jung, E.H., Jeon, N.J., Kim, Y.C., Lee, D.U., Shin, S.S., Seo, J., Kim, E.K., Noh, J.H., and Seok, S.I. (2017). Iodide management in formamidinium-lead-halide-based perovskite layers for efficient solar cells. Science *356*, 1376–1379.

312. Wang, F., Bai, S., Tress, W., Hagfeldt, A., and Gao, F. (2018). Defects engineering for high-performance perovskite solar cells. NPJ Flex. Electron. *2*, 22.

313. Xie, Y., Yin, J., Zheng, J., Fan, Y., Wu, J., and Zhang, X. (2019). Facile RbBr interface modification improves perovskite solar cell efficiency. Mater. Today Chem. *14*, 100179.

314. Yang, Y., Yang, M., Moore, D.T., Yan, Y., Miller, E.M., Zhu, K., and Beard, M.C. (2017). Top and bottom surfaces limit carrier lifetime in lead iodide perovskite films. Nat. Energy *2*, 16207.

315. Li, B., Zhang, Y., Fu, L., Yu, T., Zhou, S., Zhang, L., and Yin, L. (2018). Surface passivation engineering strategy to fully-inorganic cubic $CsPbI_3$ perovskites for high-performance solar cells. Nat. Commun. *9*, 1076.